The petrogenesis of the ignimbrites and quartz porphyritic granites exposed along the coast at Saldahna, South Africa

by

Cedric S.A. Joseph

Thesis is presented in partial fulfilment of the requirements for the degree Master of Science at the University of Stellenbosch

Supervisor: Prof. Gary Stevens

Co-Supervisors: Dr. Federico Farina and Prof. John Clemens

December 2013

Declaration

By submitting this thesis/dissertation electronically, I declare that the entirety of the work contained therein is my own, original work, that I am the sole author thereof (save to the extent explicitly otherwise stated), that reproduction and publication thereof by Stellenbosch University will not infringe any third party rights and that I have not previously in its entirety or in part submitted it for obtaining any qualification.

Signature:_____

2013

Abstract

To date, the only volcanic rocks described from the Cape Granite Suite are ignimbrites that crop out along the western margin of Langebaan lagoon, to the south of Saldahna. These ignimbrites, with an age of 515 ± 3 Ma, represent the youngest rocks within the Suite. This study aims to investigate the petrogenesis of fine grained granitic rocks exposed to the north of Langebaan lagoon, as well as to reassess the classification of these rocks as a sub-volcanic quartz porphyritic intrusive.

These rocks exhibit a dark grey to brown micro- to crypto-crystalline matrix containing prominent feldspar and quartz phenocrysts that are often embayed and broken. Phenocrysts of biotite and orthopyroxene (Fs_{50-70}) can be identified microscopically, as can replacement of both phases by chlorite. Ilmenite commonly occurs in close association with the orthopyroxene phenocrysts. A second generation of poikiloblastic biotite overgrows the matrix and is clearly formed through sub-solidus reaction. The feldspar phenocrysts are commonly microcline microperthite. Contact exposures can be observed in the study area which indicates that the finer grained rock intruded older coarser grained granites. The predominance of broken phenocrysts as well as the presence of fiamme present in outcrop in rocks with a microcrystalline matrix is indicative of a volcanic origin, suggesting that these rocks be classified as ignimbrite as opposed to quartz porphyry. The foregoing observations and features could be interpreted to represent a welded ignimbrite deposit which is underlain by coarse grained granite. The finer grained ignimbrite would then represent a subsequent intrusion by a later pulse of similar magma along the contact with the coarser grained granite.

The ignimbrites are silicic with SiO_2 ranging between 69 and 76 wt. %; they are mildly peraluminous with values for ASI (ASI = mol. Al_2O_3/ ($CaO+Na_2O+K_2O$)) ranging from 1.02 to 1.09; and ASI is negatively correlated with Mg + Fe (hereafter maficity). Tight to very tight inter-element correlations exist for several major elements as well as trace elements when plotted against maficity. The following R^2 values apply: Al =0.94; Ca = 0.98; Si = 0.97; Ti = 1.00; Na =0.90; Zr =0.95; La = 0.87. These elements are all positively correlated with maficity, except for Si which is negatively correlated.

Orthopyroxene and ilmenite represent early formed, high temperature minerals in the magma. In the biotite-poor rocks, ilmenite represents the main reservoir of titanium whilst orthopyroxene represents the main MgO and FeO reservoir. The exceptionally tight Ti: maficity correlation requires that both these minerals always be present at the same molecular ratio in the magma, despite the significant range in maficity portrayed by the rocks and despite the fact that these minerals have different size-density relationships. This exceptionally tight correlation can be readily interpreted to reflect entrainment of a peritectic assemblage consisting of ilmenite and orthopyroxene. The Al, Ca and Na correlations require the entrainment of peritectic plagioclase. The decreasing trend for ASI requires the entrainment of peritectic clionopyroxene. A near perfect match with the concentrations of these elements in the ignimbrites is produced by modelling entrainment of a peritectic assemblage consisting of plagioclase, ilmenite, orthopyroxene and clionopyroxene in stoichiometric proportions dictated by the melting reaction. A peritectic assemblage formed

by these phases' points to the partial melting of a source undergoing coupled biotite and hornblende fluid-absent melting, with hornblende being subordinate.

The opx- and ilmenite-rich micro-domains in the rocks represent zones in the magma rich in original peritectic orthopyroxene and ilmenite. In contrast, the peritectic plagioclase demanded by the chemistry of the rocks has melted during ascent due to overheating and decreasing water solubility in the melt. The phenocrystic potassium feldspar observed in the rocks crystallised after significant cooling and the physical behaviour of these crystals does not shape the chemistry of the magma. K contents of the ignimbrites are however not well replicated by this modelling, which predicts a significant K decrease due to dilution. K in the rocks is not correlated with maficity. This may reflect the fact that the K behaviour represents two slightly different source protoliths with differing K contents.

Opsomming

Tot op hede is die enigste vulkaniese rots van die Kaapse Granietgroep wat al beskryf is ignimbriete wat teen die westelike grens van die Langebaan-lagune, na die suide van Saldanha, aan die oppervlak kom. Hierdie ignimbriete, met ’n ouderdom van 515 ± 3 Ma, verteenwoordig die jongste gesteentes in die Groep. Die doel van hierdie studie was om die petrogenese van fynkorrelrige granietrots wat na die noorde van die Langebaan-lagune blootgestel is, te ondersoek, en ook die klassifikasie van hierdie rotse as ’n subvulkaniese kwartsporfier- intrusiewe gesteentes te assesseer.

Hierdie gesteentes toon ’n donker grys tot bruin mikro- tot kriptokristalvormige matriks wat prominente veldspaat en kwartsfenokriste bevat wat dikwels bogtig en gebreek is. Fenokriste van biotiet en ortopirokseen (Fs_{50-70}) asook vervanging van albei fases deur chloriet kan mikroskopies geïdentifiseer word. Ilmeniet kom dikwels naby ortopirokseenfenokriste voor. ’n Tweede generasie poikiloblastiese biotiet groei die matriks toe en is duidelik deur subsolidusreaksie gevorm. Die veldspaatfenokriste is gewoonlik mikroklien-mikropertiet. Kontakblootstelling kan in die studiegebied waargeneem word, wat aantoon dat die fynkorrelrige rots ander grofkorrelrige granietgesteentes intrudeer het. Die oorheersing van gebroke fenokriste asook die teenwoordigheid van ‘fiamme’ strukture in die rotsdagsoom met ’n mikrokristalvormige matriks dui op vulkaniese oorsprong, wat aan die hand doen dat hierdie gesteentes as ignimbriete eerder as kwartsporfier geklassifiseer kan word. Hierdie waarnemings en eienskappe kan geïnterpreteer word as verteenwoordigend van ’n gelaste ignimbriet-afsetting wat deur grofkorrelrige graniet onderlê word. Die fynkorrelrige ignimbriet stel dan ’n daaropvolgende intrusie voor deur ’n latere puls van soortgelyke magma teen die kontak met die grofkorrelrige graniet af.

Die ignimbriete is silisies met SiO_2 wat wissel tussen 69 en 76 wt. %; hulle is matig peralumineus met waardes vir ASI (ASI = mol. Al_2O_3/ ($CaO+Na_2O+K_2O$)) wat wissel van 1.02 tot 1.09; en ASI is negatief gekorreleer met Mg + Fe (hierná mafiese komponent). Nou tot baie nou inter-elementkorrelasies bestaan vir verskeie groot elemente asook spoorelemente wanneer dit teen die mafiese komponent gestip word. Die volgende R^2-waardes is van toepassing: Al =0.94; Ca = 0.98; Si = 0.97; Ti = 1.00; Na =0.90; Zr =0.95; La = 0.87. Hierdie elemente is almal positief met die mafiese komponent gekorreleer, buiten Si, wat negatief gekorreleer is.

Ortopirokseen en ilmeniet verteenwoordig vroeg gevormde, hoëtemperatuur-minerale in die magma. In die biotiet-arme rotse stel ilmeniet die hoofreservoir van titaan voor, terwyl ortopirokseen die vernaamste MgO- en FeO-reservoir voorstel. Die buitengewoon nou Ti: mafiese-korrelasie vereis dat albei hierdie minerale altyd in dieselfde molekulêre verhouding in die magma teenwoordig moet wees, ondanks die beduidende omvang van die mafiese komponent wat deur die gesteentes getoon word en ondanks die feit dat hierdie minerale verskillende grootte–digtheidsverhoudings het. Hierdie buitengewoon nou korrelasie kan geredelik geïnterpreteer word om meesleping van ’n peritektiese groep te weerspieël wat uit ilmeniet en ortopirokseen bestaan. Die Al-, Ca- en Na-korrelasies vereis die meesleping van peritektiese plagioklaas. Die verminderende neiging tot ASI vereis die meesleping van

peritektiese klionopirokseen. ’n Byna perfekte passing met die konsentrasies van hierdie elemente in die ignimbriete word voortgebring deur die modellering van meesleping van ’n peritektiese groep bestaande uit plagioklaas, ilmeniet, ortopirokseen en klionopirokseen in stoïgiometriese verhoudings wat deur die smeltreaksie bepaal word. ’n Peritektiese groep wat deur hierdie fases gevorm word, dui op die gedeeltelike smelting van ’n bron wat gekoppelde biotiet- en horingblende- vloeistofafwesige smelting ondergaan, met horingblende wat ondergeskik is.

Die ortopirokseen- en ilmeniet-ryke mikrodomeins in die gesteentes verteenwoordig sones in die magma wat ryk is aan oorspronklike peritektiese ortopirokseen en ilmeniet. Hierteenoor het die peritektiese plagioklaas wat deur die chemie van die gesteentes vereis word tydens styging gesmelt weens oorverhitting en dalende wateroplosbaarheid in die smeltsel. Die fenokristiese kaliumveldspaat wat in die rotse waargeneem is wat ná aanmerklike afkoeling gekristalliseer het en die fisiese gedrag van hierdie kristalle vorm nie die chemie van die magma nie. Die K-inhoud van die ignimbriete word egter nie goed deur hierdie modellering gerepliseer nie, wat ’n aanmerklike K-afname weens verdunning voorspel. K in die rotse is nie met mafiese komponente gekorreleer nie. Dit kan die feit weerspieël dat die K-gedrag twee effens verskillende bronprotoliete met verskillende K-inhoud voorstel.

Acknowledgements

The research for this study was funded by the South African National Research Foundation (NRF) in the form of grant funding to Professor G Stevens via the SARChI programme and an MSc Bursary to C.S.A Joseph.

Prologue

The work contained in this thesis was performed independently by myself under the guidance of my supervisor, Prof Gary Stevens (University of Stellenbosch), and co-supervisors, Dr. Federico Farina (University of Stellenbosch) and Prof John Clemens (University of Stellenbosch).

Contents

Declaration i
Abstract ii
Opsomming iv
Acknowledgements vi
Prologue vii
1 Introduction 1
2 Geological Setting 4
3 Analytical Methods 9
3.1 Fieldwork and Sampling 9
3.2 Whole Rock Chemistry 9
3.3 Trace element Chemistry 10
3.4 Mineral Chemistry 10
4 Field Description 11
4.1 Contacts 13
5 Petrography 15
6 Whole Rock Chemistry 20
6.1 Major Element Chemistry 20
6.2 Trace Element Chemistry 21
6.3 Rare Earth Element Chemistry 25
7 Mineral Chemistry 26
7.1 Feldspar 26
7.2 Biotite 26
7.3 Orthopyroxene 26
7.4 Modelling of Mineral Stability 32
8 Discussion 39
8.1 Petrographic constraints on the origin of the Saldahna Tuffisite-Quartz Porphyry 39
8.1.1 Summary of Textures 39
8.1.2 Obscurity of vitroclastic and eutaxitic features in rheomorphic tuffs 39
8.1.3 Devitrification of volcanic glass 40
8.1.4 Broken phenocrysts 41
8.2 Contacts 41
8.3 Petrogenetic Modelling 42

8.3.1 Major and Trace Element Variability 42
8.3.2 Assessment of Petrogenetic Models 44
9 Conclusion 50
10 References 51
11 Appendices 56
11.1 Appendix 1: Averaged Feldspar Compositions and Standard Deviations 56
11.1.1 Averaged Feldspar Compositions 56
11.1.2 Standard Deviations 58
11.2 Appendix 2: Averaged Pyroxene Compositions and Standard Deviations 60
11.2.1 Averaged Pyroxene Compositions 60
11.2.2 Standard Deviations 62
11.3 Appendix 3: Averaged biotite compositions and Standard Deviations 63
11.3.1 Averaged biotite compositions 63
11.3.2 Standard Deviations 64
11.4 Appendix 4: Whole rock major and trace element chemistry 65
11.4.1 Whole rock major chemistry 65
11.4.2 Trace element chemistry 69
11.5 Appendix 5: Peritectic assemblage entrainment modelling 77
11.6 Appendix 6: Sample Locality Coordinates 78

List of Figures

Figure 1: (a) Paleogeographic reconstruction of the Saldania orogen at 550 Ma (modified after Rozendaal et al. 1999); (b) Geological map of the Cape Granite Suite; CSZ stands for Colenzo Shear Zone, PWSZ for Piketberg-Wellington Shear Zone (modified after Hartnady et al. 1974); (c) A simplified geological map illustrating the distribution of granitic and volcanic phases (modified after Scheepers and Armstrong, 2002) 7

Figure 2: A selection of bivariate diagrams illustrating the elementary geochemical properties for compositions of rocks from Scheepers and Poujol (2002). Red open circles represent volcanic rocks (Postberg ignimbrites) and blue diamonds represent subvolcanic rocks (quartz porphyry) 8

Figure 3: A Google™ earth image illustrating the locations of the sample points represented by the red points and the location of a mapped contact discussed below labelled C. 11

Figure 4(a) Representative image illustrating the general appearance of the main rhyolitic phase studied. Elongate feldspar and quartz dominated domains can be observed as well as

randomly oriented quartz and feldspar dominated veins. (b) An example of a xenolith exposed in outcrop. (c) Polished slab of a porphyritic rock consisting of a fine grained grey coloured matrix with discernible feldspar and quartz phenocrysts. Finer grained elongate domain is illustrated by dashed red outline. (d) Porphyritic rock consisting of a white to light grey coloured matrix with discernible quartz and feldspar phenocrysts as well as distinctive dark grey to black coloured phenocrysts exhibiting an acicular habit. 12

Figure 5 (a) A panoramic image, with the left of the image facing south east and the right facing south, illustrating alternating rock units of coarse grained porphyritic granite. (G) and fine grained felsic (S) facing south. White lines indicate boundaries between granite and fine grained felsic rock. (b) A boundary between fine grained felsic rock unit and porphyritic granite, with alternating lighter and darker bands in what is interpreted to be a chill margin within the finer grained felsic rock. (c) Coarse grained porphyritic granite (G) that has been intruded by veins of finer grained felsic rock which extend from the adjacent fine grained felsic rock (S). (d) A sharp contact between the fine grained felsic rock and the adjacent granite facing west. (e) An enclave of granite within the fine grained felsic rock which exhibits a finer grained chill margin against the coarse grained enclave. 14

Figure 6. Photomicrographs of representative massive fine grained rocks (a-d), finer grained rocks at the contact with the granite (e-f) and a xenolith (i). (a) A perthitic feldspar grain can be observed in the centre exhibiting poorly aligned perthitic exsolutions surrounded by a finer grained groundmass of quartz, albite and acicular biotite. The surrounding phenocrysts are predominantly perthitic and display slight alteration to sericite as does the matrix feldspar imparting a brown colour to the rock in ppl. (b) Orthopyroxene can be seen to exist as anhedral corroded phenocrysts with inclusions of Fe-Ti oxides and coronas of biotite and chlorite or as anhedral inclusions of a much smaller size in surrounding fractured plagioclase and k-feldspar. (c) Two domains which exhibit differences in matrix crystal size with a well defined boundary can be observed. The finer grained matrix contains recrystallized quartz as well as fragmented quartz phenocrysts. (d) Photomicrograph illustrating a fine grained elongate domain surrounded by a finer grained matrix as well as phenocrysts and microphenocrysts of k-feldspar and quartz. (e) Phenocrysts of broken and embayed plagioclase and k-feldspar in a fine grained matrix. Light coloured elongate domains can be observed in the matrix displaying an alignment and curving around the phenocrysts. (f) Photomicrograph across two domains. The upper finer grained domain contains a larger abundance of matrix biotite and chlorite imparting a speckled appearance and resembles a flow texture mainly due to the alignment of matrix biotite and chlorite in near linear patterns. Phenocrystic quartz can be observed which can be seen to be broken and embayed. (g) Fragmented quartz crystals are embedded in a fine grained matrix, with darker bands within the matrix defining an aligned orientation, as well opaque minerals of variable size. (h) Fine grained quartz crystals within a finer grained matrix can be observed. The crystals of quartz are flatted in appearance and show slight alignment. (i) Xenolith consisting of randomly oriented fine grained biotite porphyroblasts in a fine grained matrix. 20

Figure 7. Total Alkali versus Silica diagram (after Le Bas et al., 1986; the alkali-sub alkali line boundary after Irvine and Baragar, 1971), blue circles represent rocks of group one, red diamonds represent rocks of group two. 22

Figure 8: Variation diagrams of major elements plotted against maficity (atomic Fe + Mg). Red diamonds represent rocks of a cryptocrystalline variant (group 2) and blue circles represent rocks of a microcrystalline variant (group 1). 23

Figure 9: Variation diagrams for selected trace elements plotted against maficity. Red diamonds represent rocks of a cryptocrystalline variant (group 1) and blue circles represent rocks of a microcrystalline variant (group 2). 24

Figure 10: Chondrite-normalized REE pattern for rhyolitic rocks. Red diamonds represent group 2 rocks, blue circles represent group 1 rocks 25

Figure 11. Partial P-T phase diagram for the rhyolitic rocks, as exemplified by sample A3, in the system NCKFMASH, using Perplex (Conolly 2009). The heavy dashed line represents the wet solidus. Pseudosection constructed for pressures ranging from 1 to 10 kilobars and temperatures ranging from 600 to 1000 °C. Abbreviations: Bt = biotite, Grt = garnet, Kfs = K feldspar, Pl = plagioclase, Opx = orthopyroxene, Crd = cordierite, Qtz = quartz, Ph = phengite (after Kretz, 1983). 34

Figure 12: Partial P-T phase diagram for the rhyolitic rocks, as exemplified by sample A3, in the system NCKFMASH, using Perplex_X (Conolly 2009). The heavy dashed line represents the wet solidus. Pseudosection constructed for pressures ranging from 1 to 4.6 kilobars and temperatures ranging from 700 to 900 °C. Abbreviations: Bt = biotite, Grt = garnet, Kfs = k feldspar, Pl = plagioclase, Opx = orthopyroxene, Crd = cordierite, Qtz = quartz, Ph = phengite (abbreviations after Kretz, 1983). 35

Figure 13: Partial P-T phase diagram for the rhyolitic rocks, as exemplified by sample A3, in the system NCKFMASH, using Perplex_X (Conolly 2009). The heavy dashed line represents the wet solidus. Contours for the volume % orthopyroxene are illustrated on the pseudosection. Abbreviations: Bt = biotite, Grt = garnet, Kfs = k feldspar, Pl = plagioclase, Opx = orthopyroxene, Crd = cordierite, Qtz = quartz, Ph = phengite (abbreviations after Kretz, 1983). 36

Figure 14: Partial P-T phase diagram for the rhyolitic rocks, as exemplified by sample A3, in the system NCKFMASH, using Perplex_X (Conolly 2009). The heavy dashed line represents the wet solidus. Contours for the Al_2O_3 content of orthopyroxene are illustrated on the pseudosection. Abbreviations: Bt = biotite, Grt = garnet. Kfs = k feldspar, Pl = plagioclase, Opx = orthopyroxene, Crd = cordierite, Qtz = quartz, Ph = phengite (abbreviations after Kretz, 1983). 37

Figure 15: Partial P-T phase diagram for the rhyolitic rocks, as exemplified by sample A3, in the system NCKFMASH, using Perplex_X (Conolly 2009). The heavy dashed line represents

the wet solidus. Contours for Mg # of orthopyroxene are illustrated on the pseudosection. Abbreviations: Bt = biotite, Grt = garnet, Kfs = k feldspar, Pl = plagioclase, Opx = orthopyroxene, Crd = cordierite, Qtz = quartz, Ph = phengite (after Kretz, 1983). 38

Figure 16: Variation diagrams of major elements plotted against maficity. Data plotted represents rock compositions obtained for this study as well as rock compositions obtained from Scheepers and Poujol (2002) described as subvolcanics and volcanics. 43

Figure 17: Major element plots of the rocks of this study against maficity. Plots show's vectors calculated for the fractionation of 8% biotite, 1% ilmenite, 5% plagioclase and 3% orthopyroxene phenocryst phases. Circles represent rocks of group one and the red squares represent rocks of group two.....46

Figure 18: The rock compositions of this study compared with the magma compositions produced by peritectic assemblage entrainment (blue circles). The trend resulting from the mol% of peritectic assemblage entrained to the magma is indicated by the red circles as illustrated in the legend provided.....49

List of Tables

Table 1: Table summarising the different documented phases of magmatism in the Saldania Belt (Rozendaal et al., 1999; Scheepers and Armstrong, 2002). 5

Table 2. Representative major and trace element compositions of rocks sampled.....24

Table 3. Averaged ($\sigma<1$) compositions of selected feldspar phenocryst crystals. Analyses of exsolutions are also provided as well analyses of the host grain.....28

Table 4. Averaged ($\sigma<1$) compositions of selected biotite crystals. 29

Table 5. Averaged ($\sigma<1$) compositions of selected pyroxene crystals. A rim and core analyses is also provided.....30

1 Introduction

The interpretation of compositional variation displayed by granitic rocks has been a major focus of investigation in igneous petrology. There remains no consensus on the dominant processes proposed to explain the observed geochemical diversity in suites of comagmatic granitoid rocks that commonly range in composition from leucogranite to granodiorite. This lack of consensus is evident in the number of differing models which have been proposed to explain such variations.

The models that have been proposed to explain the compositional variation displayed by granites can be subdivided into two different types which reflect two contrasting broad sets of views within the granite petrology research community. The first type constitutes a set of models which considers the chemical variability shown by granitic rocks to be the result of different petrogenetic processes that occur within the magma. These include crystal liquid fractionation, assimilation of country rock and mixing between magmas from different sources. Chemical variation is considered to reflect the influence of these processes after the segregation of a chemically homogenous melt from its source. The second set of models is based on the idea that the chemistry of granitic magmas is inherited from the source. Following this view, the chemical variability in granitic magmas is considered to be controlled by the source chemistry and melting reaction, which determines the melt composition (Stevens et al., 2007), as well as the entrainment of either the unmelted residual fraction of the source (White and Chappell, 1977) or the peritectic assemblage produced by the melting reaction (Stevens et al., 2007).

Certain features or observations are often regarded as unequivocal evidence for the operation of models of the first type. These features are usually enclaves, flow structures and evidence of mineral disequilibrium in the case of magma mixing (e.g. Perugini and Poli, 2012; Poli and Tommasini, 1999) and compositional zonation in well exposed suites of rocks, e.g. exhibiting ranges in composition from basalt to rhyolite, in the case of fractionation in volcanic suites for example (e.g. Ustunisik and Kilinc, 2011, Aydar and Gourgaud, 1998). Experimental and theoretical considerations have revealed rheological, thermal and dynamic limitations on mixing. These considerations have found that mixing is most likely to occur between magmas which are of similar viscosities, temperatures, compositions and densities, and that the products are most likely to be only moderately silicic hybrids (Bateman, 1995). To compensate in part for these limitations as well as inadequacies in accounting for observed geochemical trends, models which assume the concurrent or consecutive operation of a combination of these processes have been proposed, e.g. assimilation and fractional crystallisation (e.g. De Paolo, 1981) and mixing and fractionation (e.g. Bateman, 1995; Poli, 1999). Similarly, challenges brought against fractional crystallisation has led to the proposition of several physical mechanisms which have been proposed to facilitate crystal-liquid segregation and include simple gravitational crystal settling (e.g. Bowen 1928) through sidewall crystallization and ‘‘liquid fractionation’’(McBirney et al. 1985),solidification front formation and melt extraction (e.g., Marsh 1989, 2002) and decompression induced crystallization (e.g. Brophy, 2009). Brophy (2009) proposed a general fractional

crystallization process of ascent, volatile exsolution, crystallization, congestion and eventual liquid extraction for calc alkaline magmas in subduction zones with two stages of congestion and interstitial melt extraction.

Chappell and White (1974) proposed a subdivision of granites into an S- and I-type based on the inference of observed geological and petrological features of a rock or a suite of rocks being inherited from the source material from which they are derived. S-type granites were proposed to be derived from magmas generated by partial melting of sedimentary source rock and I-types from the partial melting of a mafic to intermediate igneous rock. The critical implication of this classification was the recognition of contrasting source rocks and their control on the observed geochemical variation in the magmas. White and Chappell (1977) consequently proposed the restite model which is based on the idea that unmelted and magmatically equilibrated source material (restite) may be entrained by a partial melt and that differences in the ratio of melt to restite are responsible for the variation in composition in many granite suites. The restite model was proposed to explain the compositional variation that is displayed by granites in the Lachlan Fold Belt. Unlike the I and S classification scheme and its implication, the restite model has received little to no acceptance. Arguments by many authors (e.g. Wall et al., 1987 and Collins 1998) have been brought against the restite model since its conception which centres on the misinterpretation of non-restitic components as restite. An example is the interpretation of metasedimentary xenoliths as restite. These enclaves do not have the expected melt-depleted compositions and contain biotite which has been interpreted to suggest a mid-crustal origin as supposed to a restitic origin which should not contain biotite as it would break down during most types of partial melting. (e.g., Clemens and Wall, 1981; Clemens and Vielzeuf, 1987; Clemens and Watkins, 2001).

The models listed above have been proposed to account for the linear major element arrays exhibited on binary plots by rocks within granitic suites. The significance of these models (e.g. magma mixing, crystal fractionation and restite unmixing) in producing the large scale geochemical variation observed in comagmatic granitic rocks is however debatable as demonstrated by Stevens et al. (2007). These models cannot adequately account for compositional parameters such as Ti and Zr which are well correlated with maficity in all granites, and which define a very narrow range of ratios, particularly in S-type granites. The strong positive correlation between Ti and maficity matches that defined by the stoichiometry of high-temperature biotite. Ti in granites is hosted in more than one mineral, typically biotite and ilmenite in S-type magmas and biotite ± hornblende and ilmenite ± titanite in I-type magmas. These minerals exhibit substantially different crystal size-density relationships and appear at different stages in the crystallization sequences. The exceptionally tight Ti: maficity correlation requires that the relevant minerals always be present in the same proportions in the magma which is very unlikely in a magma mixing, assimilation or fractional crystallization scenario considering the previous consideration. The one fractional crystallization process that will produce the observed Ti: maficity ratio in biotites is the fractional crystallization of approximately 4.5 wt% TiO_2 biotite. This would produce rocks with a positive correlation between K and maficity and the opposite is universally observed in

granites. Similarly zirconium solubility as a function of temperature and melt composition cannot account for the tight Zr-maficity correlation that exists in S-type granites given that a high fraction of zircons observed in S-type granites, such as those of the Peninsular pluton of the Cape Granite Suite (hereafter referred to as CGS), are inherited (Villaros et al., 2009). A significant proportion of the leucocratic compositions, which are proposed by Stevens et al. (2007) to most closely match pure melts, are zircon undersaturated whereas the more mafic compositions are zircon oversaturated. For the leucocratic rocks to have evolved from a more mafic precursor, these rocks would have to inherit the zircon saturated character of the hypothetical mafic precursor, which is not the case (Villaros et al., 2009).

The principal difference between models of restite unmixing and peritectic assemblage entrainment is that in the case of the latter the admixture is defined by the stoichiometry of the melting reaction and the former by the composition of the source. Stevens et al. (2007) demonstrated that the majority of S-type granites have maficity values that are too high to represent melts and that the more mafic magmas would therefore require the addition of a Fe and Mg component to the magma. It was consequently proposed that the most likely mechanism to account for the observed variation (e.g. Ti versus maficity) would be the entrainment of the solid, peritectic products of the melting reaction (e.g. ilmenite and garnet in the case of pelite-derived S-type magmas). These peritectic phases are known to be the products of high-temperature, incongruent, fluid-absent melting from experimental studies and studies of migmatites. The magma composition is as a result controlled by the stoichiometry of the melting reaction and the degree of peritectic assemblage entrainment. Clemens and Stevens (2012) noted that in I-type granites and in some S-type granites entrainment of peritectic plagioclase can be identified on the basis of positive correlations between Al and Ca with maficity, despite, in case of the I-type rocks, decreasing A/CNK as a function of maficity. In essence, peritectic assemblage entrainment produces magma compositions that define a mixing line between melt compositions and the peritectic products of the melting reaction. In contrast, the restite entrainment and unmixing produces magma compositions which form mixing lines between melt and the entire unmelted fraction of the source. Source rocks for I and S-type granites have a very wide range of Ti: maficity ratios, yet the Ti: maficity ratios defined by I and S-type granites fit well with the stoichiometry of biotite and hornblende and biotite incongruent melting reactions respectively (Stevens et al., 2007; Clemens et al, 2011; Clemens and Stevens, 2012). This clearly indicates that the source control on granite chemistry, apart from source influence on melt compositions, is peritectic assemblage entrainment, not restite entrainment.

The granitic rocks of the Cape Granite Suite have formed the basis for investigations which have facilitated the understanding of peritectic assemblage entrainment as a petrogenetic process. The felsic volcanic and subvolcanic rocks constitute finer grained granitic rocks of the CGS whose petrogenesis has not been investigated in detail. Recent work which has been conducted on the petrogenesis of peraluminous granites of the CGS provides a good basis for petrogenetic investigation for the felsic volcanic rocks of this study.

A peraluminous rhyolitic volcanic-hypabyssal phase which marked the end of the Saldanian magmatic event is presently exposed as large ignimbrite flows, tuffisite and quartz porphyry

around the town of Saldahna (Scheepers and Nortjé, 2000). The study aims to investigate the petrogenesis of these rocks which has not been previously considered. In the process the study will contribute to the development of a more complete understanding of the formation and petrogenesis of the CGS. The study also aims to address the current classification of these rocks as quartz porphyry.

2 Geological Setting

The Saldania Orogeny forms part of the Pan-African crustal evolutionary sequence in southern Africa and is exposed as inliers of older metasedimentary and metavolcanic rocks (Malmesbury Group) intruded by gabbro, diorite, granite and quartz syenite. These rocks are partly covered by Ordovician to Silurian (Cape Supergroup) aged sediments that were pervasively affected by the Permo-Triassic Cape Fold orogeny (Gresse et al., 1992; Barnett et al., 1997; Scheepers and Armstrong, 2002).

The CGS granites are intrusive into the Malmesbury Group (Scheepers and Armstrong, 2002). The regional metamorphic grade of the Malmesbury Group is greenschist facies (Scheepers and Armstrong, 2002). The Malmesbury Group can be subdivided into three terranes separated by prominent northwest-trending shear zones. All three terranes are comprised of low-grade metamorphic Neoproterozoic metasediments and subordinate metavolcanic rocks (Belcher and Kisters, 2003). These terranes are the northeastern Boland terrane, the central Swartland terrane and the southwestern Tygerberg terrane (Hartnady et al., 1974). Von Veh (1983) observed ductile, dextral strike-slip shearing preceding the intrusion of the oldest granites in the Tygerberg terrane (Scheepers and Armstrong, 2002). Sinistral strike-slip movement (during the period 550-520 Ma) affected the intrusion of both late S- as well as I-type granites, particularly along the Colenso fault and in the Swartland terrane.

Sinistral shearing in the Saldahna belt continued after the intrusion of post-orogenic to anorogenic A-type granitoids between 525-510 Ma (Scheepers and Armstrong, 2002). These late Neoproterozoic plutons and batholiths can be divided into three geographic groups exposed in the eastern, southwestern and northern areas of the Cape Province of South Africa (Scholtz, 1946). The granitoids of the Cape Granite Suite are interpreted to have intruded in a continental-arc setting, during and shortly after the main phase of Pan-African collisional tectonics (Gresse and Scheepers, 1993). A geological map which illustrates the distribution of the Cape Granites is shown in Figure 1.

Scheepers and Rozendaal (1992) and Gresse and Scheepers (1993) envisaged three major phases of magmatism in the Saldania Belt on the basis of: internal structure, relationship with enclosing rocks and geochemical features. Scheepers and Nortjé (2000) added an additional rhyolitic phase. A summary of these phases is presented in the following table.

Table 1: Table summarising the different documented phases of magmatism in the Saldania Belt (Rozendaal et al., 1999; Scheepers and Armstrong, 2002).

Magmatism	Association	Rock Type	Examples
Phase IV 515 Ma	Volcanic	Ignimbrite, tuffisite, quartz porphyry	Postberg ignimbrite, Saldahna quartz porphyry
Phase III 520 Ma	Aa	Alkali feldspar granite, quartz syenite	Klipberg granite
	Ab	Alkali feldspar granite	Cape Columbine granite
Phase II 540-520 Ma	Ib	Granite, alkali feldspar granite	Paarl fine grained granite, Slippers Bay Granite
	Ia	Monzogranite, granite, alkali feldspar granite	Paarl coarse- and medium – grained granite, Vredenburg monzogranite Greyton pluton
Phase I 555-540Ma	Sb	Granite	Trekoskraal granite, Karnberg, Rondeberg granite, Coarse porphyritic Darling Granite
	Sa_2	Granite, alkali feldspar granite	Stellenbosch fine grained granite, Contreberg granite, Olifantskop granite
	Sa_1	Granite	Hoedjiespunt granite, Seeberg granite, Peninsula granite

The first phase consists of syn- to late-tectonic granites with S-type characteristics which mainly intrude the Tygerberg terrane (Scheepers and Armstrong, 2002).The second phase consists of late-tectonic I-type granites with ages of between 540-520 Ma (Da Silva et al, 2000), presently found in the Swartland and Boland terranes. The third phase consists of A-type granites with ages that are younger than 520 Ma (Scheepers and Armstrong, 2002) currently exposed in the Tygerberg and Swartland terranes (Scheepers and Armstrong, 2002). The fourth and final phase consists of peraluminous S-type volcanic and subvolcanic rocks exposed in the Tygerberg terrane (Scheepers and Nortjé, 2000). This final magmatic phase is characterised by the extrusion of rhyolitic to rhyodacitic peraluminous felsic volcanics present as large ignimbrite flows as well as quartz porphyries and tuffisites (Scheepers and Armstrong, 2002). The felsic volcanics yielded an age of 515±3 Ma (Scheepers and Poujol, 2002).

Scholtz (1946) described a major lithological unit which extends over an area of ±250km^2 as a high level intrusive rock and classified it as “Saldahna quartz porphyry”. Scheepers and Poujol (2002) illustrated intrusive relationships between the “quartz porphyry” and granite

(i.e. Hoedjiespunt granite). They interpreted the “quartz porphyry” as the younger phase based on the presence of enclaves of Hoedjiespunt granite in the “quartz porphyry”. They stated that a high variability in the textural and mineralogical features away from these intrusive contacts is exhibited, which in part is due to a difference in matrix grain size variation, and proposed the term Saldahna tuffisite for rocks which contained flow banding, fragmented crystals and a cryptocrystalline matrix. In addition rocks with a cryptocrystalline matrix were found to exhibit perlitic structures and spherules with the matrix becoming microcrystalline further away from these intrusive contacts. They further stated that the rocks previously considered as subvolcanic were indistinguishable from their volcanic counterparts in many instances. Where the intrusive nature of the rock is evident the term “quartz porphyry” was used. It was concluded that the emplacement of these tuffisites was a direct result of a major amount of degassing of the magma chamber which caused a reduction in magma flow with the chocking of vents in some places creating a rock type with subvolcanic features. An example subvolcanic textures described were rims of finer grained matrix minerals grading to larger sizes away from the phenocrysts interpreted to be a quench texture.

Selected major element plots against maficity are illustrated in Figure 2 for volcanic and subvolcanic rock samples from Scheepers and Poujol (2002). The samples that were evaluated are peraluminous (A/CNK>1) with Ti, Ca and Na being positively correlated as a function of increasing maficity, and Si decreasing as a function of increasing maficity. The plot of Na against maficity shows the subvolcanics forming two parallel trends with a similar slope which extends from a cluster of volcanic compositions. A similar trend is displayed for A/CNK plotted against maficity with the slopes exhibited by the subvolcanic rocks being negative. The plot of K displays two inverse trends for the respective rock types plotted against maficity (fig. 2). Two apparent geochemical trends observed in these plots seems to suggest at least two different geochemical suites in the suite of rocks sampled, the first being what is referred to as volcanics (Postberg Ignimbrite) and the second subvolcanic rocks (quartz porphyry). The volcanic rocks occupy a smaller range in maficity and display a slightly larger scatter compared to the rocks classified as subvolcanic. There exists an overlap between subvolcanic and volcanic rocks within trends for major elements. Scheepers and Poujol (2002) interpreted the observed arrays to represent linear depletion trends when plotted against SiO_2 for the subvolcanic rocks with the process proposed to account for these trends being fractional crystallization and the clustering of volcanics were noted to show lesser evidence of fractionation.

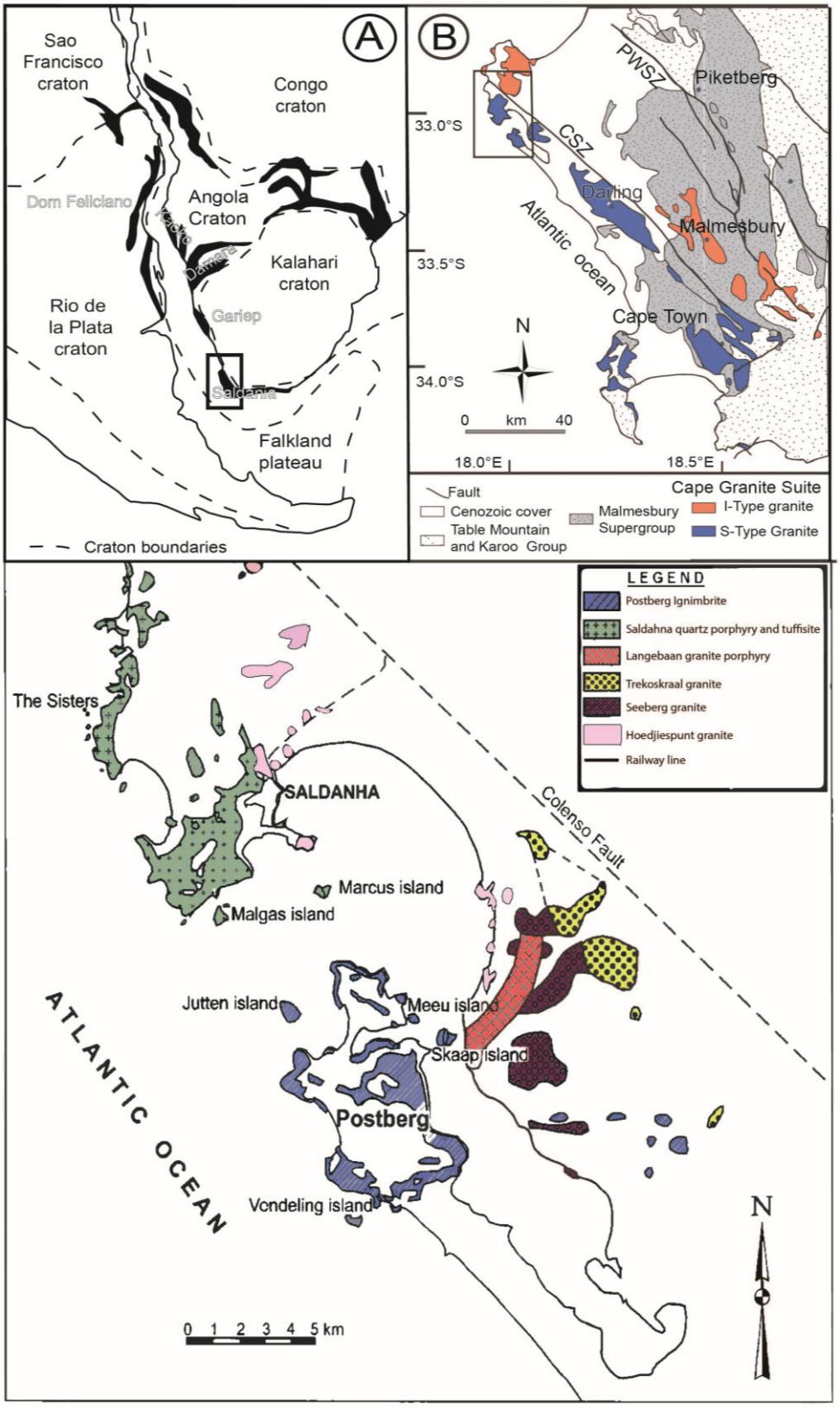

Figure 1: (a) Paleogeographic reconstruction of the Saldania orogen at 550 Ma (modified after Rozendaal et al. 1999); (b) Geological map of the Cape Granite Suite; CSZ stands for Colenzo Shear Zone, PWSZ for Piketberg-Wellington Shear Zone (modified after Hartnady et al. 1974); (c) A simplified geological map illustrating the distribution of granitic and volcanic phases (modified after Scheepers and Armstrong, 2002).

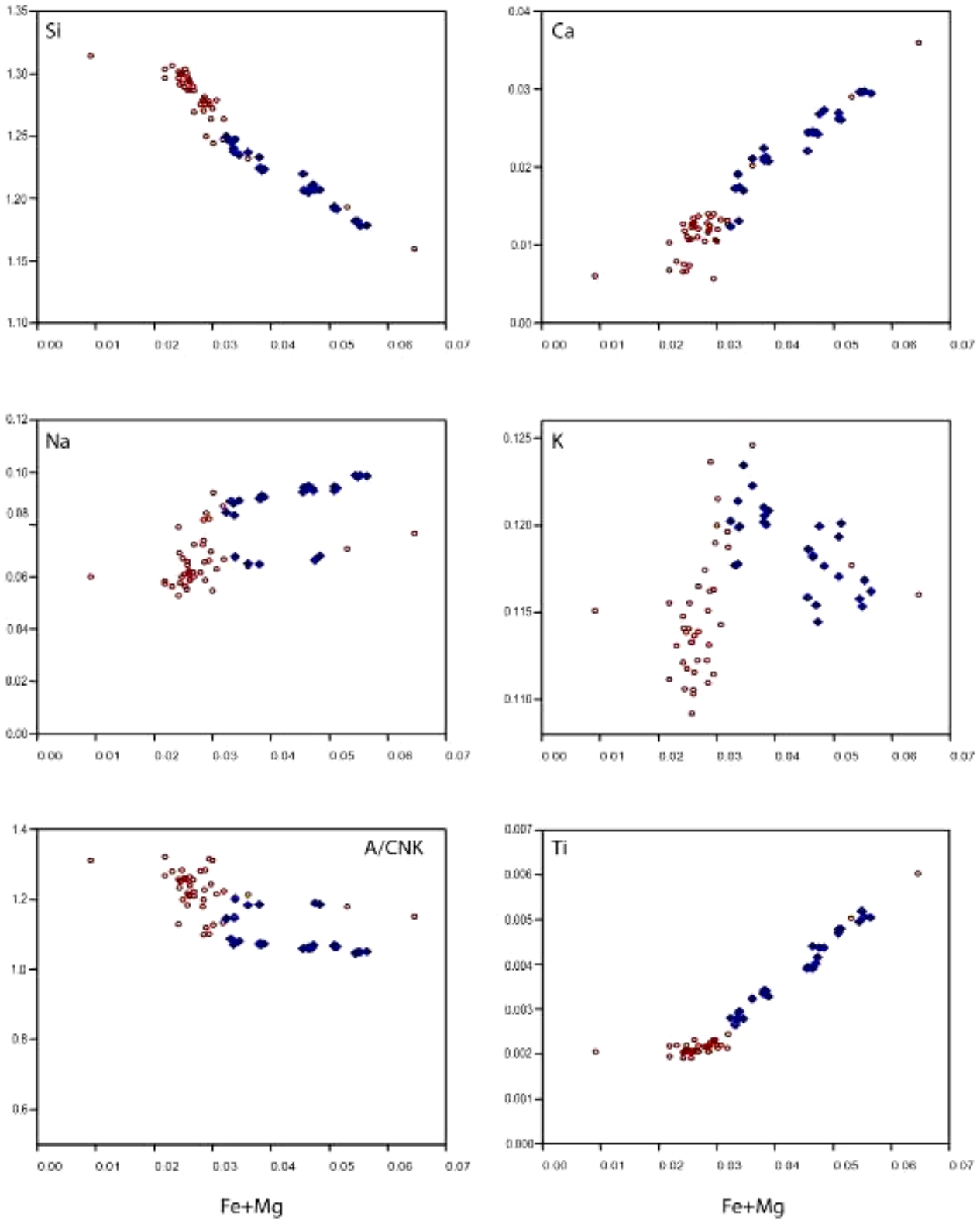

Figure 2: A selection of bivariate diagrams illustrating the elementary geochemical properties for compositions of rocks from Scheepers and Poujol (2002). Red open circles represent volcanic rocks (Postberg ignimbrites) and blue diamonds represent subvolcanic rocks (quartz porphyry).

3 Analytical Methods

3.1 Fieldwork and Sampling

Geological mapping and sampling was conducted over the study area comprising of the rocks previously mapped as Saldahna quartz porphyry and was carried out during the months of May and June in 2011 and April in 2012. Fieldwork was conducted on foot . A total of 56 samples were collected and analysed for this study. Individual waypoints were taken at each sample location. Samples were further collected in instances were a change in either texture or mineralogy could be discerned with the aid of a magnifying lens. A subset of 45 samples were found to be Saldahna quartz porphyry whilst the remaining 11 were found to be intrusive porphyritic granites and were not included in this study. Of the 45 samples, two groups were initially distinguished on the basis of acicular biotite being absent or present. In both groups, quartz and k feldspar phenocrysts could be identified in hand specimen, with the surrounding matrix having a crystalline structure which was not discernible in hand specimen. Rocks of the first group containing acicular biotite were found throughout the extent of the study area whereas rocks of the second group which did not contain any discernible acicular biotite were predominantly found along the coastline south of the town of Saldahna as well as within the town. The distribution of both sample groups as well as sample localities can be observed in Figure 3 below.. Rock samples weighing approximately 5 to7 kg of rock was collected for each sample. Samples were rinsed to remove dirt and rock dust. Weathered sections were removed from each sample with the use of a rock saw. Thin sectioning blocks were subsequently cut and sent to the University of Cape Town for thin sectioning. The remaining sample weighing approximately 4 to 5 kg was considered for geochemical analyses.

3.2 Whole Rock Chemistry

A total of 56 samples were analysed. Samples are crushed with a jaw crusher and subsequently milled into a fine powder (particle size < μm) in a tungsten mill. The jaw crusher and mill were cleaned with pure quartz and acetone after processing each sample to avoid cross contamination. Glass disks were prepared for XRF analysis using 10 g of high purity trace element and REE element free flux ($LiBO_2$ = 32.83%, $Li_2B_4O_7$ = 66.67%, LiI = 0.50%) mixed with 1g of the rock sample. Whole-rock major element compositions were determined by XRF spectrometry on a PANalytical Axios Wavelength Dispersive spectrometer at the Central Analytical Facilities, Stellenbosch University, South Africa. The spectrometer is fitted with an Rh tube and with the following analyzing crystals: LIF200, LIF220, LIF420, PE, and PX1. The instrument is fitted with a gas-flow proportional counter and a scintillation detector. The gas-flow proportional counter uses a 90% Argon, 10% methane gas mixture. Major elements were analyzed on a fused glass disk at 50 kV and 50 mA tube operating conditions. Matrix effects in the samples were corrected for by applying theoretical alpha factors and measured line overlap factors to the raw intensities measured with the SuperQ PANalytical software. Control standards that were used in the calibration procedures for major element analyses were NIM-G (Granite from the Council for Mineral Technology, South Africa) and BHVO-1 (Basalt from the United States Geological Survey, Reston).

3.3 Trace element Chemistry

Trace element compositions were obtained from the same fused beads used for major element determination by applying the method described by Eggins (2003) and analysed using an Agilent 7500ce ICP-MS coupled with an Nd-YAG 223 nm New Wave LASER ablation (LA) system operating at a 12 Hz frequency with a mixed He-Ar carrier gas. Three analyses (each comprising a 30 s blank followed by data collection for 60 s) on each whole rock fused disc were obtained using a 100 μm diameter aperture, and the results averaged. After every three samples (i.e. every 10th analysis) NIST612(Pearce et al. 1997) glass bead was analysed as a calibration standard, in addition to fused discs of NIM-G (granite) and BHVO-1 (basalt) that were analysed as secondary standards. Data were collected in time-resolved mode and were reduced using the SiO2 content measured by XRF as the internal standard. For each element, the reproducibility of replicate analyses of the samples, and deviation from the certified values of the secondary standards are less than10 %, and mostly less than 5 % relative.

3.4 Mineral Chemistry

Major element compositions of phenocrysts selected for this study were analysed with the use of a Leo® 1430VP Scanning Electron Microscope at the Department of Earth Sciences, University of Stellenbosch, South Africa. Textures were studied in backscattered electron (BSE) mode and mineral compositions quantified by EDX (Energy Dispersive X-ray) analysis using an Oxford Instruments ® 133 keV ED X-ray detector and Oxford INCA software. Beam conditions during the quantitative analyses were 20 kV accelerating voltage and 8.0 nA probe current, with a working distance of 8.5 mm and a specimen beam current of 11 nA. X-ray counts were typically ~5000 cps, and the counting time was 50 s live-time. Analyses were quantified with the use of natural mineral standards. Mineral chemical compositions obtained in weight percent of oxides were recalculated to mineral stoichiometries to obtain resultant mineral structural formulae. Comparisons between measured and accepted compositions of control standards within this laboratory, as a reflection of the accuracy of the analytical technique, have been published by Moyen et al. (2006).

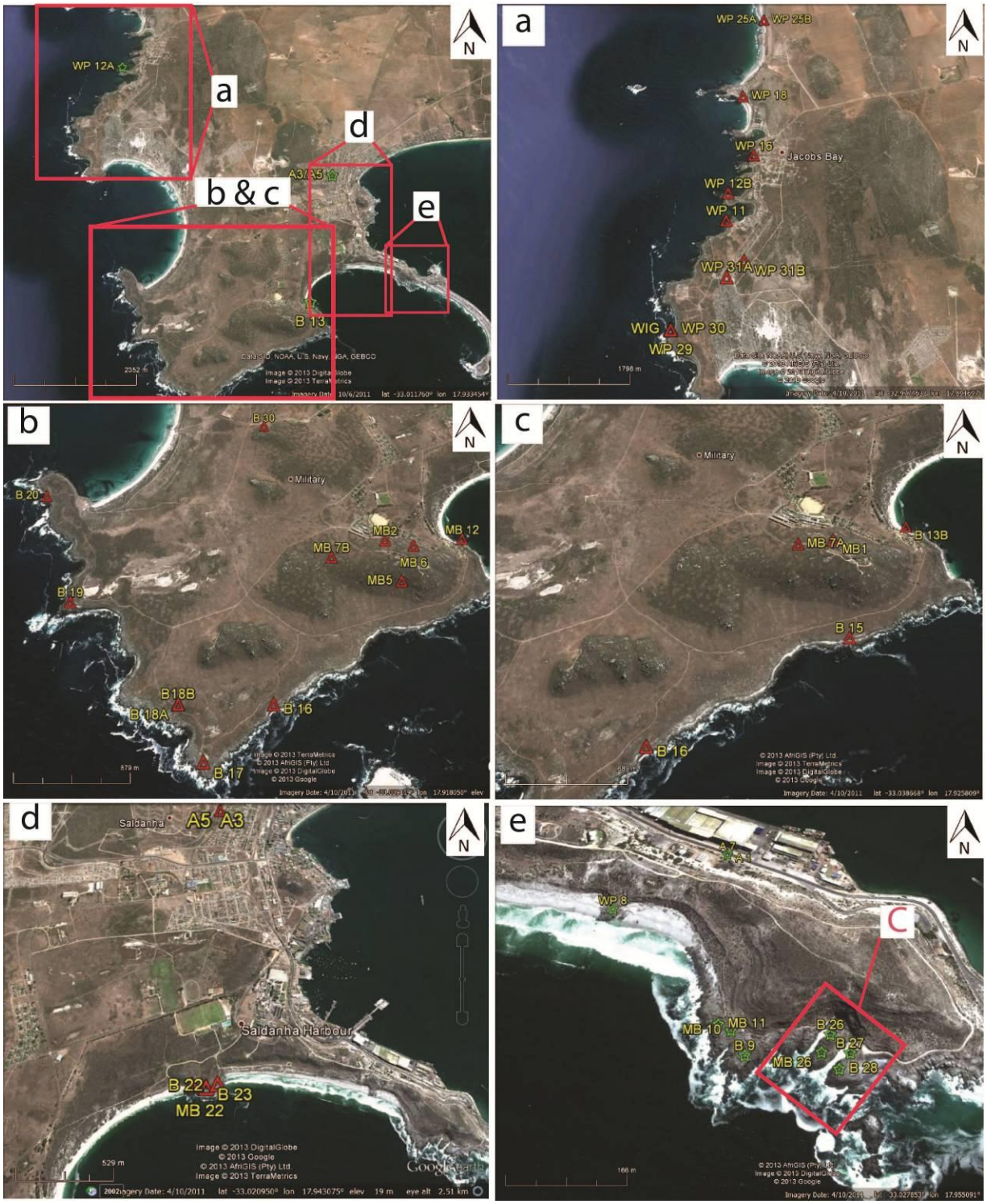

Figure 3 : A collection of Google™ earth image's illustrating the locations of the sample points, represented by red triangles for rocks of the first group, and green stars for rocks of the second group. Figure 3 (e) illustrates the location of a mapped contact discussed below labelled C.

4 Field Description

The exposures of felsic fine grained rocks in the Saldahna area occur most prominently along the coastline. Extensive units of outcrop are tens to hundreds of metres in length and tens of metres in width and are separated by sections of sandy beach. Further inland they occur as

deeply altered cliff exposures with rocks exhibiting a thick carapace of alteration which is progressively less intense at lower altitudes. The rocks are massive and grey to light grey in appearance and display no evidence of layering in the largest exposures. Many spaced shallow fractures can be observed in most outcrop as well as randomly oriented quartz veins. The rocks are porphyritic and exhibit two textures according to the size of the matrix that are either fine or very fine grained. The two textures can be distinguished in the field based on the absence or presence of acicular phenocrysts as illustrated in Figure's 4 (c) and (d) respectively.

Distinctive features which can be observed in the field are oriented elongate feldspar and quartz dominated domains (~10 cm in length) lighter in colour (fig 4a) than the host rhyolitic rock and fine grained xenoliths (fig. 4b). No distinct internal volcanic features (e.g. eutaxitic textures and glass shards) were observed in outcrop for the rocks comprising this study.

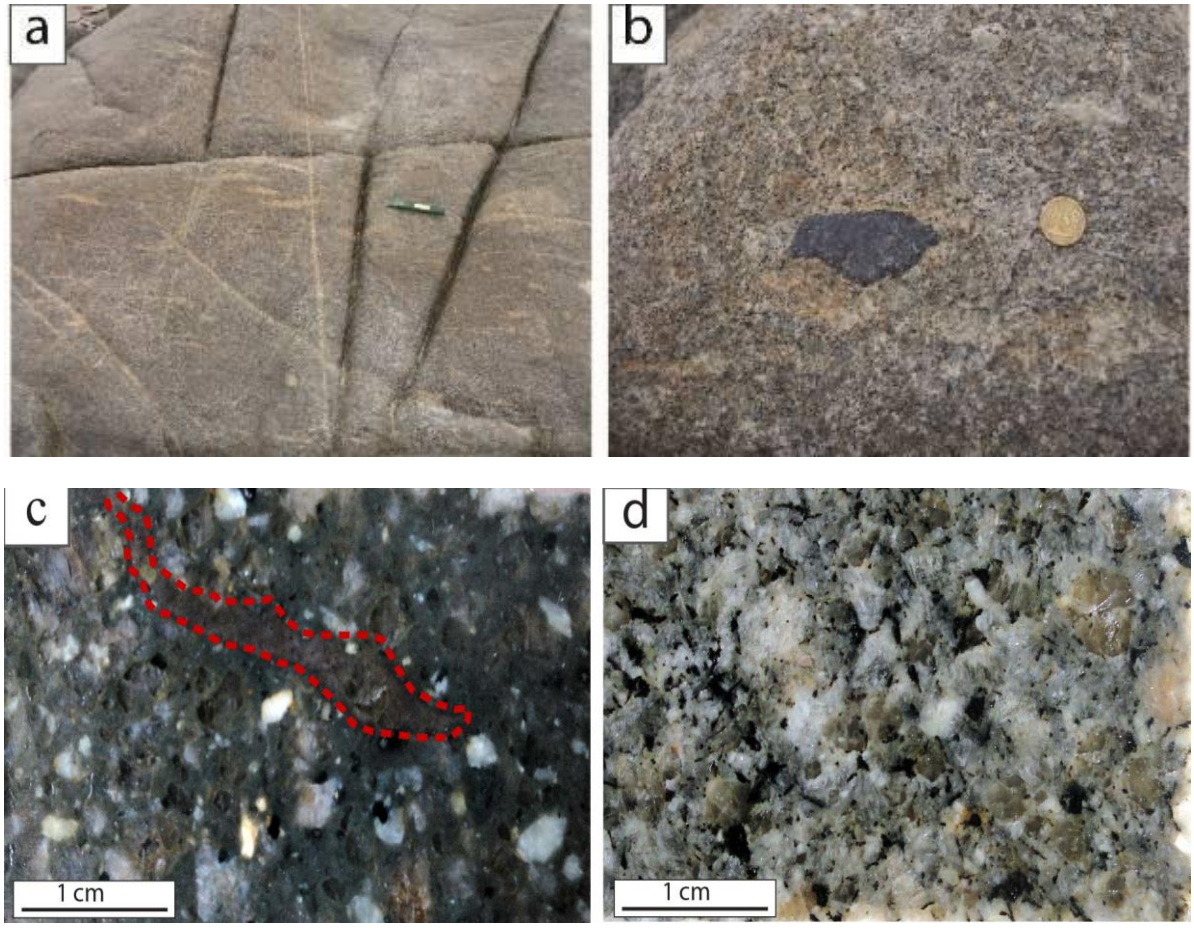

Figure 4(a) Representative image illustrating the general appearance of the main rhyolitic phase studied. Elongate feldspar and quartz dominated domains can be observed as well as randomly oriented quartz and feldspar dominated veins. (b) An example of a xenolith exposed in outcrop. (c) Polished slab of a porphyritic rock consisting of a fine grained grey coloured matrix with discernible feldspar and quartz phenocrysts. Finer grained elongate domain is illustrated by dashed red outline. (d) Porphyritic rock consisting of a white to light grey coloured matrix with discernible quartz and feldspar phenocrysts as well as distinctive dark grey to black coloured phenocrysts exhibiting an acicular habit.

4.1 Contacts

Several exposures illustrate contact relationships between coarse grained porphyritic granite and a fine grained felsic rock with prominent quartz and feldspar phenocrysts. These exposures occur as opposing faces along a series of gullies at location C marked on Figure 3. The contact region is approximately 80 metres in length and 50 metres in width. The contacts mark a boundary between the porphyritic granitic rocks found south of the contact and the fine and finer grained felsic rocks exposed towards the north. An example of one of these faces across which contacts can be observed is illustrated in Figure 5. Splays of fine grained felsic rock of uneven thickness alternate with the granite. These splays have a variable width (1-5 metres) and commonly broaden towards the base situated in between units of granite which narrow towards the base, with a variable width of 1-5 metres (fig 5(a)).

On one of the faces facing North, a basement of deformed brecciated granite, dark green in colour can be observed.

The units of fine grained felsic rock exhibit a finer grained, banded texture towards the boundaries with the adjacent granite. A textural description with accompanying photomicrographs is provided for samples taken across this banded layer as well as the narrow “veins” of finer grained felsic rock which extend through the granitic units (fig 5(c)). Enclaves of granite (fig 5(e)) are abundant in the adjacent subvolcanic units and exist in two varieties. The first variety consists of larger fragmented enclaves of porphyritic granite which are lenticular in shape and exhibit lengths averaging ~5 metres and widths of ~1 metre. The second variety consists of enclaves which are circular in shape with diameters ranging from 10 centimetres to 50 centimetres. The smaller enclaves exhibit finer grained contact zones in some instances and sharp contacts with the host rock in others. The granites do not contain enclaves of the finer grained rock.

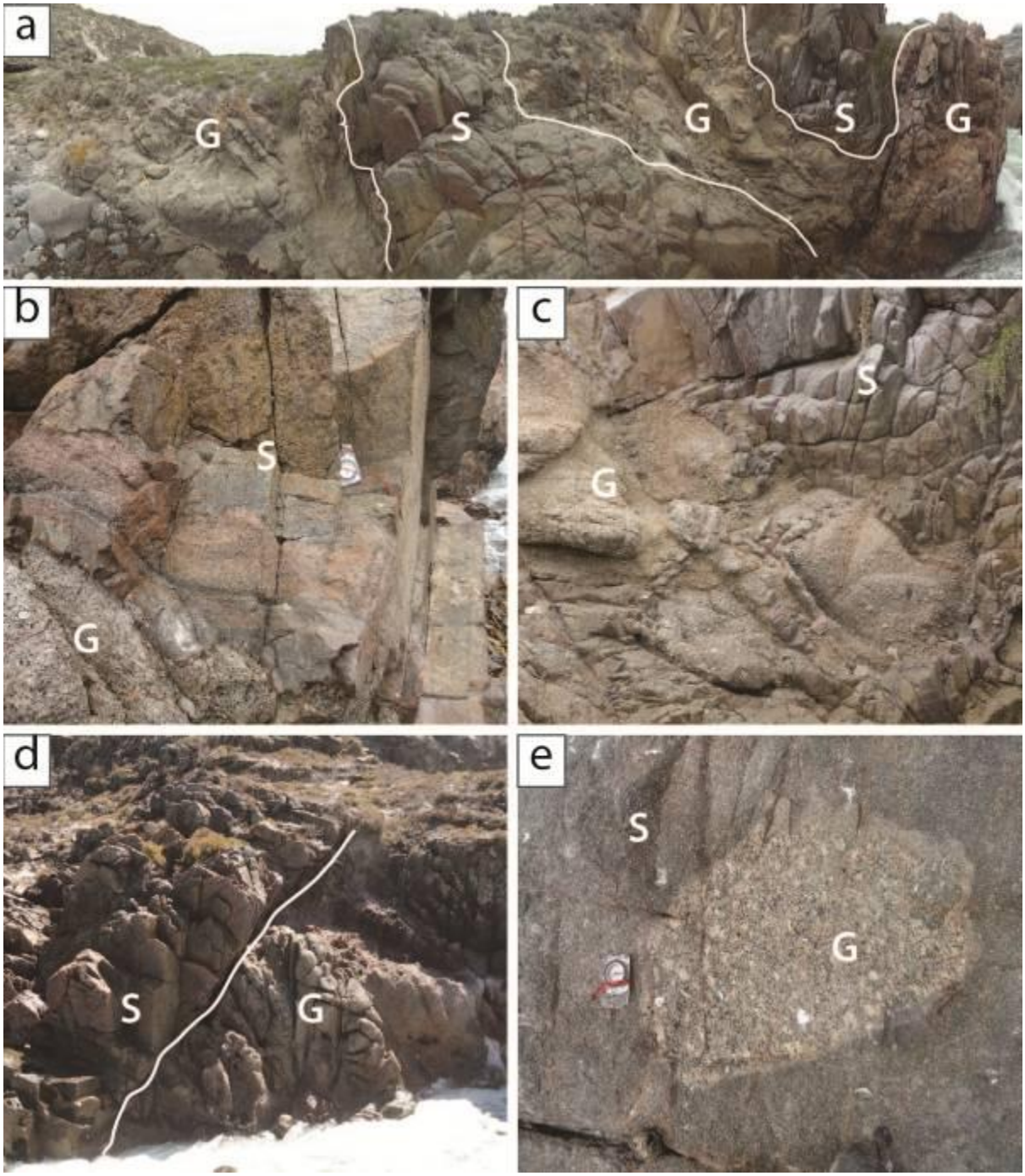

Figure 5 (a) A panoramic image, with the left of the image facing south east and the right facing south, illustrating alternating rock units of coarse grained porphyritic granite. (G) and fine grained felsic (S) facing south. White lines indicate boundaries between granite and fine grained felsic rock. (b) A boundary between fine grained felsic rock unit and porphyritic granite, with alternating lighter and darker bands in what is interpreted to be a chill margin within the finer grained felsic rock. (c) Coarse grained porphyritic granite (G) that has been intruded by veins of finer grained felsic rock which extend from the adjacent fine grained felsic rock (S). (d) A sharp contact between the fine grained felsic rock and the adjacent granite facing west. (e) An enclave of granite within the fine grained felsic rock which exhibits a finer grained chill margin against the coarse grained enclave.

5 Petrography

The fine grained rocks of this study are brown to grey porphyritic rocks. The average phenocryst content is approximately 50 vol. % ranging to as much as 60 vol. %. The dominant phenocryst assemblage consists of alkali feldspar, plagioclase, quartz, biotite and orthopyroxene. Phenocrysts of quartz, alkali feldspar and plagioclase define a bimodal distribution consisting of large phenocrysts and fine grained crystals constituting the groundmass. The accessory mineral assemblage consists of zircon, apatite, monazite, sphene and ilmenite. The alteration assemblage consists of chlorite, sericite, iron oxides and on rare occasion epidote and calcite.

Quartz constitutes up to 20 % of the phenocryst content. Crystals (0.5-7 mm) are euhedral to subhedral. Both monocrystaline and polycrystalline variants can be observed. Phenocrysts exhibit euhedral bipyramidal outlines that are broken by embayments filled with granular matrix material. These phenocrysts exhibit straight extinctions. Polycrystalline phenocrysts are subhedral to anhedral and exhibit characteristic undulose extinction. These crystals often contain cavities filled with matrix or finer grained quartz microltes.

Phenocrystic biotite constitutes up to 10 % of the crystal content. Phenocryst size ranges from 0.1 to 3 mm. Biotite is the main ferromagnesian mineral in the rock matrix. Biotite exists as reddish-brown to green tabular phenocrysts as well as microphenocrysts (0.1 – 0.5 mm), that occur as acicular crystals, interstitial laths to feldspars and quartz, and lamellar laths which overgrow the matrix and fill pre-existing fractures in larger alkali feldspar and quartz phenocrysts. Two generations of biotite are therefore evident, with the second generation being that which overgrows the matrix. The biotite which can be observed to overgrow the matrix is poikilitic and contains inclusions of matrix quartz or alkali feldspar. Some of these matrix grains (~5%) are partially altered and can be observed to be interleaved with chlorite. Tabular variants are often kinked and contain inclusions of zircon.

Phenocrystic alkali feldspar constitutes up to 40 % of the crystal content. Alkali feldspar forms euhedral to anhedral phenocrysts 1-8mm in size with a third of the phenocrysts being fragmented and fractured. Rounding of the corners of many phenocrysts is often apparent. Macro- to microperthitic alkali feldspar is common (fig.6 (a)), with up to half of the observed feldspar phenocrysts exhibiting plagioclase exsolutions in some thin sections. The extent of exsolution is highly variable, with some samples consisting of only perthitic feldspar as a feldspar phase and others containing no feldspar with perthitic exsolution. Perthitic exsolution patterns can be observed to be either well or poorly aligned. Embayed rims are found in fragmented individual crystals (1.5 – 2.0 mm). Phenocrysts can be observed to display both simple and multiple twinning. Inclusions of orthopyroxene, albite in K-feldspar, zircon and biotite are common.

Phenocrystic plagioclase constitutes up to 25 % of the crystal content. Plagioclase forms phenocrysts 1-5 mm in size as well as scarce microphenocrysts (0.5-1mm). It occurs as euhedral phenocrysts which display slight oscillatory zoning. Inclusions of orthopyroxene, monazite and zircon are common. Resorption of the phenocrysts is usually very slight or

absent, while fracturing is usually apparent. Sericite replacement is more prevalent in phenocrysts of plagioclase than alkali feldspar.

Phenocrystic orthopyroxene constitutes up to 5 % of the crystal content. The average phenocryst size ranges from 0.25 to 1 mm. The crystals are surrounded by reaction coronas of euhedral to subhedral biotite flakes. The phenocrysts are green to tan brown in colour and display a light green to light pink pleochroism. Most crystals are fractured with angular crystal edges. All orthopyroxene phenocrysts examined contain inclusions, mainly of apatite and ilmenite. Subhedral corroded phenocrysts (~0.4 mm) occuring as glomeroporphyritic clots with associated ilmenite, apatite and zircon are the most common form.

Polymineralic aggregates of quartz, biotite and opaque minerals (~2mm) are abundant in rocks with a microcrystalline matrix. Anhedral crystals illustrating a micrographic intergrowth of quartz and alkali feldspar can be observed. This feature is rare within the samples studied, only two sample exhibit this feature.

The major igneous oxide opaque assemblage is magnetite + ilmenite. These minerals occur as anhedral sub rounded crystals commonly occurring as individual crystals or as glomerocrysts of various Fe-Ti oxides with inclusions of apatite surrounded by coronas of biotite and chlorite. Ilmenite is partially to entirely altered to hematite. Sphene occurs as wedge shaped euhedral crystals. Epidote occurs as needle shaped inclusions in rare anhedral carbonate minerals or anhedral sub rounded crystals in quartz veins.

The groundmass is either microcrystalline (10-50μm) or cryptocrystalline (<10 μm). The matrix crystal size is highly variable between and within samples. Samples can consist of consistently sized matrix crystals of quartz and feldspar (albite) or contain domains of coarser crystals of both quartz and feldspar or quartz only. These domains vary in size (smallest being ~20μm in length) to a few centimetres across a thin section. The domains are most prominent in rocks with a cryptocrystalline groundmass. Figure's 6 (c), (d) and (f) illustrate the variation commonly exhibited in matrix crystal size within samples. The finer grained domains are visible in polished slabs as illustrated in 4 (c).

The rocks can be classified into two separate groups based on the consideration of the previously mentioned textures:

Group 1: Exhibit a predominantly microcrystalline matrix. They are characterised by quartz-biotite glomerocrysts; Fe-Ti oxide clots with coronas of biotite and chlorite.

Group 2: Exhibit a predominantly cryptocrystalline matrix; commonly shattered and broken phenocrysts (~ 90 % of the 50 to 60 vol. % phenocryst content); an absence of Fe-Ti oxide clots; an absence of biotite and quartz glomerocrysts.

The petrographic grouping will serve as a guideline for data presentation throughout the thesis.

The following samples can therefore be classed as group one: WP 11; WP 12B; A3; A5; WP 16; WP 18; WP 25A; WP 25B; WIG; WP 29; WP 30; WP 31A; WP 31B; MB 1; MB 2; MB

5; MB 6; MB 7A; MB 7B; MB 12; B 13B; B 15; B 16; B 17; B 18A; B 18B; B 19; B 20; B 22; MB 22; B 23; B 30.

The following samples can therefore be classed as group two: WP 12; A 1; A 7; A3/A5; WP 8; MB10; MB 11; B 13; B 26; MB 26; B 27; B 8; B 28.

The banded layers marking the contact with the porphyritic granite cropping out at location C (Fig. 3) are very fine grained and exhibit a matrix consisting of devitrified glass with microphenocrysts consisting of only quartz with small rounded opaque minerals situated in the matrix (Figure's 6 (g) and (h)). These rocks occur in narrow lenses along the contacts. The xenolith illustrated earlier (Fig. 4(b)) is found to consist of randomly oriented fine grained biotite porphyroblasts in a fine grained matrix (Fig. 6(i)).

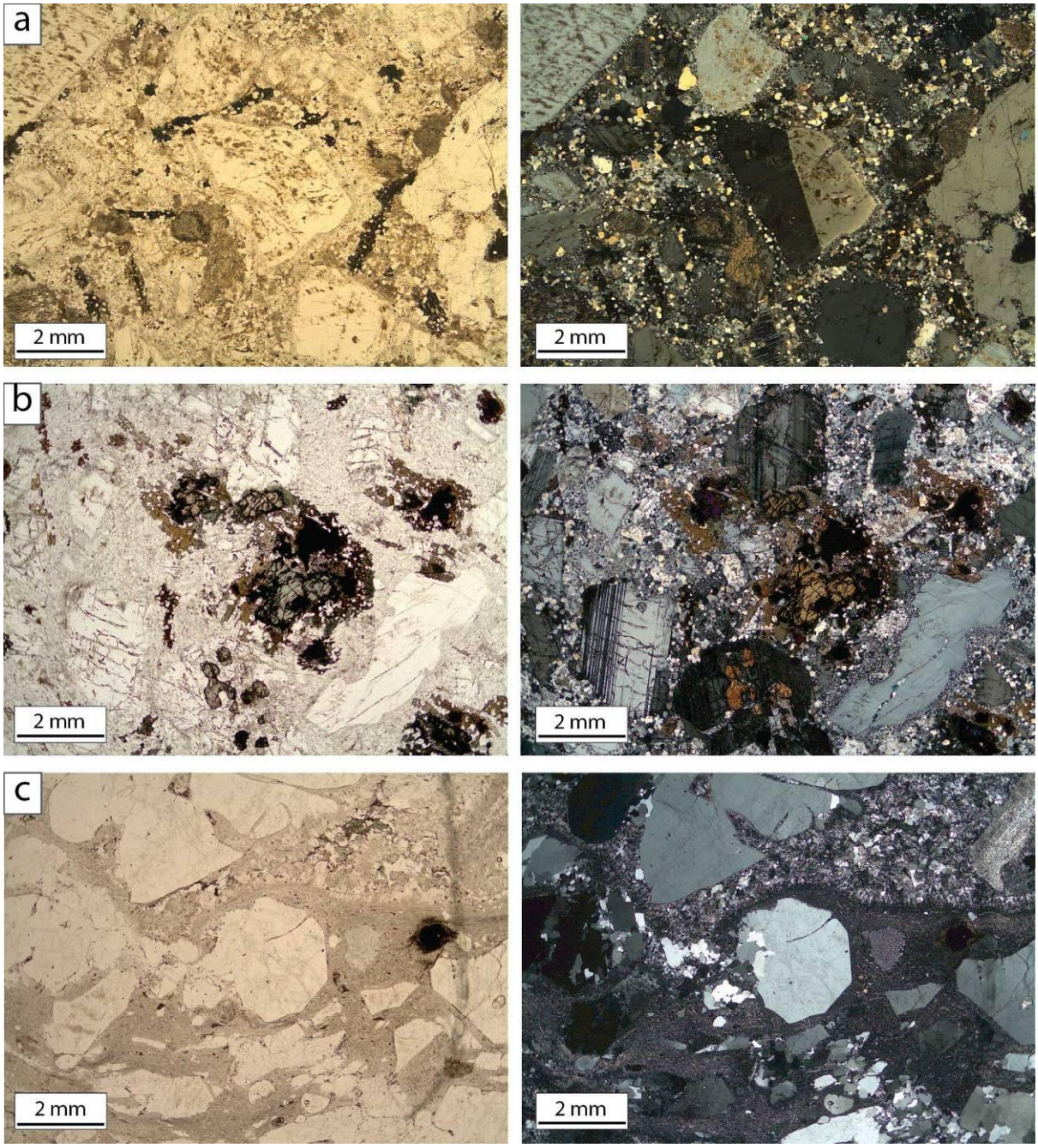

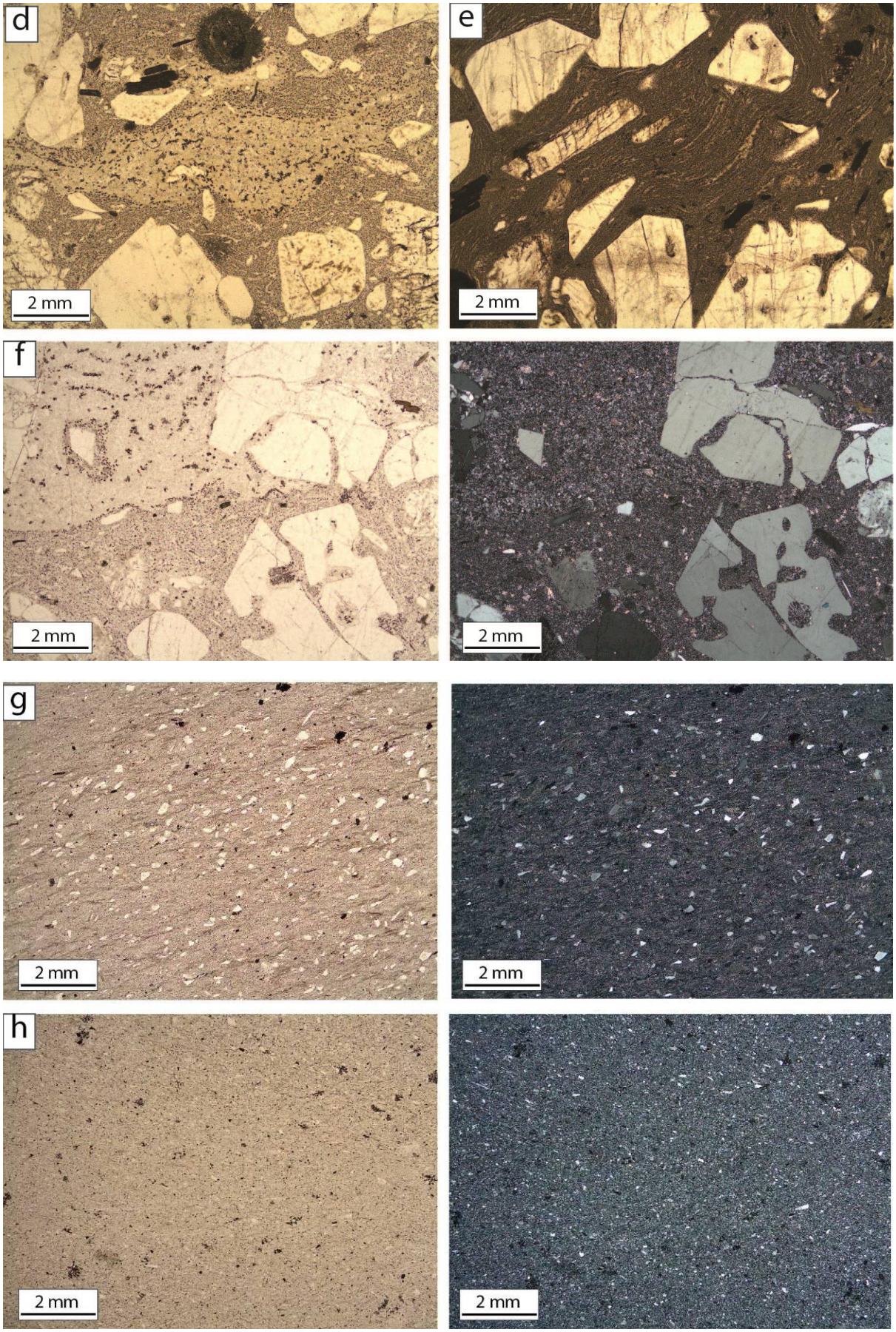

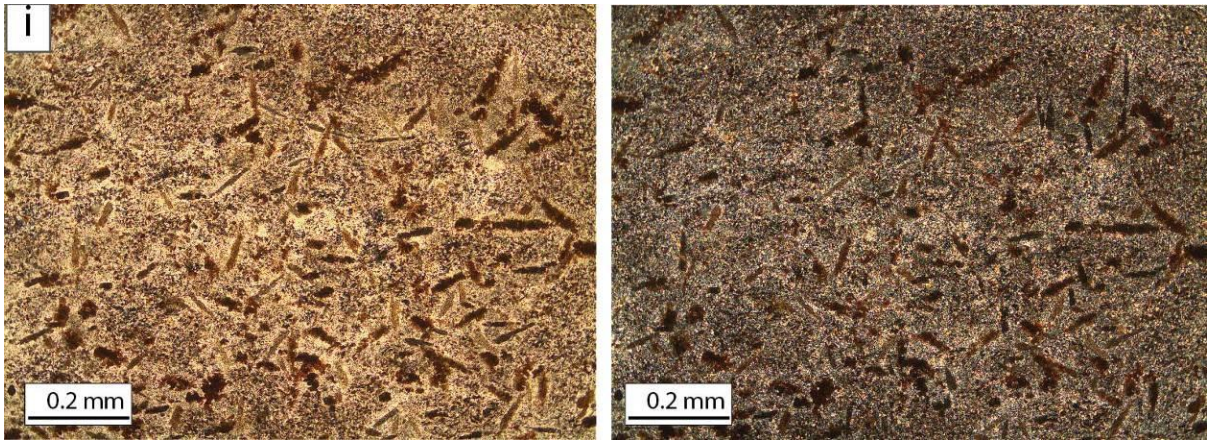

Figure 6. Photomicrographs of representative massive fine grained rocks (a-d), finer grained rocks at the contact with the granite (e-f) and a xenolith (i). (a) A perthitic feldspar grain can be observed in the centre exhibiting poorly aligned perthitic exsolutions surrounded by a finer grained groundmass of quartz, albite and acicular biotite. The surrounding phenocrysts are predominantly perthitic and display slight alteration to sericite as does the matrix feldspar imparting a brown colour to the rock in ppl. (b) Orthopyroxene can be seen to exist as anhedral corroded phenocrysts with inclusions of Fe-Ti oxides and coronas of biotite and chlorite or as anhedral inclusions of a much smaller size in surrounding fractured plagioclase and k-feldspar. (c) Two domains which exhibit differences in matrix crystal size with a well defined boundary can be observed. The finer grained matrix contains recrystallized quartz as well as fragmented quartz phenocrysts. (d) Photomicrograph illustrating a fine grained elongate domain surrounded by a finer grained matrix as well as phenocrysts and microphenocrysts of k-feldspar and quartz. (e) Phenocrysts of broken and embayed plagioclase and k-feldspar in a fine grained matrix. Light coloured elongate domains can be observed in the matrix displaying an alignment and curving around the phenocrysts. (f) Photomicrograph across two domains. The upper finer grained domain contains a larger abundance of matrix biotite and chlorite imparting a speckled appearance and resembles a flow texture mainly due to the alignment of matrix biotite and chlorite in near linear patterns. Phenocrystic quartz can be observed which can be seen to be broken and embayed. (g) Fragmented quartz crystals are embedded in a fine grained matrix, with darker bands within the matrix defining an aligned orientation, as well opaque minerals of variable size. (h) Fine grained quartz crystals within a finer grained matrix can be observed. The crystals of quartz are flatted in appearance and show slight alignment. (i) Xenolith consisting of randomly oriented fine grained biotite porphyroblasts in a fine grained matrix.

6 Whole Rock Chemistry

6.1 Major Element Chemistry

The major and trace element analyses of 13 representative samples of the fine grained rock are presented in Table 2. The table consists of seven samples of the first group (microcrystalline variant) and six samples of the second group (cryptocrystalline variant). A table of all the analyses, which consist of rocks of both groups is presented in the appendix. The rocks are SiO_2 rich, with silica content ranging between 66.6 and 75.76 wt. %. The TAS diagram in Figure 7 shows these rocks to be rhyolites. The rocks are relatively high in K_2O content (5.03-5.45 wt. %) and low in Na_2O content (2.25-2.81 wt. %) and display significant major element variability (Al_2O_3 = 11.9-14.9 wt. %, CaO = 0.58-1.87 wt. %, MgO = 0.14-0.51 wt. %, FeOt = 1.38-3.08 wt. %, Na_2O = 2.25-2.81 wt. %, TiO_2 = 0.16-0.45 wt. %). The fine grained rocks are slightly peraluminous with A/CNK (Al/0.5Ca+Na+K) ranging in value from 1.04 to 1.21. A/CNK and Si exhibit a negative correlation as a function of increasing maficity. Al, Ca, Na, P and Ti exhibit a positive correlation as a function of increasing maficity. The following elements exhibit a tight inter-element correlation when plotted

against maficity: Al (R^2=0.93), Ca (R^2=0.98), Na (R^2=0.75), P (R^2=0.96), Si (R^2=0.96), Ti (R^2=0.99). These values are applicable to the whole dataset. K displays a segmented trend, with a positive followed by a negative correlation as a function of increasing maficity. Figure 8 illustrates variation diagrams for Si, Al, Na, Ca, K, A/CNK, P and Ti plotted against maficity.

The textural subdivision of rock textures adopted in the petrography section has been applied in the description of samples on the bivariate diagrams displayed. Two separate populations which define separate ranges in maficity can be distinguished. The rocks of group two (cryptocrystalline variant) are more felsic than rocks of group one and define a lesser range in values of maficity (i. e. 0.0233 to 0.0264). Rocks of group one (microcrystalline variant) have values of maficity ranging between 0.0274-0.0569. These two populations also define two slightly different slopes resulting in a slightly "kinked" trend being displayed for Si, Al, Ca, Na when plotted against maficity.

6.2 Trace Element Chemistry

The trace element concentrations of these rocks are variable. The following ranges in ppm are exhibited for selected trace elements: Zr ranges between 26 to 345 ppm; Hf ranges between 1 and 8 ppm; Ce ranges between 5 and 140 ppm; La ranges between 2 and 66 ppm. Trace elements which occur as constituents in mineral phases, e.g. k-feldspar and zircon, display tight positive correlations as a function of increasing maficity. V, Sr, Ba, Hf, Zr are examples of such elements with trace element concentrations being plotted against maficity in Figure 9. The remaining trace elements display scattered trends when plotted against maficity. Table 3 contains trace element abundances for representative rock samples. Ba and Sr are large ion lithophile elements which are compatible within phases, principally plagioclase, that are reactants in melting reactions. Hf and Zr are high field strength elements concentrated within zircon. The tight positive correlations of these trace elements with maficity are similar to those of the Peninsula pluton and were interpreted to result from the co-entrainment of accessory minerals from the source (Villaros et al., 2009).

Rocks from group two (cryptocrystalline variant) contain lower concentrations of trace elements than their microcrystalline counterparts

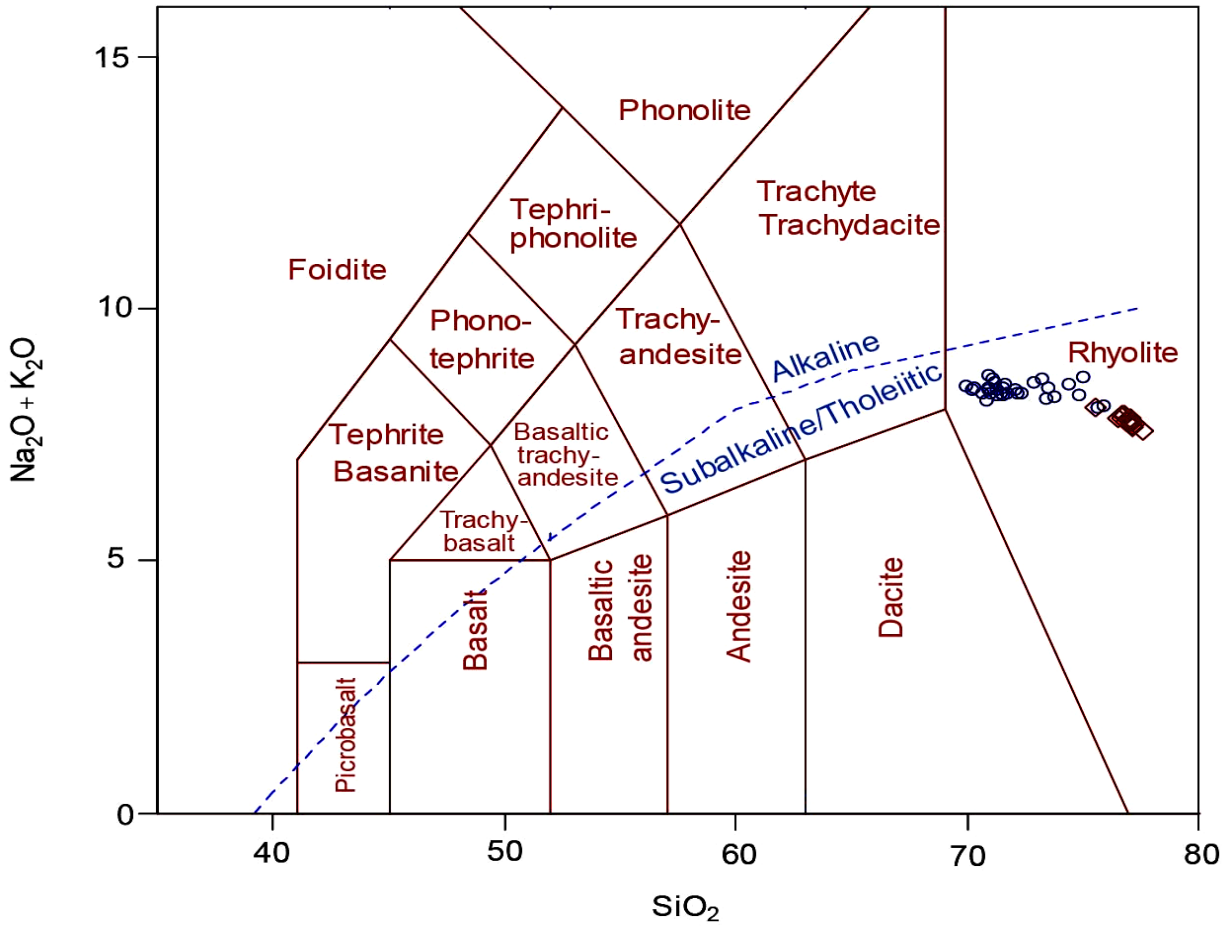

Figure 7. Total Alkali versus Silica diagram (after Le Bas et al., 1986; the alkali-sub alkali line boundary after Irvine and Baragar, 1971), blue circles represent rocks of group one, red diamonds represent rocks of group two.

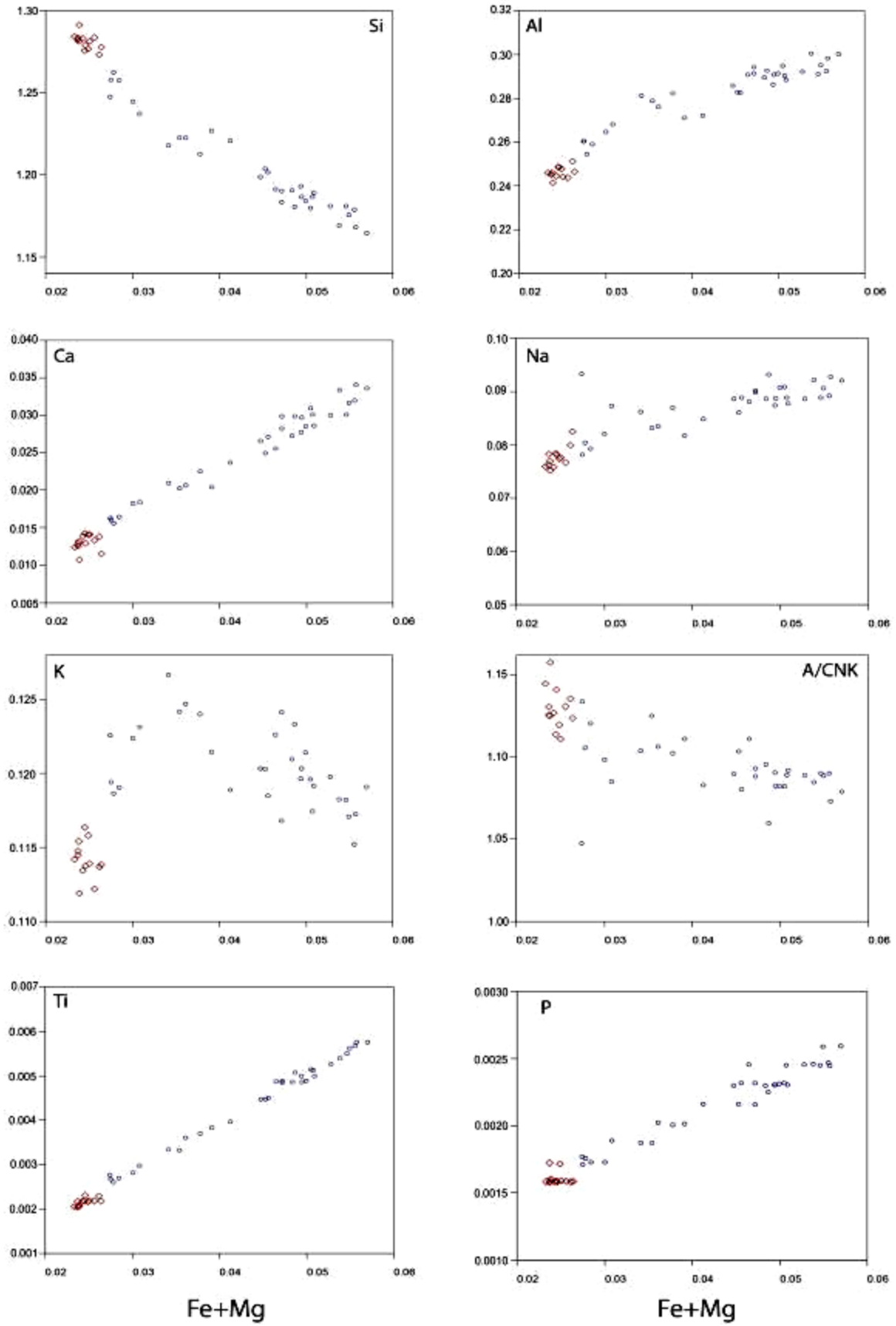

Figure 8: Variation diagrams of major elements plotted against maficity (atomic Fe + Mg). Red diamonds represent rocks of a cryptocrystalline variant (group 2) and blue circles represent rocks of a microcrystalline variant (group 1).

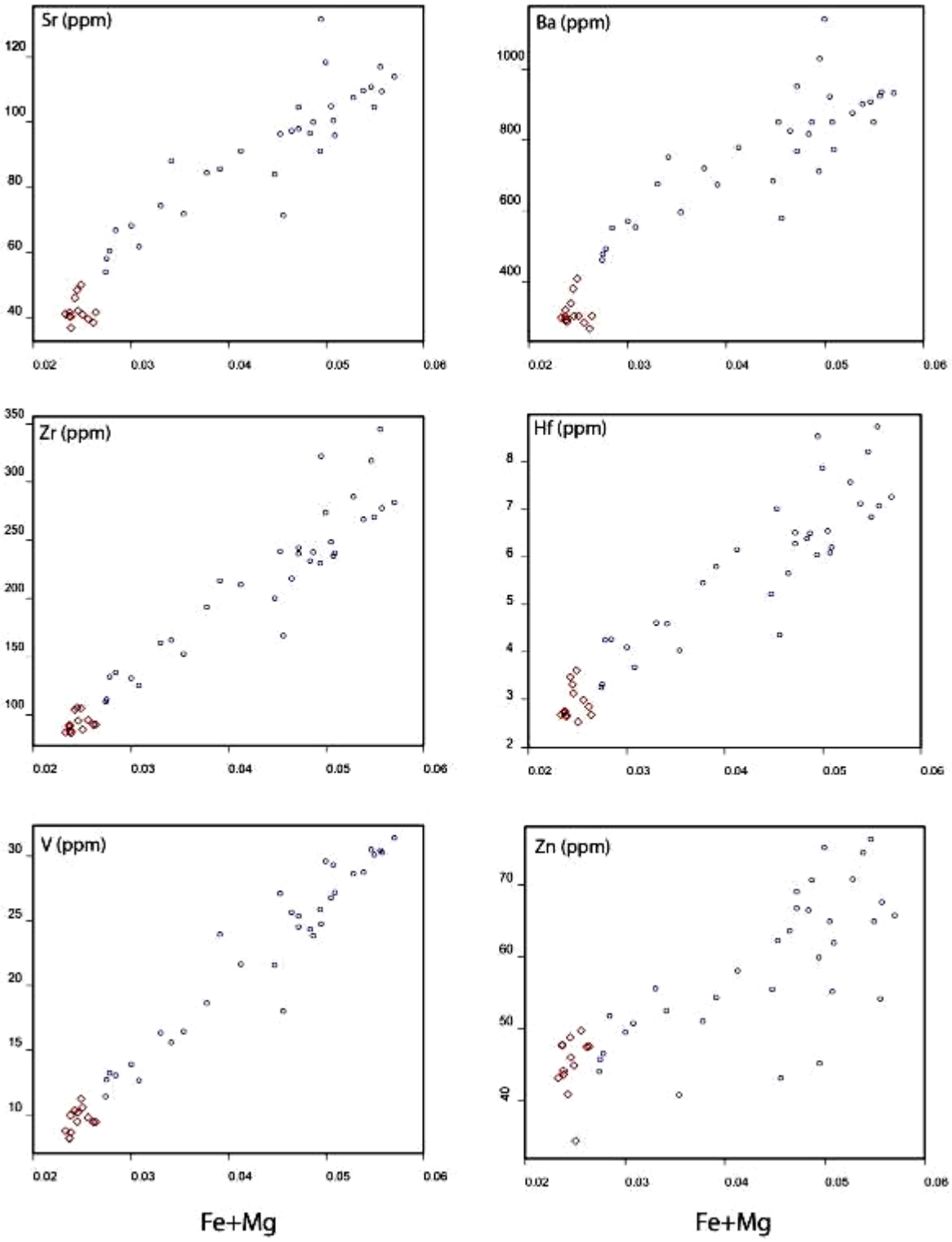

Figure 9: Variation diagrams for selected trace elements plotted against maficity. Red diamonds represent rocks of a cryptocrystalline variant (group 1) and blue circles represent rocks of a microcrystalline variant (group 2).

6.3 Rare Earth Element Chemistry

A Rock/Chondrites normalized REE element diagram (Boynton, 1984) of the rocks sampled is illustrated in Figure 10. The rhyolitic rocks exhibit an overall slightly steep LREE pattern with a more gently sloping HREE pattern and display a large negative Eu anomaly. Average Eu/Eu* = 0.52 for rocks of group one and 0.4 for rocks of group two (standard deviation= 0.03 and 0.05 respectively). The rocks of group two are depleted in light rare earth elements compared to the rocks of group one and exhibit a more negative Eu/Eu*. The ranges in HREE concentrations displayed by both groups of rocks overlap.

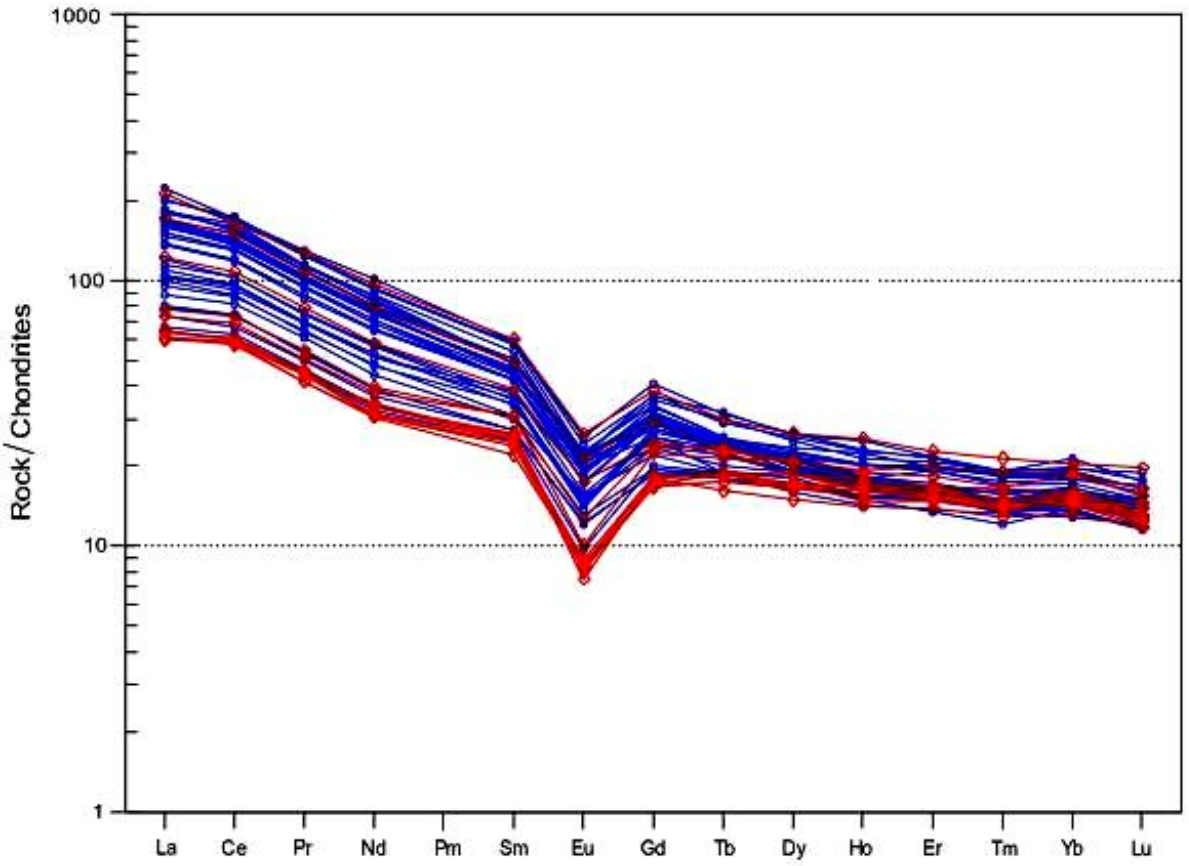

Figure 10: Chondrite-normalized REE pattern for rhyolitic rocks. Red diamonds represent group 2 rocks, blue circles represent group 1 rocks.

Table 2. Representative major and trace element compositions of rocks sampled.

Sample	A3	B13B	B18A	MB1	MB5	WP18	WP25B	A1	A3A5	A7	B9	MB10	MB11
Group	**1**									**2**			
wt%													
Al_2O_3	14.45	14.88	13.10	14.53	14.91	13.20	14.27	12.11	12.20	12.44	12.26	12.27	12.26
CaO	1.65	1.87	0.89	1.64	1.82	1.00	1.52	0.77	0.76	0.78	0.69	0.71	0.68
FeO	2.77	3.02	1.61	2.89	2.90	1.75	2.71	1.47	1.46	1.49	1.42	1.42	1.38
K_2O	5.40	5.40	5.55	5.50	5.42	5.64	5.51	5.22	5.23	5.37	5.29	5.31	5.26
MgO	0.44	0.50	0.19	0.45	0.48	0.20	0.42	0.16	0.14	0.15	0.14	0.14	0.14
MnO	0.04	0.04	0.03	0.05	0.04	0.03	0.04	0.02	0.03	0.03	0.02	0.03	0.02
Na_2O	2.69	2.81	2.39	2.68	2.78	2.49	2.65	2.34	2.30	2.36	2.38	2.32	2.30
P_2O_5	0.17	0.17	0.12	0.17	0.17	0.12	0.16	0.11	0.11	0.12	0.12	0.11	0.11
SiO_2	69.62	68.64	74.58	69.18	68.36	73.20	70.09	74.93	75.50	75.53	75.63	75.76	75.49
TiO_2	0.40	0.45	0.21	0.41	0.42	0.22	0.39	0.17	0.17	0.17	0.17	0.16	0.16
LOI	0.53	0.48	0.67	0.69	0.69	0.45	0.56	0.59	0.60	0.44	0.61	0.76	0.92
Total	98.16	98.26	99.34	98.19	97.99	98.30	98.32	97.88	98.50	98.88	98.73	98.99	98.73
A/CNK	1.09	1.07	1.13	1.09	1.08	1.10	1.09	1.11	1.13	1.12	1.13	1.13	1.14
ppm													
V	29.32	30.31	12.72	28.64	28.78	13.87	25.89	10.52	10.32	11.21	8.18	8.14	8.75
Cr	12.11	13.01	8.26	19.44	10.14	13.78	24.53	9.75	< 8	8.88	9.94	14.19	9.48
Ni	7.70	7.10	5.74	7.66	6.40	5.76	9.24	5.65	4.04	4.49	5.98	5.15	5.10
Cu	18.05	10.39	14.75	7.84	12.36	13.68	23.73	13.96	16.36	23.88	13.36	7.29	8.35
Zn	55.17	67.62	45.74	70.75	74.48	49.48	59.86	34.45	40.92	44.88	47.80	47.70	43.12
Rb	203.14	200.69	243.25	202.02	201.91	279.94	204.32	216.44	285.46	291.78	272.80	241.14	251.86
Sr	100.42	109.44	58.29	107.70	109.75	68.30	91.04	41.05	46.25	50.36	40.75	41.86	41.26
Y	33.87	33.61	30.19	41.49	35.31	34.76	32.99	28.04	34.90	35.40	32.60	32.19	30.04
Zr	237	277.37	113.42	287.20	268.24	131.84	230.42	87.34	104.58	105.69	90.04	91.31	85.24
Mo	1.92	2.51	1.13	1.85	2.01	0.63	1.86	2.09	2.42	2.68	0.84	0.73	2.00
Cs	8.52	9.12	10.53	9.17	8.79	12.97	8.15	7.90	12.15	11.45	12.01	10.21	9.88
Ba	852.33	934.90	478.07	876.63	901.27	571.51	711.79	302.85	339.06	408.18	301.27	320.07	297.66

Table 2. (continued)

Sample	A3	B13B	B18A	MB1	MB5	WP18	WP25B	A1	A3A5	A7	B9	MB10	MB11
Group	**1**									**2**			
ppm													
Pr	12.62	14.05	6.48	13.67	13.66	8.56	11.57	5.07	6.19	6.62	5.55	5.38	5.35
Nd	45.38	51.58	23.31	52.74	50.23	30.74	42.66	18.31	22.65	23.78	19.90	20.47	18.39
Sm	8.80	9.38	5.30	10.40	9.53	7.46	8.15	4.29	5.98	6.04	4.96	4.90	4.78
Eu	1.61	1.62	0.90	1.55	1.59	1.15	1.37	0.62	0.74	0.92	0.59	0.65	0.61
Gd	8.02	7.67	4.82	8.27	7.82	6.67	7.73	4.64	5.80	6.11	4.47	4.74	4.31
Tb	1.17	1.14	0.86	1.20	1.18	1.09	1.15	0.76	1.02	1.11	0.88	0.89	0.82
Dy	6.45	6.72	5.36	7.57	6.99	6.77	6.43	4.79	6.73	6.72	5.44	5.53	5.25
Ho	1.24	1.27	1.09	1.61	1.27	1.30	1.14	1.02	1.35	1.37	1.19	1.19	1.11
Er	3.31	3.50	3.12	4.13	3.49	4.03	3.32	2.93	3.82	4.22	3.29	3.43	3.30
Tm	0.48	0.45	0.43	0.59	0.48	0.55	0.45	0.41	0.54	0.61	0.46	0.45	0.45
Yb	3.18	2.96	2.84	3.75	3.41	3.59	3.09	2.74	3.87	3.96	3.08	3.17	2.98
Lu	0.44	0.44	0.38	0.51	0.47	0.48	0.42	0.38	0.50	0.53	0.44	0.42	0.40
Hf	6.10	7.07	3.32	7.58	7.12	4.10	6.04	2.53	3.48	3.62	2.72	2.76	2.68
Pb	33.80	37.52	36.40	37.04	39.88	46.30	35.92	29.37	39.29	42.08	32.78	35.41	32.57
Th	18.87	20.91	12.07	22.37	21.06	16.73	17.96	10.33	13.51	14.18	11.66	11.74	11.21
Ce	115.20	131.58	60.36	124.28	125.70	76.30	105.81	45.94	55.85	59.34	49.02	48.22	46.60
La	50.77	56.50	25.05	57.12	56.43	32.24	46.49	18.75	22.71	24.04	19.81	20.14	18.81
U	4.28	4.96	4.50	5.32	5.13	4.56	4.77	5.93	8.28	8.62	4.71	4.49	6.93

7 Mineral Chemistry

Tables are presented which contain averaged compositional values for selected mineral phases. Complete tables with standard deviations calculated for these averaged values can be found in the appendix.

7.1 Feldspar

A total of 35 feldspar grains from 7 samples were studied (Table 3). Structural formulae were calculated on the basis of 8 oxygens and 5 cations. A table of thirteen representative analyses is presented below. The table consists of averaged values for compositionally homogenous crystals as well as a crystal with associated perthitic exsolution with compositions for both the host crystal as well as the exsolution being presented in Table 3 below. Anorthite, orthoclase and albite present the following ranges, $An_{0.75\text{-}8.1}$ and $An_{26\text{-}35.5}$, $Or_{0.66\text{-}25}$ and $Or_{63\text{-}77.3}$ and $Ab_{21.37\text{-}97.84}$. The foregoing represents ranges for end member compositions exhibited for phenocrysts within each individual sample. The perthitic exsolutions occur as a series of poorly to well aligned rounded blebs of albite ($Ab_{90\text{-}98}$) in a host grain of orthoclase ($Or_{66\text{-}77}$). The exsolutions as well as inclusions of albite in their host grain of orthoclase are not always texturally discernible.

7.2 Biotite

A total of 12 biotite grains from 6 selected samples were studied (Table 4). Structural formulae were calculated on the basis of 22 oxygens and 8 cations. The biotite phenocrysts contain up to 4.7 wt. % TiO_2 and 28.38 wt. % FeO^T. Structural formulae show that Si and Al cation p.f.u. generally fill the tetrahedral sites. The biotites show a range in compositions with SiO_2 = 34.85–36.73 wt.%, FeO^T =24.33–28.38 wt.%, Al_2O_3 = 14.15–16.30 wt.%, K_2O = 8.67–9.49 wt.%, TiO_2 = 1.99–4.77 wt.%. Mg# (Mg/ (Mg +Fe)) ranges between 0.22 and 0.31. In the structural formulae, the 12-fold co-ordination site totals range between 1.84 and 1.95. The octahedral site totals show similar variation with values ranging between 5.52 to 5.83 cations p.f.u. Biotite which forms tabular phenocrysts (0.6-1.5mm) in group two rocks exhibits high values of K (values > 1.8 apfu) and Ti (values > 0.43 apfu). Biotite's of the acicular or anhedral variety (~200-600µm) exhibit with lower values of K (values < 0.43 apfu) and Ti (values < 0.43 apfu).

7.3 Orthopyroxene

A total of 11 pyroxenes were selected from 4 samples (Table 5). Structural formulae were calculated on the basis of 6 oxygens and 4 cations. The orthopyroxene can be classified as ferrohypersthene $Fs_{50\text{-}70}$ based on Poldervaart's nomenclature for the orthopyroxene diadochic series. Orthopyroxene is commonly denoted by its overall fraction of ferrosilite (Fs = Fe^T/Ca+Mg+Fe^T), enstatite (En = Mg/Ca+Mg+Fe^T) and wollastinite (Wo = Ca/Ca+Mg+Fe^T). The samples studied show the following range in terms of this denotation: $Fs_{64\text{-}74}$, $En_{25\text{-}34}$ and $Wo_{0.1\text{-}1.09}$. Al content ranges between 1.05 and 2.38 wt. %. Ca content ranges from 0.06 to 0.49 wt. %. Na is present in six of the analyses and ranges between 0.02 and 0.63 wt. %. Rare inclusions of orthopyroxene within orthopyroxene can be observed in two of the samples. The included orthopyroxene differs from the other pyroxene crystals

including its host in that it contains K (0.06 wt. %), lesser Ti and the absence of tetrahedral Al with higher octahedral aluminium. The aluminium and calcium contents of the inclusion are 1.6 and 0.25 wt% respectively and are much lower than the host pyroxene crystal whose aluminium and calcium contents are 1.74 and 0.36 wt% respectively.

Table 3. Averaged (σ<1) compositions of selected feldspar phenocryst crystals. Analyses of exsolutions are also provided as well analyses of the host grain.

Sample	A1				A3A5			A3				WP 31	
Group	**2**							**1**					
Feldspar Grain	1.00	2.00	3.00	3-Exsol	1.00	2.00	4.00	1.00	2.00	3.00	4.00	1.00	2.00
SiO_2	59.21	65.49	65.33	68.41	65.24	65.13	58.53	59.65	58.26	58.44	58.69	64.75	67.60
Al_2O_3	25.63	18.86	18.78	19.73	19.06	19.09	25.51	25.86	25.72	25.51	25.52	19.08	19.81
FeO	0.10	0.05	0.06	0.10	0.07	0.04	0.11	0.14	0.12	0.20	0.10	0.07	0.05
CaO	7.30	0.32	0.29	0.30	0.37	0.36	7.27	7.28	7.55	7.24	7.25	0.37	0.29
Na_2O	7.39	3.40	2.42	10.86	3.27	3.38	7.42	7.20	7.13	7.22	7.03	3.70	10.95
K_2O	0.85	11.98	13.29	0.18	12.04	11.88	0.78	0.95	0.79	0.89	0.94	11.86	0.33
BaO	0.05	0.31	0.30	0.08	0.65	0.57	0.05	0.09	0.03	0.03	0.04	0.28	0.02
SrO	0.10	0.09	0.12	0.03	0.01	0.05	0.02	0.10	0.03	0.12	0.06	0.06	0.04
Total	100.63	100.51	100.59	99.70	100.70	100.51	99.70	101.26	99.62	99.66	99.63	100.16	99.08
Formula based on eight O atoms													
Si	2.64	2.98	2.99	2.99	2.97	2.97	2.63	2.64	2.62	2.63	2.64	2.96	2.98
Al	1.35	1.01	1.01	1.02	1.02	1.03	1.35	1.35	1.37	1.36	1.35	1.03	1.03
Fe	0.00	0.00	0.00	0.00	0.00	0.00	0.00	0.00	0.00	0.00	0.00	0.00	0.00
Ca	0.35	0.02	0.01	0.01	0.02	0.02	0.35	0.35	0.36	0.35	0.35	0.02	0.01
Na	0.64	0.30	0.21	0.92	0.29	0.30	0.65	0.62	0.62	0.63	0.61	0.33	0.94
K	0.05	0.70	0.78	0.01	0.70	0.69	0.04	0.05	0.05	0.05	0.05	0.69	0.02
Ba	0.00	0.01	0.01	0.00	0.01	0.01	0.00	0.00	0.00	0.00	0.00	0.00	0.00
Sr	0.00	0.00	0.00	0.00	0.00	0.00	0.00	0.00	0.00	0.00	0.00	0.00	0.00
Total	5.03	5.02	5.01	4.96	5.02	5.02	5.04	5.01	5.02	5.02	5.01	5.03	4.98
An	33.67	3.79	1.41	1.51	1.81	1.74	34.57	33.94	35.30	33.89	34.37	1.76	1.42
Ab	61.65	72.12	21.37	97.84	28.69	29.64	60.98	60.80	60.31	61.16	60.30	31.60	96.67
Or	4.68	24.09	77.22	0.66	69.50	68.61	4.46	5.25	4.39	4.95	5.33	66.63	1.90

Table 4. Averaged (σ<1) compositions of selected biotite crystals.

Sample	MB7		WP 11		A3A5	WP 31			A1		A3	
Group	**1**		**1**		**2**	**1**			**2**		**1**	
Biotite Grain	1	2	1	2	1	1	2	3	1	2	1	2
SiO_2	35.35	36.73	36.04	35.94	35.20	34.93	35.12	35.61	34.90	35.42	36.22	34.85
TiO_2	3.81	3.79	3.27	3.90	4.77	2.20	3.20	1.99	4.53	4.12	4.12	1.59
Al_2O_3	14.40	14.65	15.92	15.02	15.76	15.12	15.89	15.39	15.95	16.25	14.15	16.30
FeO	28.38	25.42	26.24	26.64	24.33	27.83	27.69	27.38	26.77	25.14	25.85	28.12
MnO	0.16	0.25	0.28	0.25	0.32	-	0.26	0.26	0.38	0.28	0.16	0.26
MgO	4.82	6.30	4.56	4.73	5.60	6.34	4.56	6.06	4.15	5.43	6.52	5.06
CaO	0.07	0.05	0.05	0.05	0.04	-	0.04	0.06	0.06	-	0.04	-
Na_2O	0.23	0.12	0.20	0.20	0.27	0.28	0.30	0.22	0.20	0.21	0.19	0.09
K_2O	8.67	9.25	9.13	9.08	9.09	8.90	8.87	8.91	9.08	9.49	8.93	8.75
Total	95.90	96.55	95.70	95.81	95.38	95.59	95.94	95.88	96.02	96.33	96.16	95.02
Mg#	0.23	0.31	0.24	0.24	0.29	0.29	0.23	0.28	0.22	0.28	0.31	0.24
Formula based on 22 O atoms												
Si	5.60	5.69	5.66	5.65	5.51	5.55	5.55	5.62	5.49	5.51	5.65	5.56
Al (iv)	2.40	2.31	2.34	2.35	2.49	2.45	2.45	2.38	2.51	2.49	2.35	2.44
Total (T)	8	8	8	8	8	8	8	8	8	8	8	8
Al (vi)	0.29	0.37	0.60	0.44	0.42	0.38	0.50	0.48	0.45	0.49	0.25	0.63
Ti	0.45	0.44	0.39	0.46	0.56	0.26	0.38	0.24	0.54	0.48	0.48	0.19
Fe	3.76	3.29	3.44	3.50	3.19	3.70	3.66	3.61	3.52	3.27	3.37	3.75
Mn	0.02	0.03	0.04	0.03	0.04	0.00	0.03	0.03	0.05	0.04	0.02	0.04
Mg	1.14	1.46	1.07	1.11	1.31	1.50	1.07	1.42	0.97	1.26	1.52	1.20
Total (M)	5.67	5.59	5.53	5.54	5.52	5.83	5.65	5.78	5.54	5.54	5.64	5.81
Ca	0.01	0.01	0.01	0.01	0.01	0.00	0.01	0.01	0.01	0.00	0.01	0.00
Na	0.07	0.04	0.06	0.06	0.08	0.09	0.09	0.07	0.06	0.06	0.06	0.03
K	1.75	1.83	1.83	1.82	1.81	1.80	1.79	1.79	1.82	1.88	1.78	1.78
Total(T)	1.84	1.87	1.90	1.89	1.90	1.89	1.89	1.87	1.89	1.95	1.84	1.81

Table 5. Averaged (σ<1) compositions of selected pyroxene crystals. A rim and core analyses is also provided.

Sample	B19			MB 7		MB1					A3	
Group	**1**											
Pyroxene Grain	1	2	3	1-Rim	1-Core	1	2	3	4	5	1	2
SiO_2	47.6	46.8	47.6	47.8	50.2	48.6	48.3	48.5	48.2	47.2	47.9	48.4
TiO_2	0.20	0.23	0.23	0.17	0.10	0.17	0.20	0.18	0.20	0.19	-	0.24
Al_2O_3	1.79	1.97	1.74	1.74	1.60	1.85	1.79	1.72	1.85	2.38	1.87	1.82
Cr_2O_3	-	-	-	-	-	-	-	-	-	-	-	-
FeO	37.7	39.5	37.4	37.8	35.6	38.4	38.9	38.2	39.2	41.2	37.4	37.2
MnO	0.72	0.93	0.70	0.68	0.95	0.72	0.74	0.68	0.75	0.98	0.69	0.74
MgO	10.1	8.7	10.2	10.6	10.7	10.5	10.1	10.4	9.7	8.0	10.7	10.8
CaO	0.37	0.21	0.39	0.36	0.25	0.33	0.34	0.39	0.31	0.20	0.31	0.49
Na_2O	-	0.36	-	-	0.20	-	-	-	-	0.02	0.11	-
K_2O	-	-	-	-	0.06	-	-	-	-	-	-	-
Total	98.50	98.59	98.33	99.14	99.70	100.61	100.32	100.08	100.16	100.20	99.02	99.66
Mg#	0.32	0.28	0.33	0.33	0.35	0.33	0.32	0.33	0.31	0.26	0.34	0.34
Formula based on six O atoms												
Si	1.95	1.93	1.96	1.94	2.02	1.95	1.95	1.96	1.95	1.94	1.95	1.95
Al	0.05	0.07	0.04	0.06	0.00	0.05	0.05	0.04	0.05	0.06	0.05	0.05
Total T	2.00	2.00	2.00	2.00	2.02	2.00	2.00	2.00	2.00	2.00	2.00	2.00
Ti	0.01	0.01	0.01	0.01	0.00	0.01	0.01	0.01	0.01	0.01	0.00	0.01
Al	0.04	0.03	0.04	0.03	0.08	0.04	0.04	0.04	0.04	0.05	0.04	0.04
Cr	0.00	0.00	0.00	0.00	0.00	0.00	0.00	0.00	0.00	0.00	0.00	0.00
Fe^{3+}	0.00	0.06	0.00	0.02	0.00	0.00	0.00	0.00	0.00	0.00	0.03	0.00
Fe^{2+}	0.65	0.65	0.64	0.63	0.59	0.64	0.65	0.64	0.66	0.70	0.62	0.63
Mg	0.31	0.26	0.31	0.32	0.31	0.31	0.30	0.31	0.29	0.24	0.32	0.32
Total M1(VI)	0.99	0.99	0.99	0.99	0.98	0.99	0.99	0.99	0.99	0.99	1.00	0.99
Fe^{2+}	0.65	0.66	0.64	0.64	0.61	0.65	0.66	0.65	0.67	0.71	0.63	0.63
Mn	0.03	0.03	0.02	0.02	0.03	0.02	0.03	0.02	0.03	0.03	0.02	0.03
Mg	0.31	0.27	0.31	0.32	0.33	0.32	0.30	0.31	0.29	0.25	0.33	0.32

Table 5 cont.

Ca	0.02	0.01	0.02	0.02	0.01	0.01	0.01	0.02	0.01	0.01	0.01	0.02
Na	0.00	0.03	0.00	0.00	0.02	0.00	0.00	0.00	0.00	0.00	0.01	0.00
Total M2(VI)	1.00	1.00	1.00	1.00	1.00	1.00	1.00	1.00	1.00	1.00	1.00	1.00
Wo	0.8	0.5	0.9	0.8	0.6	0.7	0.8	0.9	0.7	0.5	0.7	1.1
En	32.1	28.0	32.5	33.1	34.7	32.6	31.3	32.4	30.3	25.5	33.6	33.7
Fs	67.1	71.5	66.6	66.0	64.7	66.7	67.9	66.7	69.0	74.0	65.7	65.2

7.4 Modelling of Mineral Stability

P-T pseudosections are phase stability diagrams calculated for particular rock compositions. They provide a means of predicting the stable assemblage of phases within P-T space, and can be used to obtain estimates of the composition and the relative abundance of the minerals in each assemblage field. Measured mineral compositions can be compared to the predicted compositions in order to obtain estimates of the P-T conditions under which the assemblage formed. These techniques were first developed for use in subsolidus metamorphic studies and subsequently, with the development of a model to predict the behaviour of melt (Holland and Powell, 2001) has been applied to studies of migmatites. Villaros et al (2009b) used a pseudosection modelling approach to provide useful constraints on the conditions of crystallization of garnet from the peninsular pluton. Consequently, a similar approach is attempted here to constrain the P-T conditions of crystallization of the phenocrysts. The assemblages that would form in a magma represented by sample A3 (SiO_2= 69.62, Al_2O_3= 14.45, FeO = 2.77, MgO = 0.44, CaO = 1.65, Na_2O = 2.69, K_2O = 5.40, H_2O = 3.00, values represent major oxide weight percent) are predicted from a pseudosection calculated using PerpleX (Conolly 1990; Conolly and Petrini 2002). This sample was selected as it contained abundant orthopyroxene phenocrysts. Granite magmas lose water on crystallization, so the magma water content is not available from the whole rock analysis. Additionally, granite magmas may mobilise out of the source with entrained peritectic phases, adding to the uncertainty surrounding magma water content, even if the water content of the melt was known. The K_2O-rich I-type character of the rocks is consistent with their formation by biotite dominated melting. Incongruent melting of biotite at mid- to lower-crustal P-T conditions buffers the melt water content to approximately 3.5 wt% water (Clemens and Watkins, 2001). Consequently a value of 3 wt% water was chosen for the modelling, thereby allowing for the possibility of some anhydrous crystal content in the magma on leaving the source. This value seems reasonable as it results in fluid-saturation at a temperature close to the wet granite solidus (Fig. 11). Thus, the solidus predicted by the modelling is the lowest temperature solidus possible over the entire pressure range.

The pseudosections were constructed using the program Perplex (Conolly, 1990; Conolly and Petrini, 2002; Conolly, 2005). Solid solution models used to establish the pseudosection are: TiBio (WPH) (White et al., 2007), Pheng (HP), Sp (HP), hCrd, Opx(HP) (Holland and Powell, 1996), melt (HP) (Holland and Powell, 2001; White et al, 2001), Gt (WPH) (Bertelloni and Ritsema, 2008), Pl (h) (Newton et al, 1980) and Kf (Waldbaum and Thompson, 1969) (details in solut09.dat; database: hp04ver.dat).

Pseudosections were constructed for a temperature-pressure range of 600 to 1000 °C and 1 to 10 kilobars (Fig. 11, 13,14 and 15). Figure 12 is constructed for a temperature range of 600 to 900 °C and a pressure range of 1 and 4.6 kilobars. The foregoing figure is constructed to provide clarity of P-T stability fields within the P-T range specified. The heavy dashed line in the pseudosections presented represents the wet solidus. Mineral abbreviations follow those of Kretz (1983).In these pseudosections, plagioclase is stable mineral phase over the entire P-T range of 600 to 1000°C and 1 to 10 kbar. Biotite is lost beginning at temperatures between 750 to 790°C. K feldspar is lost beginning at temperatures between 800 to 710°C.Garnet is

absent below pressures of 2800 kbar. Orthopyroxene is stable over the modelled P-T range of 740 to 860°C and pressures below 6850 kbar.

Isopleths reflecting the volume percent of orthopyroxene, aluminium content in weight percent and Mg# (i.e. Mg# = Mg/ (Mg + Fe)) are illustrated in Figures 13, 14and 15 respectively. The modelling predicts a decrease in aluminium content and Mg# in orthopyroxene with decreasing pressure within the fields were orthopyroxene is stable and an increase in volume percent with decreasing pressure. Orthopyroxene is found to constitute 4 % of the crystal content for sample A3. The Al_2O_3 content of two orthopyroxene grains from sample A3 (Table 6) is 1.87 and 1.82 and Mg# is 0.34 for both grains. A comparison of Mg # between the orthopyroxene grains (Mg# = 0.26 -0.35) studied and the predicted by the model (Mg# = 0.26 – 0.36) indicates that the phenocrysts studied represent phenocrysts formed throughout the P-T stability field. The P-T pseudosections predict orthopyroxene contents (Fig. 13) lower than those for sample A3. Al_2O_3 contents (Fig. 14) are significantly higher (5.0 to 6.1 wt%) than those exhibited by the pyroxene grains for sample A3. The Mg# for sample A3 (Mg# = 0.34) falls within the range predicted by the pseudosection.

	SiO_2	Al_2O_3	FeO	MgO	CaO	Na_2O	K_2O	H_2O
A3	69.61	14.45	2.77	0.44	1.65	2.69	5.40	3.00

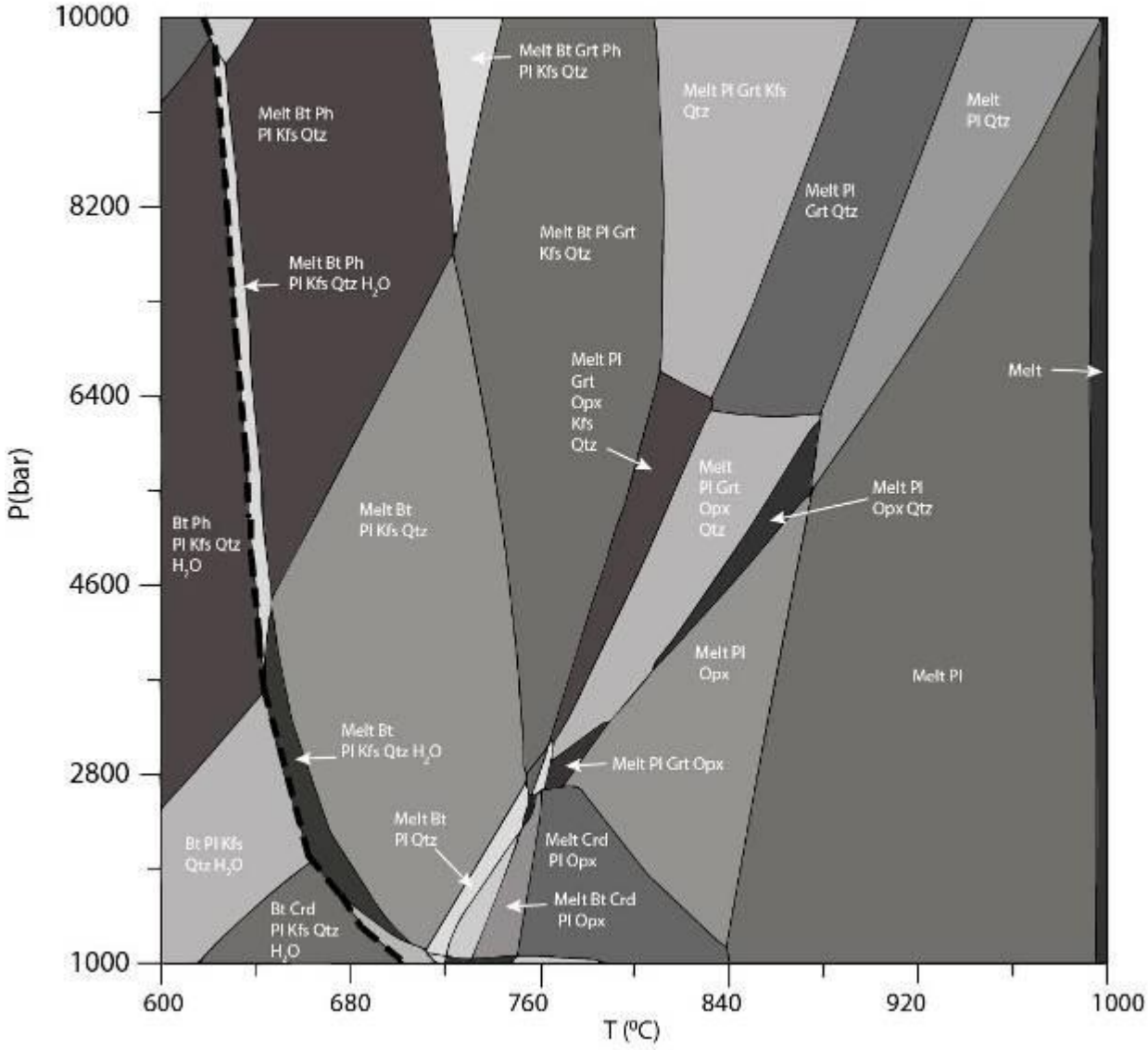

Figure 11.Partial P-T phase diagram for the rhyolitic rocks, as exemplified by sample A3, in the system NCKFMASH, using Perplex (Conolly 2009). The heavy dashed line represents the wet solidus. Pseudosection constructed for pressures ranging from 1 to 10 kilobars and temperatures ranging from 600 to 1000 °C. Abbreviations: Bt = biotite, Grt = garnet, Kfs = K feldspar, Pl = plagioclase, Opx = orthopyroxene, Crd = cordierite, Qtz = quartz, Ph = phengite (after Kretz, 1983).

	SiO_2	Al_2O_3	FeO	MgO	CaO	Na_2O	K_2O	H_2O
A3	69.61	14.45	2.77	0.44	1.65	2.69	5.40	3.00

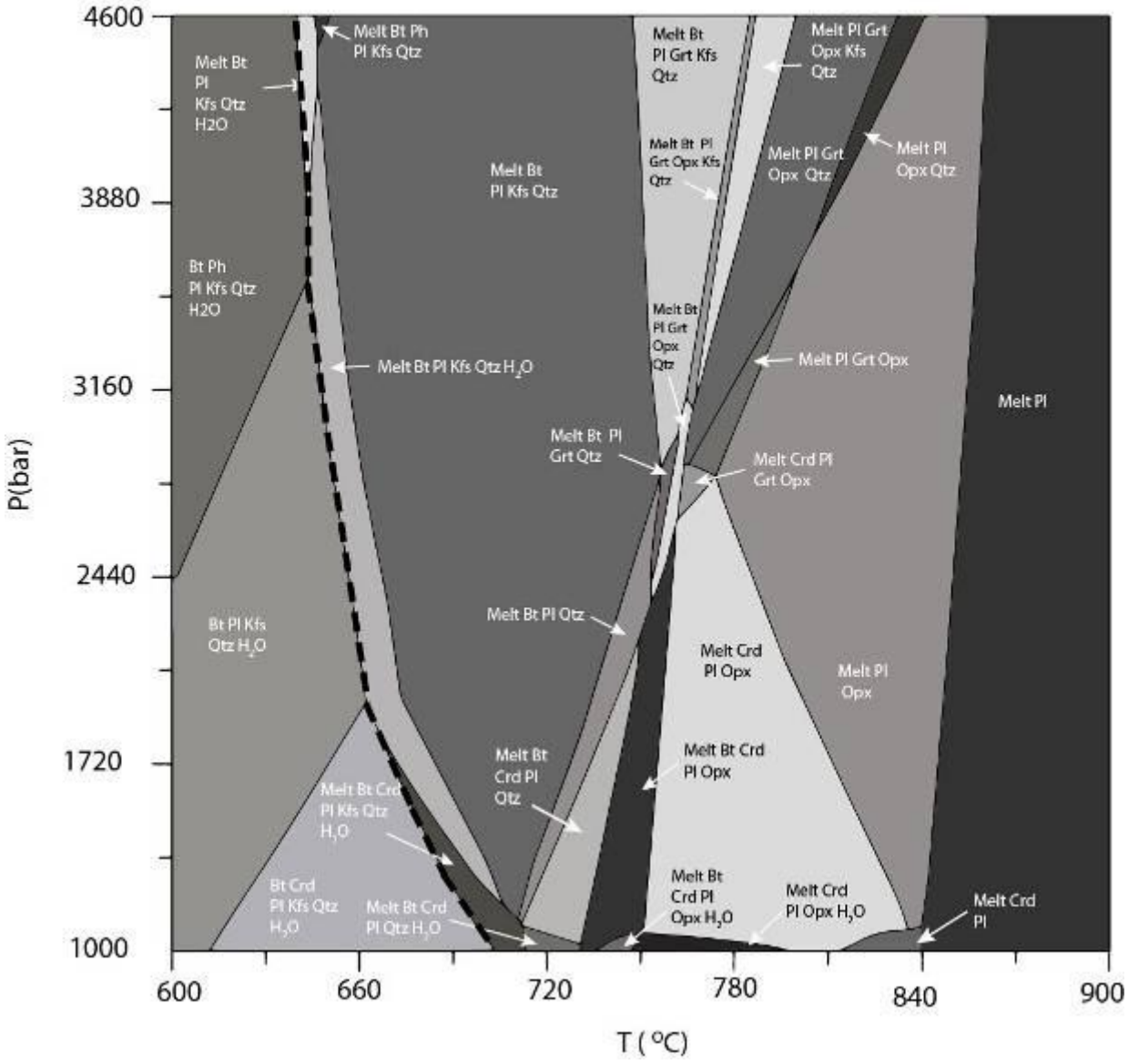

Figure 12: Partial P-T phase diagram for the rhyolitic rocks, as exemplified by sample A3, in the system NCKFMASH, using Perplex_X (Conolly 2009). The heavy dashed line represents the wet solidus. Pseudosection constructed for pressures ranging from 1 to 4.6 kilobars and temperatures ranging from 700 to 900 °C. Abbreviations: Bt = biotite, Grt = garnet, Kfs = k feldspar, Pl = plagioclase, Opx = orthopyroxene, Crd = cordierite, Qtz = quartz, Ph = phengite (abbreviations after Kretz, 1983).

	SiO_2	Al_2O_3	FeO	MgO	CaO	Na_2O	K_2O	H_2O
A3	69.61	14.45	2.77	0.44	1.65	2.69	5.40	3.00

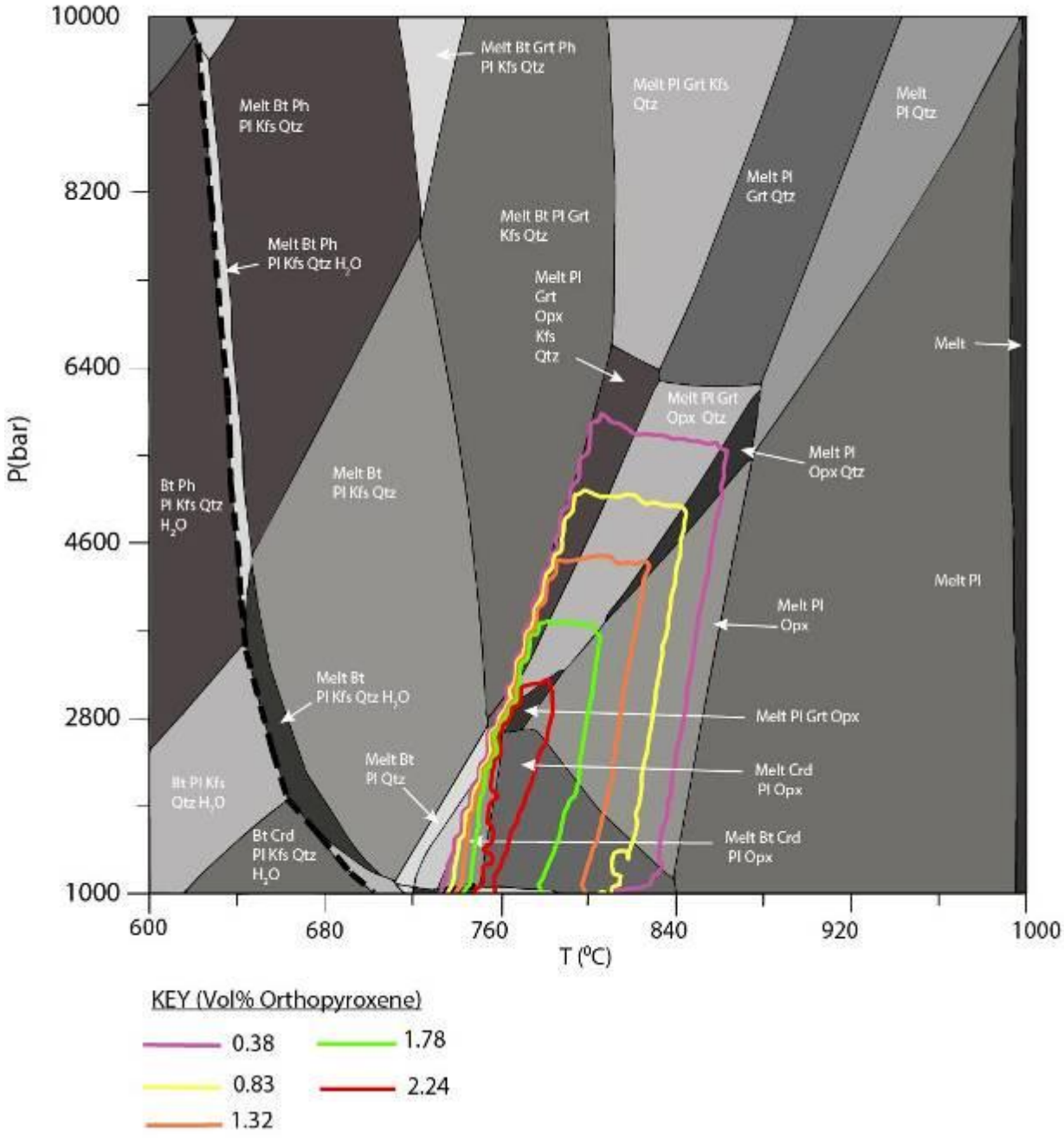

Figure 13: Partial P-T phase diagram for the rhyolitic rocks, as exemplified by sample A3, in the system NCKFMASH, using Perplex_X (Conolly 2009). The heavy dashed line represents the wet solidus. Contours for the volume % orthopyroxene are illustrated on the pseudosection. Abbreviations: Bt = biotite, Grt = garnet, Kfs = k feldspar, Pl = plagioclase, Opx = orthopyroxene, Crd = cordierite, Qtz = quartz, Ph = phengite (abbreviations after Kretz, 1983).

	SiO_2	Al_2O_3	FeO	MgO	CaO	Na_2O	K_2O	H_2O
A3	69.61	14.45	2.77	0.44	1.65	2.69	5.40	3.00

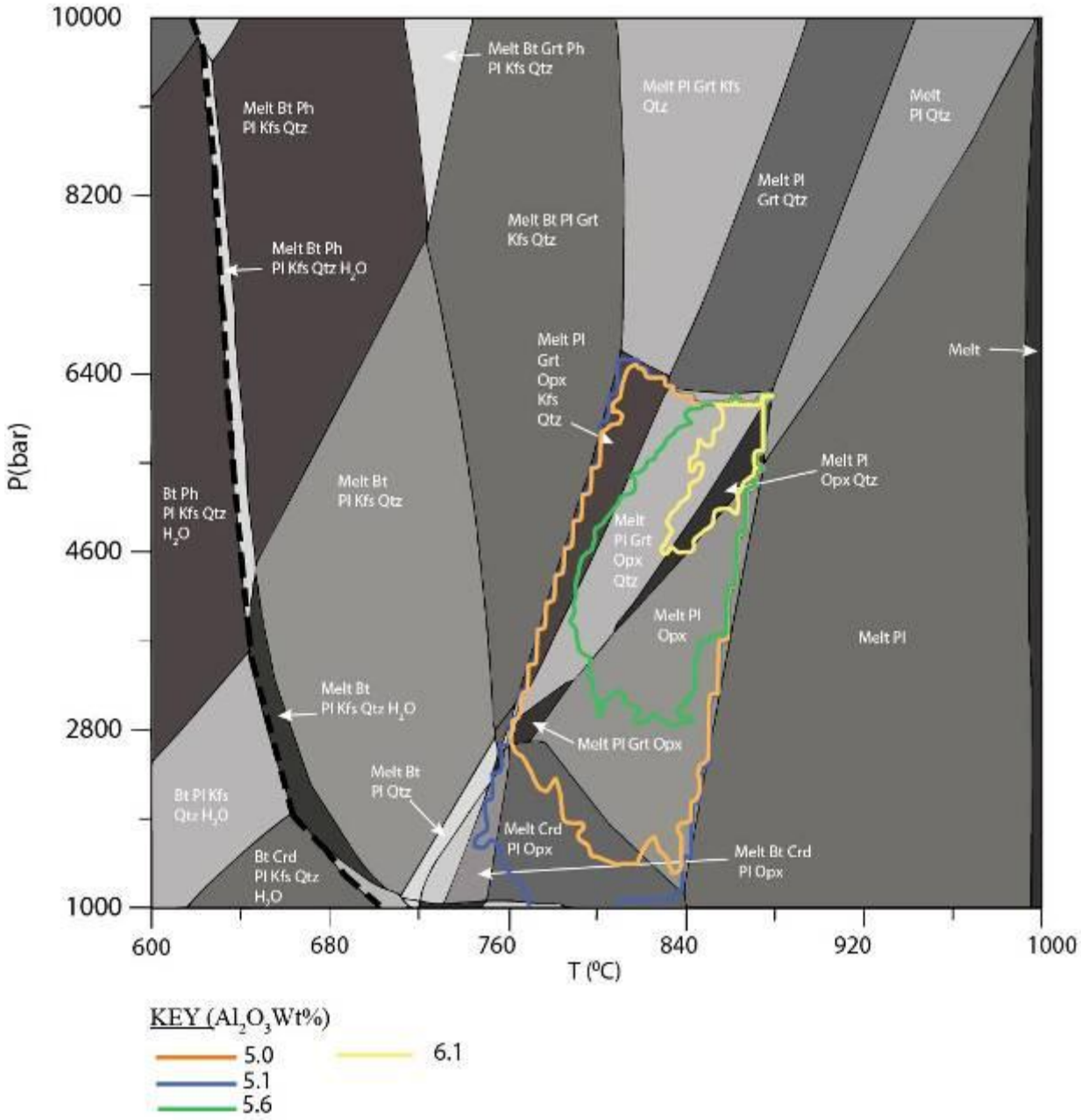

Figure 14: Partial P-T phase diagram for the rhyolitic rocks, as exemplified by sample A3, in the system NCKFMASH, using Perplex_X (Conolly 2009). The heavy dashed line represents the wet solidus. Contours for the Al_2O_3 content of orthopyroxene are illustrated on the pseudosection. Abbreviations: Bt = biotite, Grt = garnet. Kfs = k feldspar, Pl = plagioclase, Opx = orthopyroxene, Crd = cordierite, Qtz = quartz, Ph = phengite (abbreviations after Kretz, 1983).

	SiO_2	Al_2O_3	FeO	MgO	CaO	Na_2O	K_2O	H_2O
A3	69.61	14.45	2.77	0.44	1.65	2.69	5.40	3.00

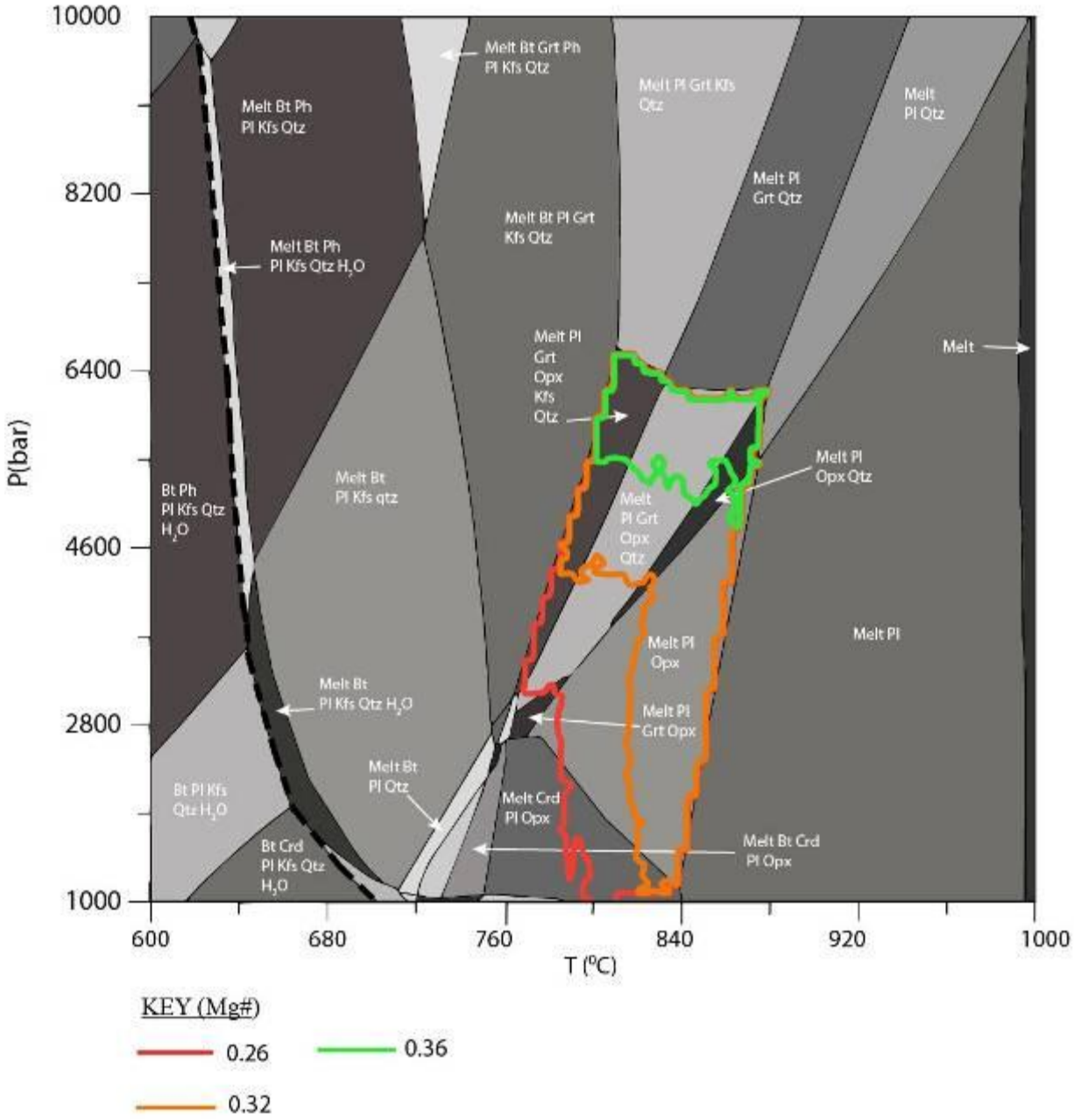

Figure 15: Partial P-T phase diagram for the rhyolitic rocks, as exemplified by sample A3, in the system NCKFMASH, using Perplex_X (Conolly 2009). The heavy dashed line represents the wet solidus. Contours for Mg # of orthopyroxene are illustrated on the pseudosection. Abbreviations: Bt = biotite, Grt = garnet, Kfs = k feldspar, Pl = plagioclase, Opx = orthopyroxene, Crd = cordierite, Qtz = quartz, Ph = phengite (after Kretz, 1983).

8 Discussion

8.1 Petrographic constraints on the origin of the Saldahna Tuffisite-Quartz Porphyry

The information provided in the preceding sections allow important new insights into the petrogenesis of the rhyolitic rocks of this study. This information is useful in resolving the ambiguity around the nature of the Saldahna tuffisite/Quartz porphyry noted by Scheepers and Poujol, 2002.

8.1.1 Summary of Textures

The rocks of both textural groups exhibit distinct textural features which collectively allow conclusions to be drawn regarding their eruptive or intrusive origins. Embayed quartz and feldspar can be observed in rocks of both groups. Phenocrysts are either euhedral or anhedral and exhibit deep regular embayments. Broken and shattered phenocrysts are commonly observed in both groups, although the proportion of broken phenocrysts is higher in the group 2 rocks which are characterised by cryptocrystalline matrix material. Phenocrysts also contain inclusions of matrix crystals with numerous unoriented cracks. The rocks of the second group also exhibit fine grained elongate domains, lighter in colour, which seem to define a flow foliation as illustrated in the petrography. These features vary range in size from 2 to 8 mm and are always found curved around the phenocrysts. These features when developed in the size range of 6 to 8 mm in thin section resemble fiamme (Fig. 6 (d)). The same feature can be observed in polished slabs ranging in length from 3 to 5 cm (Fig. 4 (c)) and defining coarser or finer grained domains in thin section with distinct boundaries and resemble fiamme whilst the smaller size fraction which range in size from 2 to 4 mm seem to define a flow texture (Fig 6(e)). The term fiamme, follows that of Bull and McPhie (2007), in which a fiamme is described as a term for an “elongate lenses or domains of the same mineralogy, texture and composition, which define a pre-tectonic foliation, and are separated by domains of different mineralogy, texture or composition”. From the foregoing, the elongate domains previously described are considered to be fiamme.

It is proposed that the rocks of this study represent eruptive pyroclastic rocks. The primary diagnostic feature that suggests an eruptive, explosive origin is the common occurrence of broken phenocrysts. Broken phenocrysts are observed in rocks of both group’s one and two.

8.1.2 Obscurity of vitroclastic and eutaxitic features in rheomorphic tuffs

Rocks of both groups do not exhibit the full range of distinct vitroclastic or eutaxitic textures. Shards, pumice, lithic fragments and broken phenocrysts are often regarded as unequivocal evidence of a pyroclastic origin (Henry and Wolf, 2002). These features are however found to be absent in many rheomorphic tuffs because of several factors which work to disguise primary textures such as shards and pumice throughout ash-flow tuffs (Henry and Wolf, 2002; Best and Christiansen, 1997). The tops and interiors of strongly rheomorphic tuffs from extensive silicic units are subject to intense recrystallization within the interior of a flow which can commonly disguise primary textures or result in their obliteration (Henry and Wolf, 2002). In addition dense welding that commonly occurs throughout high-temperature ash-flow tuffs, even in those that do not undergo secondary flow acts to obscure primary

features. In addition post depositional processes such as devitrification by metamorphism or hydrothermal alteration has made positive recognition of these high temperature ash-flow tuffs difficult (Henry and Wolf, 2002).

Intense recrystallization which occurs as a result of dense welding or devitrification could serve to explain the absence of features such as shards and pumice in the rocks of this study. These processes would also obscure features such as fiamme, with distinct outlines in recrystallized rocks being the only indication of their original appearance. Broken phenocrysts can be observed as they're presence is not affected by these post depositional processes. The growth of poikilitic sub-solidus biotite as well as overgrowths of matrix quartz and biotite laths on feldspar phenocrysts attest the intense recrystallization these rocks have undergone, in particular the rocks of the first group in which the foregoing features are more common, as a consequence of the heat developed due to the overlying volcanic pile.

8.1.3 Devitrification of volcanic glass

The primary distinction between rocks of the first group and rocks of the second group is a difference in the average crystal size of the matrix. The matrix of these rocks would have initially consisted of glass which through devitrification and recrystallization would attain their current texture. Textures produced by the devitrification of glass have been described by Lofgren (1971) who experimentally reproduced the transformation of natural glasses to wholly crystalline rocks in the temperature and pressure ranges of 240 to 700°C and 0.5 to 4 kb, respectively.

Three stages were identified to categorize the three dominant textural associations in partially and completely devitrified rhyolitic glass. The three stages consist of a glassy stage characterised by glassy or felsitic textures with isolated spherulites, a spherulitic stage characterised by spherulitic textures and micropoikilitic quartz and a third stage which can either be granophyric or granitic in texture. The last stage records little or no evidence of a glassy precursor. Rocks that had undergone recrystallization to the last stage would be recognized as volcanic on the grounds of field evidence and petrographic evidence within phenocryst assemblage, rather than by textures within glassy components or indicative of glass. In the experiments of Lofgren (1971), the transition to the granophyric or granitic stage is marked by the progressive recrystallization of the fibres of spherulites, axiolites, and the globulites into larger crystals. If the fine-grained feldspar continued to recrystallize, it would most likely enclose the quartz in the manner of a granophyre. Where poikilitic quartz is absent, the resulting texture would most likely be that of equigranular granite. For a granitic or granophyric texture to be produced, the pressure and temperature would have to be maintained for a substantial period of time, either during initial cooling or during subsequent reheating (Lofgren, 1971). Lofgren (1971) proposed that water would probably be near saturation for the glass, and there would probably be a separate vapour phase present as the recrystallization occurred.

Following these interpretations, the rocks of both groups identified in this study would therefore represent the third stage of devitrification proposed by Lofgren (1971) in which

primary eutaxitic and vitroclastic fabric would be absent. The recrystallization of these rocks would be the facilitated by the associated rheomorphism and welding during emplacement.

8.1.4 Broken phenocrysts

Broken phenocrysts are readily observed in thin section in rocks of both groups of this study. Effusive and very weakly explosive eruptions are characterised by evenly distributed, euhedral phenocrysts in a flow banded or massive groundmass whereas the products of explosive eruptions are characterised by broken and uneven crystal distribution as well as vitroclastic matrix textures (e.g. Branney et al., 1992; Best and Christiansen, 1997; Allen and McPhie, 2003). Best and Christiansen (1997) experimentally simulated the fragmentation of phenocrysts by mutual impact in a fast-moving mixture of vitric particles and crystals. Textural evidence suggested that cuspate, embayed fragments of phenocrysts are most likely to have formed through the rupture of contained inclusions within a vesiculating rhyolitic melt before the fragmentation of the magma. The decompression of an ascending magma surrounding a crystal can result in stress within a crystal, in the region surrounding a melt inclusion, to exceed the tensile strength of a crystal. This will cause the crystal to crack. The crack is accompanied by the decompression of the melt within the inclusion, the exsolution of volatiles and the further expansion of the inclusion until the crystal blows apart.

The broken phenocrysts therefore indicate an explosive eruption as supposed to an effusive eruption which would be characterised by an even distribution of euhedral phenocrysts in a massive or flow banded groundmass. Phenocrysts can be observed to contain cavities often filled with matrix crystals. The cavities can also be observed along breakage planes for pairs of broken phenocrysts. These cavities could potentially represent former melt inclusions which would rupture in a vesiculating magma prior to its fragmentation during decompression (Best and Christiansen, 1997).

8.2 Contacts

The finer grained rocks developed at the contacts with the coarse grained granite are texturally identical to rock textures of group two. These rocks are regarded as quartz porphyry by Scheepers and Poujol (2002). The occurrence of granite enclaves of the country granite in the finer-grained rocks as well as the occurrence of rhyolitic veins intruded into the granite support a shallow level intrusive nature for these rocks. In contrast, textures such as broken phenocrysts and textures resembling flow textures and fiamme suggest an eruptive pyroclastic origin. Consequently, these specific rocks recording intrusive relationships are interpreted to represent a pyroclastic feeder dyke system or fissure ignimbrites, through which the overlying ignimbrite deposit consisting of rocks of group one was built.

Pyroclastic dykes are classified under a range of geological forms encapsulated under the term clastic dykes and form an interface between the subvolcanic intrusive system and extrusive explosive processes in intermediate to silica-rich volcanic systems. Winter et al. (2008) envisaged two possible formation scenarios for pyroclastic dykes. The first would represent a mixture molten, fragmented magma which solidified during its ascent. The second is described as intra-vent fall-back from a collapsing eruption column. Winter et al. (2008) further noted that the resulting textures are similar. The first scenario is favoured for

pyroclastic dykes in classical caldera systems, e.g. vents and conduits which contain densely welded ignimbritic rock in the deep parts of intracaldera ignimbrites (Sparks et al., 1999). Branney and Kokelaar (1994) proposed scenarios similar to those of Winter et al. (2008) for subvertical, disconcordant bodies of sheared high grade tuff which are enclosed by older stratigraphic units which they observed in the Scafell caldera in the British Lake district. These bodies were termed ignimbrite vents.

8.3 Petrogenetic Modelling

8.3.1 Major and Trace Element Variability

The rocks of both groups one and two exhibit compositional ranges for K_2O and Na_2O which are regarded as characteristic of S-type granites based on the compositional ranges defined by Chappell and White (1974). Na_2O ranges between 2.25 and 2.81 wt. %; K_2O ranges between 5.09 and 5.83 wt. %. One other parameter used in the distinction of I-type granites from S-type granites is the aluminium saturation index, with S-type granites usually exhibiting values above 1.1 and I type granites usually exhibiting values below 1.1. The finer grained rocks of group two have an ASI values greater than 1.1 (1.11-1.15) whereas the rocks of group one range in value between 1.05 and 1.14. A trend which is exhibited by the rocks of this study is a decrease in ASI with increasing maficity. Clemens and Stevens (2011) illustrated that I-type granites trend towards a metaluminous character with higher values of maficity. The rocks do not contain hornblende usually associated with metaluminous I-type granites nor do they contain cordierite and garnet which are found in peraluminous S-type granite. The rocks of both groups contain a characteristic accessory mineral in sphene which is present in I-type granites and absent in S-type granites. Thus, the rocks studied show intermediate characteristics between S and I-type granites.

A set of bivariate diagrams comparing the rocks of this study (designated group one and group two) with those of Scheepers and Poujol (2002) (described as subvolcanic and volcanic) are illustrated in Figure 16. Systematic discrepancies can be observed for the rock compositions plotted below between rock compositions published by Scheepers and Poujol (2002) and rock compositions of this study. Both sets of data exhibit a near identical range in maficity. Data published by Scheepers and Poujol (2002) exhibit lower Al, K and Ti contents, higher Si content, and lower Na for volcanic rocks and higher Na for subvolcanic rocks. The reason for the apparent discrepancy between both data sets could not be established.

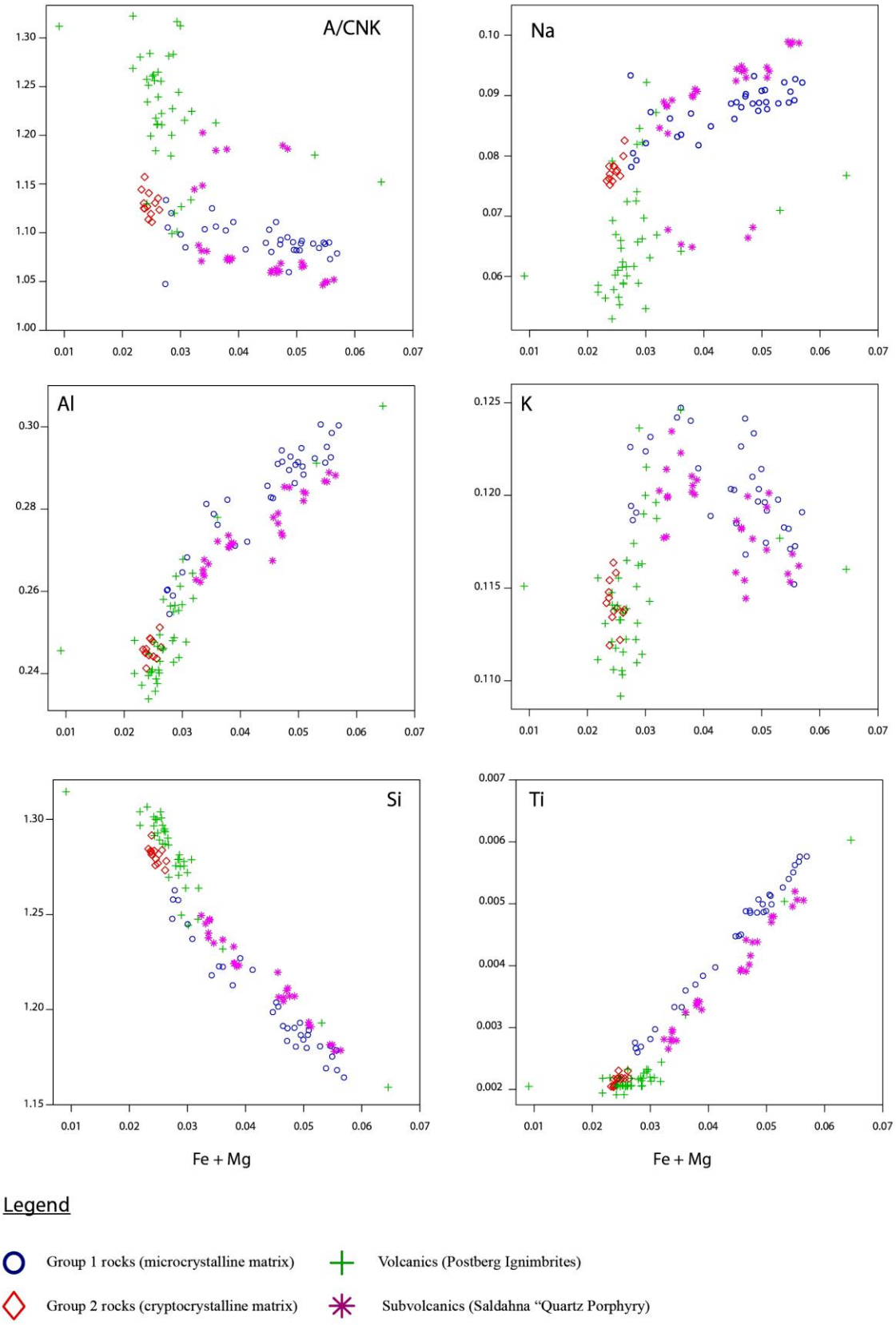

Figure 16: Variation diagrams of major elements plotted against maficity. Data plotted represents rock compositions obtained for this study as well as rock compositions obtained from Scheepers and Poujol (2002) described as subvolcanics and volcanics.

8.3.2 Assessment of Petrogenetic Models

As described in the geochemistry section, the rocks of this study exhibit tight inter-element correlations for a number of elements when plotted against maficity, e.g. Ti, Na, Ca, and Zr. An evaluation of models which have proposed to account for peraluminous granites which exhibit similar trends was undertaken by Stevens et al. (2007) and Clemens and Stevens (2012). The findings which were summarised earlier found existing models (e.g. liquid crystal fractionation and magma mixing) inadequate in explaining these inter-element correlations, e.g. the tight positive correlation of Ti with Mg+ Fe combined with the negative correlation of K with maficity which rules out biotite accumulation by any process as the mechanism for producing the Ti: maficity correlation. In combination, these studies proposed that in both S and I-type granites, the tight Ti: maficity correlation is a consequence of peritectic assemblage entrainment. The tight inter-element correlations exhibited by the rocks of this study possibly challenge this hypothesis because of the complexity in the behaviour of K relative to maficity. The relative roles of fractional crystallization and peritectic assemblage entrainment are considered below. Mixing with a mafic magma is not considered as a mechanism to account for the chemical range portrayed by these rocks for two reasons. Firstly, mantle derived mafic magmas are characterised by variable Ti: maficity ratios (Stevens et al 2007). Thus, a particular mafic magma of unusual Ti: maficity ratio would need to be involved in the petrogenesis of these granites and all other granites showing the same Ti: maficity ratio. This is considered to be very unlikely. Secondly, the rocks of this study are characterised by low Cr and Ni contents that do not correlate tightly with maficity. These trace elements are typically substantially more enriched in mafic magmas than in granites. Therefore, if the major mechanism shaping the compositional range of the Saldahna rocks was mixing with a mafic magma, it is predictable that elements such as Cr and Ni should show a positive correlation with maficity.

8.3.2.1 Crystal Fractionation

By convention, a trace element approach is adopted for fractionation modelling. For a fractionation model to be viable, compatibility with the major elements should exist. Consequently, a major element approach is adopted here. The flexibility afforded in modelling trace elements due to uncertainties in the distribution coefficients, proportions of minerals and the fractionating assemblage can reproduce observed trends.

The fractionation of selected phases is modelled based on the following mass balance equation: $c_l^i = \frac{c_o^i - c_{\min}^i f_c}{(1 - f_c)}$. O represents the least evolved magma composition which is taken to be the most mafic sample, min would represent the mineral being fractionated and l represents the unknown chemistry of the differentiated melt.

On Figure 17 mineral vectors indicate the direction of displacement expected for the liquid following the removal of the fractionating phase. The cumulate compositions will lie in the opposite direction. The modelled trends represent fractionation of 8 wt% biotite, 1wt% ilmenite, 5 wt% plagioclase, 3 wt% orthopyroxene and 10 wt% of a fractionating assemblage consisting of 19% biotite and 81% plagioclase are illustrated in Figure 17. The compositions

of the minerals used are those of the phenocrysts obtained for the selected samples described in the mineral chemistry. It is important to note that the fractionation of these phases in amounts greater than those considered results in the exhaustion of elements in the hypothetically differentiated melt. As can be seen in the Figure 17, the fractionation of the phases considered does not consistently account for all of the observed trends. A fractionating assemblage consisting of plagioclase and biotite in the proportions stated can best approximate the trends exhibited by the rocks of this study. This assemblage is however inadequate in accounting for trend exhibited for Ti, Na or A/CNK.

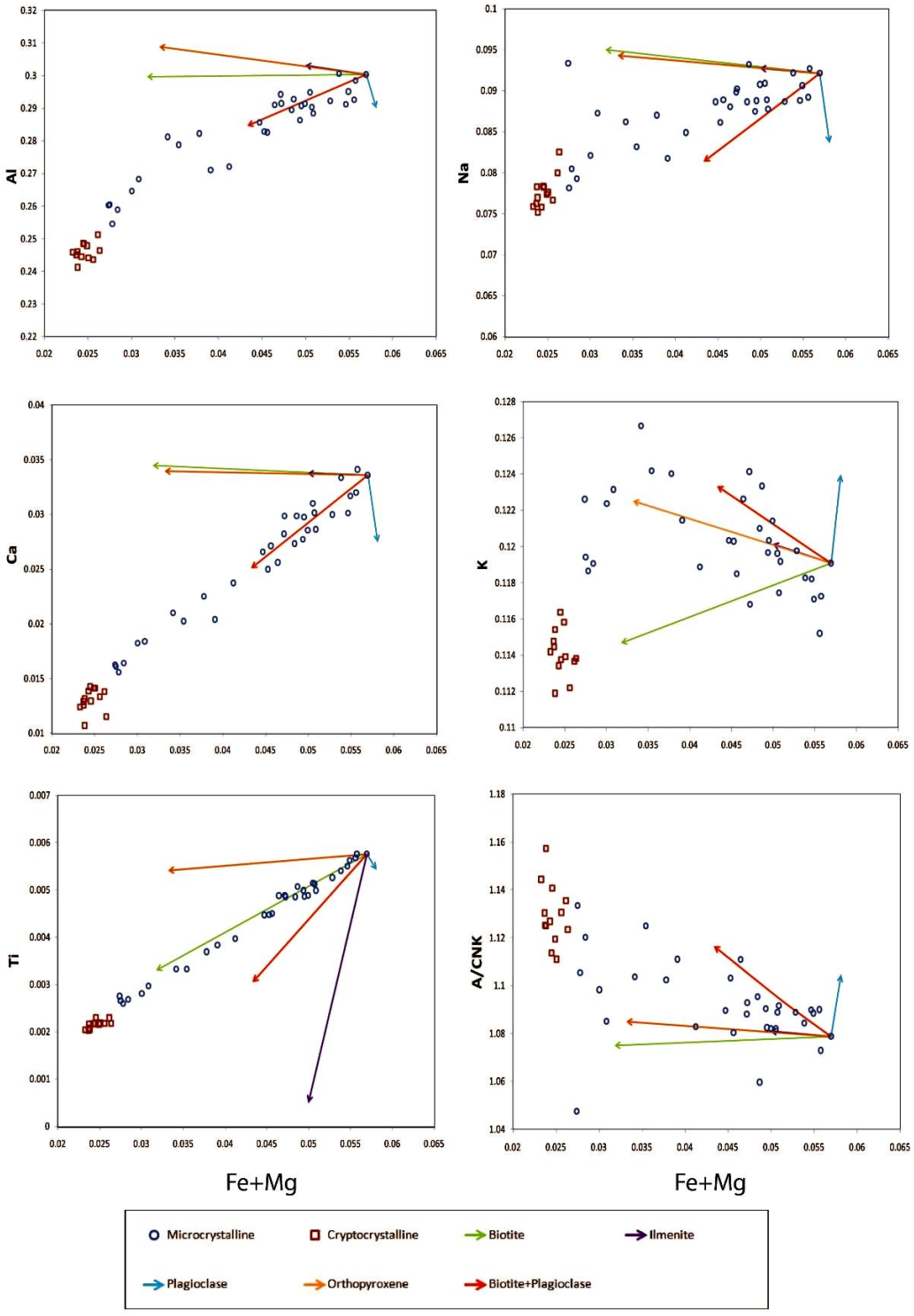

Figure 17: Major element plots of the rocks of this study against maficity. Plots show's vectors calculated for the fractionation of 8% biotite, 1% ilmenite, 5% plagioclase and 3% orthopyroxene phenocryst phases. Circles represent rocks of group one and the red squares represent rocks of group two.

8.3.2.2 Peritectic Phase Entrainment

It is proposed that tight inter-element correlations similar to those exhibited by the rhyolitic rocks of this study are produced in the source, through the entrainment of the peritectic assemblage to the magma (Stevens et al., 2007). A distinctive difference between S and I-type granites is a decreasing trend of A/CNK with maficity in I type granites (Stevens and Clemens, 2012). A negative A/CNK/maficity trend is exhibited by the rocks of this study. Stevens and Clemens (2012) proposed that this trend reflects the entrainment of a peritectic assemblage consisting of Opx+ Cpx+ Pl+ Ilm produced as a consequence of biotite and hornblende incongruent melting. An appropriate peraluminous felsic melt could be produced through the fluid absent melting of volcanic rocks, e.g. potassic andesite to dacite, or biotite to hornblende-rich granodioritic to tonalitic rocks.

As discussed previously, the characteristic correlation which exists between Ti and maficity in most granites as well as in the rocks of this study cannot be adequately explained by models which are usually invoked to account for compositional variation in granites. The exceptionally tight Ti: maficity correlation requires that in these rocks, the biotite, orthopyroxene, titanite and ilmenite proportions always resolve themselves at a constant Ti: Fe+ Mg ratio, irrespective of the maficity of the sample. The fact that these minerals have different size-density relationships and appear at different stages in the crystallization sequence argues very strongly against the Ti: maficity correlation being the consequence of fractional crystallization. This exceptionally tight correlation can be readily interpreted to reflect entrainment of a peritectic assemblage consisting of peritectic orthopyroxene and ilmenite.

A peritectic assemblage formed by these phases' points to the partial melting of a source undergoing coupled biotite and hornblende fluid-absent melting. The decrease in ASI with maficity is a consequence of peritectic clionopyroxene entrainment, which occurs in a rock undergoing fluid-absent incongruent melting involving hornblende as a reactant. The Al, Ca and Na correlations with maficity argues for the co-entrainment of peritectic plagioclase.

A balanced reaction model in a suitable source rock can be used to evaluate the role of PAE with the resultant compositions being shaped by the stoichiometry of the melting reaction. The magmas can be modelled as melt in addition to peritectic plagioclase, orthopyroxene, clionopyroxene, ilmenite and albite. The proportions of these components are presented below. The balanced reaction and magma compositions are provided in the appendix.

Reaction: 0.416 Hornblende + 1.2Biotite + 11.57 Quartz + 9.158 Plagioclase (An 40) = 16.91 Melt + 7.5Plagioclase (An 42) + 0.643 Ilmenite + 4.898Orthopyroxene+ 2.195 Clinopyroxene

The magma compositions which are produced by the variable entrainment of the peritectic assemblage upon the incongruent melting of biotite and hornblende closely approximate the

compositional trends defined by the rocks of this study, with the exception of K. The vector illustrated in Figure 11 represents varying degrees of peritectic assemblage entrainment which reflects the stoichiometry of the melting reaction. The initial starting point represents a suitable hypothetical melt composition. The next two red points would result from the entrainment of 5 and 10 mol. % of the peritectic assemblage produced by the coupled incongruent melting of biotite and hornblende in a ratio of 1:2.88. The model reactant hornblende has 2 wt% H_2O, 1.96 Al p.f.u and 2.5 wt% TiO_2 and biotite has 4.2 wt% TiO_2 and 2.68 Al pfu. The protolith is assumed to contain sufficient quartz and plagioclase, so that these reactants do not limit the degree of melting. The reactant plagioclase is assumed to be An_{40} and the peritectic plagioclase An_{42}. The balanced reaction as well as the anhydrous magma compositions which would be produced from the entrainment of the peritectic assemblage to the melt in varying proportions is provided in the appendix.

The compositional trends for rocks of the second group are however not accounted for by the modelling, for Al, Si and K. Two possible scenarios can be considered to account for the trends exhibited at lower maficity (0.023-0.031) for Al, Si and K. The first would be the removal of either k-feldspar or biotite from a rock composition (e.g. B23) which represents the point of inflection for the trends exhibited by Si, Al and K versus maficity. The removal of biotite could be considered as it is found in lower abundance in rocks of the second group, e.g. an absence of biotite glomerocrysts and acicular biotite commonly observed in rocks of the first group. The removal of either biotite or k-feldspar does not however account for trends exhibited for Si, Al or K with antithetic trends being produced as a consequence of their removal. The second possibility could be a different source for rocks of the second group. The source protolith would contain lower abundances of K and Al, and a higher abundance of Si.

The co-entrainment of an accessory suite consisting of zircon, ilmenite, apatite and monazite controls the concentration of elements that are hosted within these minerals. This accounts for the fact that elements concentrated in these minerals, e.g. Hf and Zr (High Field Strength Elements) in Zircon and REE's in monazite correlate positively with compatible major elements that do not reflect their solubilities in the melt, but rather the operation of peritectic assemblage entrainment.

The rocks of the second group display LREE depletion compared to rocks of the first group. This is due to the lower abundance of monazite which is commonly hosted in the Fe-Ti oxide clots which are absent in the finer grained rocks. The source protolith for the rocks of the second group would therefore exhibit a lower abundance of monazite which hosts LREE.

Peritectic grains are not necessarily present in the observed petrography. These peritectic grains readily re-equilibrate with the magma during ascent and emplacement due to their small grain size. Villaros et al. (2009) noted how garnet which is preserved in the CGS granites has equilibrated through a dissolution-precipitation process, at low pressures within the magma chamber. A similar argument can be made for orthopyroxene which occurs as corroded phenocrysts surrounded by a reaction rim of biotite. Clemens and Wall (1988) suggested that the presence of orthopyroxene in volcanic S-type rocks is a result of rapid

pressure quenching of the magma which halts crystallization at an early stage and noted that an increase in H_2O and $KAlSi_3O_8$ activity during the normal course of crystallization would result in the formation of biotite at the expense of orthopyroxene . Orthopyroxene is usually absent in granitoids of equivalent composition.

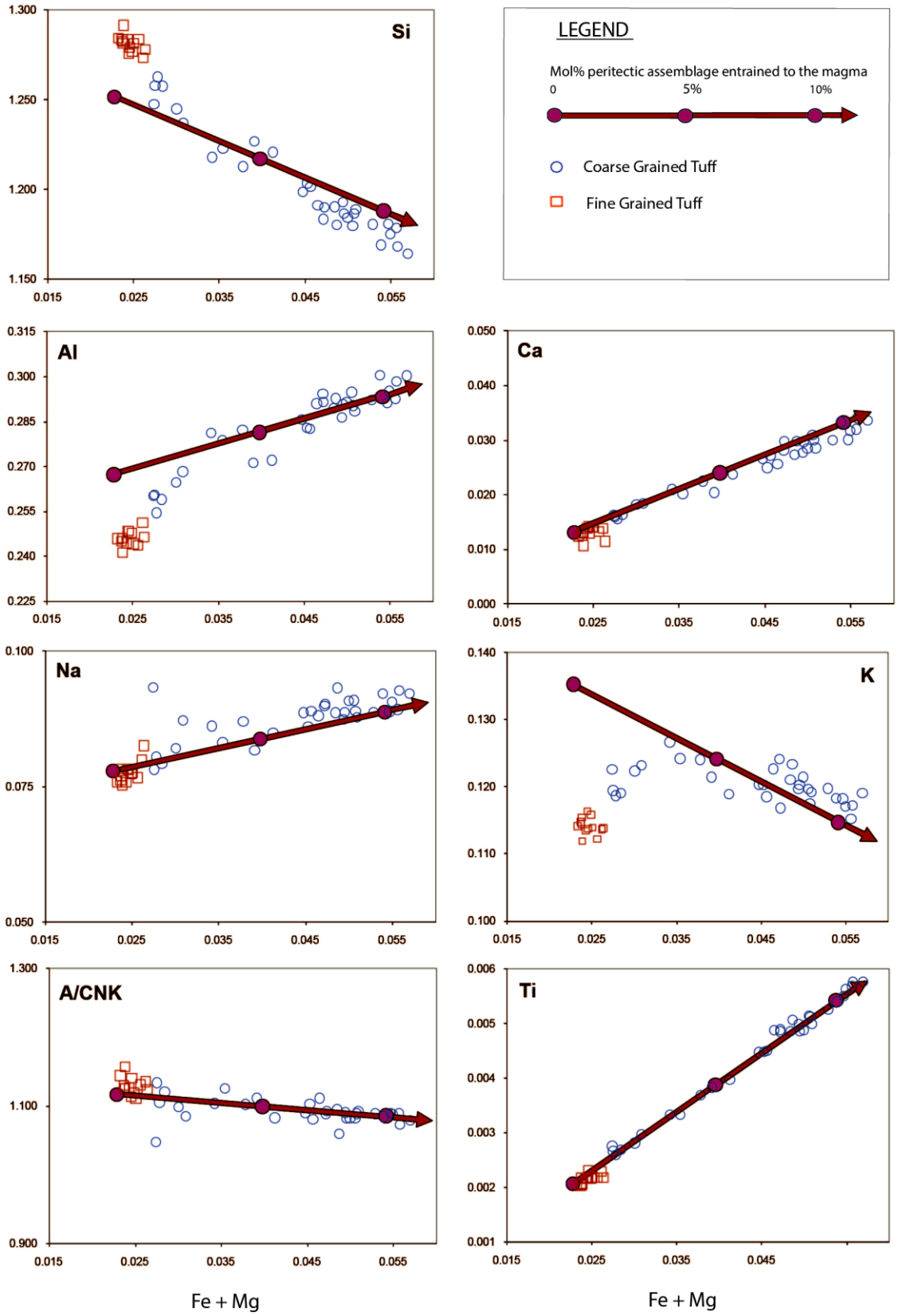

Figure 18: The rock compositions of this study compared with the magma compositions produced by peritectic assemblage entrainment (blue circles). The trend resulting from the mol% of peritectic assemblage entrained to the magma is indicated by the red circles as illustrated in the legend provided.

8.3.2.3 Constraining the conditions of formation of for Orthopyroxene

Orthopyroxene is stable between temperatures of 740 and 880°C and pressures below 6.85 kilobars. The pseudosection therefore illustrates that orthopyroxene observed in thin section is not peritectic. Magmatic orthopyroxene increases in vol. % as a function of decreasing pressure and decreases in Al content as a function of decreasing pressure. The highest measured aluminium content for a pyroxene is 2.83 wt % for sample MB 1 which represent conditions far lower than those illustrated in the pseudosection (5.0 - 6.1 wt%). This indicates that orthopyroxene observed in thin section has most likely undergone a dissolution-precipitation process at low pressures within the magma chamber. Garnet would react to orthopyroxene, followed by the modification of orthopyroxene composition as the magma continued to decompress. At lower pressures and temperatures, pressures less than 2800 kbar and temperatures less than 840°C cordierite becomes a stable phase and is present in the stability fields. Cordierite is however not observed in the mineral assemblage. The absence of cordierite in the rocks would indicate that the magma reached the solidus at temperatures (e.g. 800°C) above that of any stability field containing cordierite.

9 Conclusion

The textural investigation has considered the features of these rocks, primarily the presence of broken phenocrysts and micropoikilitic biotite to suggest an eruptive pyroclastic origin for rocks which fall under the designation of the two groups. Rocks which exhibit textures of either group can therefore be classified and termed as either Saldahna tuffisite (Scheepers and Poujol, 2002) or ignimbrite and represent an extensive, well exposed rheomorphic rhyolitic tuff which juxtaposes the Postberg ignimbrite. Post depositional processes of welding, compaction and devitrification related to lithostatic load have facilitated pervasive post depositional granophyric/granitic crystallization which has led to the obliteration of primary eutaxitic and vitroclastic fabric, a feature which is commonly observed in high grade ignimbrite successions, e.g. Nuraxi tuff, Sardinia (Pioli and Rosi, 2005). The apparent contradiction inherent to the existence of intrusive contacts and the common presence of broken feldspar phenocrysts can perhaps be reconciled if these rocks are interpreted to represent a welded ignimbrite deposit that overlay the coarse grained granite, with subsequent intrusions by a later pulse of similar magma via what are now seen to be pyroclastic dykes which built the ignimbrite deposit along the contact with the coarse grained granite.

The major and trace element variation exhibited by these ignimbrites can be adequately accounted for through the entrainment of a peritectic assemblage consisting of plagioclase, orthopyroxene, clionopyroxene and ilmenite as well as the coupled entrainment of accessory mineral phases associated with biotite, e.g. monazite. The peritectic minerals, i.e. orthopyroxene, equilibrated within the magma, probably through reactions to form garnet and then through a dissolution–precipitation process once orthopyroxene formed at the expense of garnet during ascent. The contrast exhibited in K behaviour, Al and Si, as well as the depletion in LREE's for the finer grained ignimbrites would suggest their derivation from a source similar to that of their coarser grained counterparts, with the source exhibiting a lower K content as well as a lower abundance of monazite which hosts LREE's.

10 References

Aydar, E., & Gourgaud, A. (1998). The geology of Mount Hasan stratovolcano, central Anatolia, Turkey. *Journal of volcanology and geothermal research*, **85**(1), 129-152.

Allen, S. R., & McPhie, J. (2003). Phenocryst fragments in rhyolitic lavas and lava domes. *Journal of volcanology and geothermal research*, **126**(3), 263-283.

Bas, M. L., Maitre, R. L., Streckeisen, A., & Zanettin, B. (1986). A chemical classification of volcanic rocks based on the total alkali-silica diagram. *Journal of petrology*, **27**(3), 745-750.

Bateman, R. (1995). The interplay between crystallization, replenishment and hybridization in large felsic magma chambers. *Earth-Science Reviews*, **39**(1), 91-106.

Barnett, W., Armstrong, R. A., & de Wit, M. J. (1997). Stratigraphy of the upper Neoproterozoic Kango and lower Palaeozoic Table Mountain groups of the Cape fold belt revisited. *South African Journal of Geology*, **100**(3), 237-250.

Belcher, R. W., & Kisters, A. F. (2003). Lithostratigraphic correlations in the western branch of the Pan-African Saldania belt, South Africa: the Malmesbury Group revisited. *South African Journal of Geology*, **106**(4), 327-342.

Best, M. G., & Christiansen, E. H. (1997). Origin of broken phenocrysts in ash-flow tuffs. *Geological Society of America Bulletin*, **109**(1), 63-73.

Best, M. G., Christiansen, E. H., Best, M. G., & Christiansen, E. (2001).*Igneous petrology* .Oxford, Blackwell Science.-480pp

Boynton, W. V. (1984). Cosmochemistry of the rare earth elements: meteoric studies. *Rare earth element geochemistry*, 63-114.

Branney, M. J., & Kokelaar, P. (1994). Volcanotectonic faulting, soft-state deformation and rheomorphism of tuffs during development of a piecemeal caldera, English Lake District. *Geological Society of America Bulletin*, **106**(4), 507-530.

Branney, M. J., & Kokelaar, P. (1992). A reappraisal of ignimbrite emplacement: progressive aggradation and changes from particulate to non-particulate flow during emplacement of high-grade ignimbrite. *Bulletin of Volcanology*, **54**(6), 504-520.

Brophy, J. G. (2009). Decompression and H_2O exsolution driven crystallization and fractionation: development of a new model for low-pressure fractional crystallization in calc-alkaline magmatic systems. *Contributions to Mineralogy and Petrology*, **157**(6), 797-811.

Bull, K. F., & McPhie, J. (2007). Fiamme textures in volcanic successions: Flaming issues of definition and interpretation. *Journal of Volcanology and Geothermal Research*, **164**(4), 205-216.

Chappell, B. W., & White, A. J. R. (1974). Two contrasting granite types. *Pacific geology*, **8**(2), 173-174.

Clemens, J. D., & Mawer, C. K. (1992). Granitic magma transport by fracture propagation. *Tectonophysics*, **204**(3), 339-360.

Clemens, J. D., & Vielzeuf, D. (1987). Constraints on melting and magma production in the crust. *Earth and Planetary Science Letters*, **86**(2), 287-306.

Clemens, J. D., & Wall, V. J. (1981). Origin and crystallization of some peraluminous (S-type) granitic magmas. *The Canadian Mineralogist*, **19**(1), 111-131.

Clemens, J., & Watkins, J. (2001). The fluid regime of high-temperature metamorphism during granitoid magma genesis. *Contributions to Mineralogy and Petrology*, **140**(5), 600-606.

Clemens, J. D., & Stevens, G. (2012). What controls chemical variation in granitic magmas?. *Lithos*. **134-135**, 317-329

Clemens, J. D., & Mawer, C. K. (1992). Granitic magma transport by fracture propagation. *Tectonophysics*, **204**(3), 339-360.

Clemens, J. D., & Vielzeuf, D. (1987). Constraints on melting and magma production in the crust. *Earth and Planetary Science Letters*, **86**(2), 287-306.

Cleverly, R. W., & Bristow, J. W. (1979). Revised volcanic stratigraphy of the Lebombo monocline. *Transactions of the Geological Society of South Africa*, **82**(2), 227-230.

Collins, W. J. (1998). Evaluation of petrogenetic models for Lachlan Fold Belt granitoids: implications for crustal architecture and tectonic models. *Australian Journal of Earth Sciences*, **45**(4), 483-500.

Connolly, J. A. D. (1990). Multivariable phase diagrams; an algorithm based on generalized thermodynamics. *American Journal of Science*, **290**(6), 666-718.

Collins, W. J. (1998). Evaluation of petrogenetic models for Lachlan Fold Belt granitoids: implications for crustal architecture and tectonic models. *Australian Journal of Earth Sciences*, **45**(4), 483-500.

Connolly, J. A. D., & Petrini, K. (2002). An automated strategy for calculation of phase diagram sections and retrieval of rock properties as a function of physical conditions. *Journal of Metamorphic Geology*, **20**(7), 697-708

De Paolo, D. J. (1981). Trace element and isotopic effects of combined wallrock assimilation and fractional crystallization. *Earth and planetary science letters*, **53**(2), 189-202.

de Saint Blanquat, M., Horsman, E., Habert, G., Morgan, S., Vanderhaeghe, O., Law, R., & Tikoff, B. (2011). Multiscale magmatic cyclicity, duration of pluton construction, and

the paradoxical relationship between tectonism and plutonism in continental arcs. *Tectonophysics*, **500**(1), 20-33.

Eichelberger, J. C., Izbekov, P. E., & Browne, B. L. (2006). Bulk chemical trends at arc volcanoes are not liquid lines of descent. *Lithos*, **87**(1), 135-154.

Ekren, E. B., McIntyre, D. H., & Bennett, E. H. (1984). *High-temperature, large-volume, lavalike ash-flow tuffs without calderas in southwestern Idaho*. US Government Printing Office.

Fuhrman, M. L., & Lindsley, D. H. (1988). Ternary-feldspar modeling and thermometry. *American Mineralogist*, **73**(3-4), 201-215.

Gresse, P. G., & Scheepers, R. (1993). Neoproterozoic to Cambrian (Namibian) rocks of South Africa: a geochronological and geotectonic review. *Journal of African Earth Sciences (and the Middle East)*, **16**(4), 375-393.

Gresse, P. G., Chemale, F., Da Silva, L. C., Walraven, F., & Hartmann, L. A. (1996). Late-to post-orogenic basins of the Pan-African–Brasiliano collision orogen in southern Africa and southern Brazil. *Basin Research*, **8**(2), 157-171.

Hartnady, C. J. H., Newton, A. R., & Theron, J. N. (1974). The stratigraphy and structure of the Malmesbury Group in the southwestern Cape. *Bulletin precambrian research unit*, **15**, 193-213.

Henry, C. D., & Wolff, J. A. (1992). Distinguishing strongly rheomorphic tuffs from extensive silicic lavas. *Bulletin of Volcanology*, **54**(3), 171-186.

Holland, T. J. B., & Powell, R. (1998). An internally consistent thermodynamic data set for phases of petrological interest. *Journal of metamorphic Geology*,**16**(3), 309-343.

Holland, T., & Powell, R. (1996). Thermodynamics of order-disorder in minerals: II. Symmetric formalism applied to solid solutions. *American Mineralogist*,**81**(11), 1425-1437.

Holland, T. I. M., & Powell, R. (2001). Calculation of phase relations involving haplogranitic melts using an internally consistent thermodynamic dataset. *Journal of Petrology*, **42**(4), 673-683.

Irvine, T.N. and Baragar, W.R.A., 1971. A guide to the chemical classification of the common volcanic rocks. *Canadian Journal of Earth Sciences*, **8**, 523-548.

Kretz, R. (1983). Symbols for rock-forming minerals. *American mineralogist*,**68**, 277-279.

Lofgren, G. (1971). Spherulitic textures in glassy and crystalline rocks. *Journal of Geophysical Research*, **76**(23), 5635-5648.

Marsh, B. D. (2002). On bimodal differentiation by solidification front instability in basaltic magmas, part 1: basic mechanics. *Geochimica et Cosmochimica Acta*, **66**(12), 2211-2229.

Mc Birney, A. R., Baker, B. H., & Nilson, R. H. (1985). Liquid fractionation. Part I: Basic principles and experimental simulations. *Journal of Volcanology and Geothermal Research*, **24**(1), 1-24.

Milner, S. C., Duncan, A. R., & Ewart, A. (1992). Quartz latite rheoignimbrite flows of the Etendeka Formation, north-western Namibia. *Bulletin of Volcanology*, **54**(3), 200-219.

Milner, S. C. (1986). The geological and volcanological features of the quartz latites of the Etendeka Formation. *Comm Geol Surv Southwest Africa/Namibia*, **2**, 109-116.

Newton, R.C., Charlu T.V., & Kleppa O.J. (1980) Thermochemistry of the high structural state plagioclases. *Geochemica Cosmochimica Acta*, **44**, 933-941.

Perugini, D., & Poli, G. (2012). The mixing of magmas in plutonic and volcanic environments: Analogies and differences. *Lithos*, **153**, 261-277.

Poli, G., & Tommasini, S. (1999). Geochemical modeling of acid–basic magma interaction in the Sardinia–Corsica Batholith: the case study of Sarrabus, southeastern Sardinia, Italy. *Lithos*, **46**(3), 553-571.

Scheepers, R., & Armstrong, R. (2002). New U-Pb SHRIMP zircon ages of the Cape Granite Suite: implications for the magmatic evolution of the Saldania Belt. *South African Journal of Geology*, **105**(3), 241-256.

Scheepers, R., & Nortjé, A. N. (2000). Rhyolitic ignimbrites of the Cape Granite suite, southwestern Cape province, South Africa. *Journal of African Earth Sciences*, **31**(3), 647-656.

Scheepers, R., & Poujol, M. (2002). U-Pb zircon age of Cape Granite Suite ignimbrites: characteristics of the last phases of the Saldanian magmatism. *South African Journal of Geology*, **105**(2), 163-178.

Scheepers, R., & Rozendaal, A. (1992). Relationship of the Riviera W (Mo Cu) deposit to magmatism in the southwestern Cape Province, South Africa. *Abstracts Geocongress 1992, Geological Society South Africa*, 339-341.

Scholtz, D. L. (1947). On the younger pre-Cambrian granite plutons of the Cape Province: Geol. *Soc. South Africa Proc*, **49**, 35-82.

Sparks, R.S.J, Tait, S.R., Yanev, Y. (1999). Dense welding caused by volatile resorption. Journal of the Geological Society, **156**(2), 217-225

Stevens, G., Villaros, A., & Moyen, J. F. (2007). Selective peritectic garnet entrainment as the origin of geochemical diversity in S-type granites. *Geology*, **35**(1), 9-12.

Ustunisik, G., & Kilinc, A. (2011). The role of fractional crystallization, magma recharge, and magma mixing in the differentiation of the Small Hasandag volcano, Central Anatolia, Turkey. *Lithos*, **125**(3), 984-993.

Villaros, A., Stevens, G., & Buick, I. S. (2009). Tracking S-type granite from source to emplacement: Clues from garnet in the Cape Granite Suite. *Lithos*,**112**(3), 217-235.

Villaros, A., Stevens, G., Moyen, J. F., & Buick, I. S. (2009). The trace element compositions of S-type granites: evidence for disequilibrium melting and accessory phase entrainment in the source. *Contributions to Mineralogy and Petrology*, **158**(4), 543-561.

Von Veh, M. W. (1983). *Aspects of Sedimentation, Structure, and Tectonic Evolution in the Tygerberg Terrane, Southwestern Cape Province*. University of Cape Town, Department of Geology, Chamber of Mines Precambrian Research Unit.

Waldbaum, D. R., & Thompson Jr, J. B. (1969). Mixing properties of sanidine crystalline solutions: IV. Phase diagrams from equations of state. *Am Mineral*, **54**, 1274-1298.

Wall, V. J., Clemens, J. D., & Clarke, D. B. (1987). Models for granitoid evolution and source compositions. *The Journal of Geology*, 731-749.

Winter, C., Breitkreuz, C., & Lapp, M. (2008). Textural analysis of a Late Palaeozoic coherent-pyroclastic rhyolitic dyke system near Burkersdorf (Erzgebirge, Saxony, Germany). *Geological Society, London, Special Publications*, **302**(1), 199-221.

White, R. W., Powell, R., & Holland, T. J. B. (2001). Calculation of partial melting equilibria in the system Na2O–CaO–K2O–FeO–MgO–Al2O3–SiO2–H2O (NCKFMASH). *Journal of Metamorphic Geology*, **19**(2), 139-153.

White, R. W., Powell, R., & Holland, T. J. B. (2007). Progress relating to calculation of partial melting equilibria for metapelites. *Journal of Metamorphic Geology*, **25**(5), 511-527.

White, A. J., & Chappell, B. W. (1977). Ultrametamorphism and granitoid genesis. *Tectonophysics*, **43**(1), 7-22.

Xu, W., Lithgow-Bertelloni, C., Stixrude, L., & Ritsema, J. (2008). The effect of bulk composition and temperature on mantle seismic structure. *Earth and Planetary Science Letters*, **275**(1), 70-79

11 Appendices

11.1 Appendix 1: Averaged Feldspar Compositions and Standard Deviations

11.1.1 Averaged Feldspar Compositions

Sample	A1				A3								
Group	2				1								
Feldspar	1	2	3	3-E	1	2	3	4	5	6	7	8	9
SiO_2	59.21	65.49	65.33	68.41	59.65	58.26	58.44	58.69	64.62	65.05	65.26	58.21	60.22
Al_2O_3	25.63	18.86	18.78	19.73	25.86	25.72	25.51	25.52	18.87	18.97	18.91	25.66	23.70
FeO	0.10	0.05	0.06	0.10	0.14	0.12	0.20	0.10	0.08	0.05	0.10	0.14	0.13
CaO	7.30	0.32	0.29	0.30	7.28	7.55	7.24	7.25	0.39	0.50	0.41	7.49	5.47
Na_2O	7.39	3.40	2.42	10.86	7.20	7.13	7.22	7.03	3.57	3.69	3.60	6.89	5.89
K_2O	0.85	11.98	13.29	0.18	0.95	0.79	0.89	0.94	11.39	11.05	11.37	1.03	4.13
BaO	0.05	0.31	0.30	0.08	0.09	0.03	0.03	0.04	0.47	0.40	0.32	0.05	0.13
SrO	0.10	0.09	0.12	0.03	0.10	0.03	0.12	0.06	0.05	0.06	0.05	0.08	0.06
Total	100.63	100.51	100.59	99.70	101.26	99.62	99.66	99.63	99.44	99.77	100.02	99.57	99.73

Sample	A3	A3A5				MB7		WP11					
Group	1	2				1		1					
Feldspar	10	1	2	3	4	1	2	1	2	3	4	5	6
SiO_2	57.92	65.24	65.13	59.93	58.53	58.36	65.20	65.60	66.42	64.73	65.64	59.38	58.28
Al_2O_3	26.12	19.06	19.09	25.08	25.51	25.96	18.91	18.84	18.14	18.70	18.92	24.83	26.05
FeO	0.12	0.07	0.04	0.21	0.11	0.12	0.07	0.06	0.33	0.06	0.06	0.14	0.13
CaO	7.66	0.37	0.36	6.00	7.27	7.45	0.32	0.33	0.49	0.26	0.34	6.41	7.65
Na_2O	7.31	3.27	3.38	6.81	7.42	7.20	2.84	3.83	4.50	3.36	3.68	7.46	7.12
K_2O	0.56	12.04	11.88	2.01	0.78	0.92	12.56	11.47	9.73	12.09	11.44	1.37	0.84
BaO	0.04	0.65	0.57	0.05	0.05	0.09	0.44	0.10	0.11	0.12	0.19	0.05	0.07
SrO	0.09	0.01	0.05	0.09	0.02	0.08	0.07	0.11	0.05	0.08	0.12	0.13	0.12
Total	99.84	100.70	100.51	100.18	99.70	100.19	100.40	100.34	99.78	99.40	100.40	99.78	100.25

Sample	WP 31						
Group	1						
Feldspar	1	1-E	2	3	4	5	5-E
SiO_2	64.75	67.60	58.54	57.95	58.12	65.02	65.78
Al_2O_3	19.08	19.81	25.54	25.76	25.65	19.07	21.19
FeO	0.07	0.05	0.16	0.36	0.22	0.06	0.07
CaO	0.37	0.29	6.87	7.11	7.33	0.30	1.78
Na_2O	3.70	10.95	7.97	7.88	7.57	3.52	10.95
K_2O	11.86	0.33	0.76	0.64	0.95	12.21	0.28
BaO	0.28	0.02	0.02	0.08	0.04	0.16	0.06
SrO	0.06	0.04	0.02	0.05	0.04	0.05	0.05
Total	100.16	99.08	99.87	99.83	99.90	100.38	100.17

11.1.2 Standard Deviations

Sample	A1				A3								
Group	2				1								
Feldspar	1	2	3	3-E	1	2	3	4	5	6	7	8	9
SiO_2	0.63	0.25	0.40	0.17	0.52	0.61	0.26	0.55	0.52	0.55	0.44	0.61	2.22
Al_2O_3	0.39	0.14	0.23	0.09	0.20	0.18	0.27	0.27	0.29	0.40	0.32	0.25	2.94
FeO	0.04	0.04	0.06	0.13	0.04	0.08	0.21	0.05	0.07	0.04	0.10	0.14	0.06
CaO	0.46	0.13	0.07	0.06	0.28	0.27	0.22	0.31	0.16	0.19	0.13	0.21	2.92
Na_2O	0.25	0.31	0.92	0.28	0.20	0.25	0.18	0.37	0.72	0.74	0.72	0.20	2.45
K_2O	0.11	0.37	1.22	0.04	0.09	0.20	0.15	0.17	0.95	0.95	0.97	0.07	5.58
BaO	0.05	0.03	0.09	0.08	0.05	0.03	0.04	0.03	0.17	0.11	0.09	0.04	0.15
SrO	0.09	0.07	0.11	0.05	0.10	0.05	0.12	0.07	0.05	0.07	0.09	0.09	0.06

Sample	A3	A3A5				MB7		WP11					
Group	1	2				1		2					
Feldspar	10	1	2	3	4	1	2	1	2	3	4	5	6
SiO_2	0.53	0.30	0.39	1.13	0.48	0.53	0.55	0.57	3.90	0.72	0.42	1.63	0.63
Al_2O_3	0.28	0.11	0.12	0.85	0.33	0.32	0.22	0.23	1.99	0.21	0.13	1.43	0.36
FeO	0.05	0.03	0.04	0.21	0.04	0.06	0.04	0.07	0.80	0.04	0.04	0.14	0.03
CaO	0.27	0.19	0.09	1.42	0.28	0.42	0.08	0.07	0.54	0.07	0.10	1.40	0.50
Na_2O	0.15	0.20	0.37	1.54	0.30	0.29	0.67	1.54	2.40	1.63	1.11	0.68	0.26
K_2O	0.09	0.41	0.46	1.80	0.07	0.04	0.91	2.01	3.92	2.21	1.53	2.05	0.06
BaO	0.04	0.12	0.06	0.04	0.03	0.05	0.16	0.08	0.06	0.09	0.08	0.04	0.05
SrO	0.08	0.02	0.04	0.07	0.03	0.09	0.06	0.08	0.06	0.09	0.12	0.09	0.07

Sample	WP31						
Group	1						
Feldspar	1	1-E	2	3	4	5	5-E
SiO_2	0.42	0.35	0.99	0.75	0.66	0.41	2.67
Al_2O_3	0.14	0.18	0.80	0.24	0.45	0.16	1.91
FeO	0.05	0.07	0.14	0.62	0.21	0.05	0.13
CaO	0.08	0.06	1.29	0.59	0.53	0.06	2.11
Na_2O	0.58	0.33	0.50	0.34	0.25	0.69	1.38
K_2O	0.81	0.28	0.27	0.21	0.22	1.02	0.12
BaO	0.07	0.02	0.03	0.06	0.04	0.06	0.08
SrO	0.05	0.06	0.03	0.07	0.04	0.08	0.08

11.2 Appendix 2: Averaged Pyroxene Compositions and Standard Deviations

11.2.1 Averaged Pyroxene Compositions

Sample	B19			MB 7		MB1					A3	
Pyroxene Grain	1	2	3	1-Rim	1-Core	1	2	3	4	5	1	2
SiO2	47.6	46.8	47.6	47.8	50.2	48.6	48.3	48.5	48.2	47.2	47.9	48.4
TiO2	0.20	0.23	0.23	0.17	0.10	0.17	0.20	0.18	0.20	0.19	-	0.24
Al2O3	1.79	1.97	1.74	1.74	1.60	1.85	1.79	1.72	1.85	2.38	1.87	1.82
Cr2O3	-	-	-	-	-	-	-	-	-	-	-	-
FeO	37.7	39.5	37.4	37.8	35.6	38.4	38.9	38.2	39.2	41.2	37.4	37.2
MnO	0.72	0.93	0.70	0.68	0.95	0.72	0.74	0.68	0.75	0.98	0.69	0.74
MgO	10.1	8.7	10.2	10.6	10.7	10.5	10.1	10.4	9.7	8.0	10.7	10.8
CaO	0.37	0.21	0.39	0.36	0.25	0.33	0.34	0.39	0.31	0.20	0.31	0.49
Na2O	-	0.36	-	-	0.20	-	-	-	-	0.02	0.11	-
K2O	-	-	-	-	0.06	-	-	-	-	-	-	-
Total	98.50	98.59	98.33	99.14	99.70	100.61	100.32	100.08	100.16	100.20	99.02	99.66
Mg#	0.32	0.28	0.33	0.33	0.35	0.33	0.32	0.33	0.31	0.26	0.34	0.34
Formula based on six O atoms												
Si	1.95	1.93	1.96	1.94	2.02	1.95	1.95	1.96	1.95	1.94	1.95	1.95
Al	0.05	0.07	0.04	0.06	0.00	0.05	0.05	0.04	0.05	0.06	0.05	0.05
Total T	2.00	2.00	2.00	2.00	2.02	2.00	2.00	2.00	2.00	2.00	2.00	2.00
Ti	0.01	0.01	0.01	0.01	0.00	0.01	0.01	0.01	0.01	0.01	0.00	0.01
Al	0.04	0.03	0.04	0.03	0.08	0.04	0.04	0.04	0.04	0.05	0.04	0.04
Cr	0.00	0.00	0.00	0.00	0.00	0.00	0.00	0.00	0.00	0.00	0.00	0.00
Fe3	0.00	0.06	0.00	0.02	0.00	0.00	0.00	0.00	0.00	0.00	0.03	0.00
Fe2	0.65	0.65	0.64	0.63	0.59	0.64	0.65	0.64	0.66	0.70	0.62	0.63
Mg	0.31	0.26	0.31	0.32	0.31	0.31	0.30	0.31	0.29	0.24	0.32	0.32

Cont.

Total M1(VI)	0.99	0.99	0.99	0.99	0.98	0.99	0.99	0.99	0.99	0.99	1.00	0.99
Fe2	0.65	0.66	0.64	0.64	0.61	0.65	0.66	0.65	0.67	0.71	0.63	0.63
Mn	0.03	0.03	0.02	0.02	0.03	0.02	0.03	0.02	0.03	0.03	0.02	0.03
Mg	0.31	0.27	0.31	0.32	0.33	0.32	0.30	0.31	0.29	0.25	0.33	0.32
Ca	0.02	0.01	0.02	0.02	0.01	0.01	0.01	0.02	0.01	0.01	0.01	0.02
Na	0.00	0.03	0.00	0.00	0.02	0.00	0.00	0.00	0.00	0.00	0.01	0.00
Total M2(VI)	1.00	1.00	1.00	1.00	1.00	1.00	1.00	1.00	1.00	1.00	1.00	1.00
Wo	0.8	0.5	0.9	0.8	0.6	0.7	0.8	0.9	0.7	0.5	0.7	1.1
En	32.1	28.0	32.5	33.1	34.7	32.6	31.3	32.4	30.3	25.5	33.6	33.7
Fs	67.1	71.5	66.6	66.0	64.7	66.7	67.9	66.7	69.0	74.0	65.7	65.2

11.2.2 Standard Deviations

Sample	B19			MB 7		MB1					A3	
Group	**1**											
Pyroxene	1	2	3	1-Rim	1-Core	1	2	3	4	5	1	2
SiO_2	0.22	0.54	0.20	0.49	1.44	0.17	0.29	0.30	0.36	0.84	0.30	0.30
TiO_2	0.05	0.08	0.05	0.08	0.12	0.07	0.03	0.02	0.03	0.05		0.07
Al_2O_3	0.07	0.30	0.09	0.05	0.31	0.07	0.10	0.09	0.06	0.56	0.08	0.12
FeO	0.23	0.88	0.97	0.76	2.06	0.33	0.62	0.83	0.99	0.98	0.17	0.14
MnO	0.07	0.15	0.12	0.07	0.32	0.10	0.06	0.07	0.06	0.19	0.05	0.08
MgO	0.24	0.90	0.65	0.64	0.98	0.24	0.50	0.71	0.63	0.95	0.11	0.15
CaO	0.06	0.06	0.08	0.05	0.13	0.09	0.07	0.05	0.07	0.05	0.03	0.03
Na2O	-	-	-	-	0.17	-	-	-	-	0.05	0.17	-
K_2O	-	-	-	-	0.13	-	-	-	-	-	-	-

11.3 Appendix 3: Averaged biotite compositions and Standard Deviations

11.3.1 Averaged biotite compositions

Sample	MB7		WP 11		A3A5	WP 31			A1		A3	
Group	**1**				**2**	**1**			**2**		**1**	
Biotite Grain	1	2	1	2	1	1	2	3	1	2	1	2
SiO_2	35.35	36.73	36.04	35.94	35.20	34.93	35.12	35.61	34.90	35.42	36.22	34.85
TiO_2	3.81	3.79	3.27	3.90	4.77	2.20	3.20	1.99	4.53	4.12	4.12	1.59
Al_2O_3	14.40	14.65	15.92	15.02	15.76	15.12	15.89	15.39	15.95	16.25	14.15	16.30
FeO	28.38	25.42	26.24	26.64	24.33	27.83	27.69	27.38	26.77	25.14	25.85	28.12
MnO	0.16	0.25	0.28	0.25	0.32	-	0.26	0.26	0.38	0.28	0.16	0.26
MgO	4.82	6.30	4.56	4.73	5.60	6.34	4.56	6.06	4.15	5.43	6.52	5.06
CaO	0.07	0.05	0.05	0.05	0.04	-	0.04	0.06	0.06	-	0.04	-
Na_2O	0.23	0.12	0.20	0.20	0.27	0.28	0.30	0.22	0.20	0.21	0.19	0.09
K_2O	8.67	9.25	9.13	9.08	9.09	8.90	8.87	8.91	9.08	9.49	8.93	8.75
Total	95.90	96.55	95.70	95.81	95.38	95.59	95.94	95.88	96.02	96.33	96.16	95.02

11.3.2 Standard Deviations

Sample	MB 7		WP 11		A3A5	WP 31			A1		A3	
Group	**1**				**2**	**1**			**2**		**1**	
Biotite Grain	1	2	1	2	1	1	2	3	1	2	1	2
SiO_2	0.99	0.17	0.36	0.51	0.40	0.65	0.62	0.41	0.35	0.24	0.57	0.44
TiO_2	0.34	0.46	0.72	0.89	0.90	0.61	0.49	0.60	0.41	0.89	0.82	0.06
Al_2O_3	0.48	0.32	0.47	0.90	0.49	0.45	0.60	0.51	0.28	0.52	0.34	0.26
FeO	1.04	0.37	0.51	0.34	0.64	0.61	0.49	0.48	0.33	0.46	0.51	0.70
MnO	0.06	0.05	0.05	0.03	0.03		0.04	0.05	0.03	0.05	0.04	0.05
MgO	0.59	0.27	0.36	0.28	0.43	0.22	0.16	0.63	0.15	0.47	0.48	0.20
CaO	0.04	0.03	0.03	0.03	0.03	-	0.03	0.04	0.03	-	0.03	-
Na_2O	0.07	0.08	0.06	0.05	0.11	0.09	0.06	0.06	0.08	0.08	0.07	0.02
K_2O	0.40	0.15	0.11	0.14	0.18	0.37	0.21	0.14	0.32	0.18	0.20	0.34

11.4 Appendix 4: Whole rock major and trace element chemistry

11.4.1 Whole rock major chemistry

Sample	A3	A5	B13B	B15	B16	B17	B18A	B18B	B19	B20	B22	B23	B30
Group	**1**												
Al_2O_3	14.45	14.47	14.88	14.46	14.46	14.60	13.10	12.66	14.49	14.62	14.14	13.25	14.73
CaO	1.65	1.56	1.87	1.74	1.40	1.54	0.89	0.87	1.63	1.69	1.24	1.00	1.74
FeO	2.77	2.76	3.02	2.99	2.57	2.60	1.61	1.54	2.67	2.72	2.11	1.77	2.97
K_2O	5.40	5.57	5.40	5.26	5.63	5.69	5.55	5.51	5.54	5.48	5.74	5.62	5.40
MgO	0.44	0.41	0.50	0.49	0.38	0.39	0.19	0.19	0.45	0.45	0.31	0.21	0.50
MnO	0.04	0.04	0.04	0.05	0.04	0.04	0.03	0.02	0.04	0.04	0.03	0.03	0.05
Na_2O	2.69	2.74	2.81	2.68	2.66	2.71	2.39	2.76	2.69	2.74	2.65	2.62	2.75
P_2O_5	0.17	0.16	0.17	0.17	0.17	0.16	0.12	0.12	0.16	0.16	0.14	0.13	0.18
SiO_2	69.62	69.31	68.64	68.66	69.78	69.21	74.58	71.54	69.70	68.96	71.61	72.03	69.15
TiO_2	0.40	0.38	0.45	0.44	0.38	0.38	0.21	0.21	0.38	0.40	0.29	0.23	0.44
LOI	0.53	0.44	0.48	0.51	0.68	0.50	0.67	0.76	0.83	0.65	0.65	0.91	0.72
Total	98.47	98.15	98.60	97.79	98.44	98.11	99.52	96.35	98.88	98.22	99.15	98.00	98.96

Sample	MB1	MB12	MB2	MB22	MB5	MB6	MB7A	MB7B	WIG	WP11	WP12B	WP16	WP18
Group	**1**												
Al_2O_3	14.53	12.39	14.00	14.01	14.91	14.51	14.45	14.56	13.90	14.10	12.49	13.55	13.20
CaO	1.64	0.71	1.57	1.15	1.82	1.65	1.50	1.64	1.11	1.37	0.84	1.30	1.00
FeO	2.89	1.46	2.56	1.90	2.90	2.96	2.65	2.61	1.99	2.54	1.58	2.32	1.75
K_2O	5.50	5.24	5.45	5.83	5.42	5.44	5.58	5.39	5.72	5.54	5.38	5.47	5.64
MgO	0.45	0.15	0.40	0.28	0.48	0.49	0.42	0.40	0.28	0.36	0.19	0.32	0.20
MnO	0.05	0.02	0.04	0.03	0.04	0.04	0.04	0.04	0.03	0.04	0.02	0.03	0.03
Na_2O	2.68	2.37	2.71	2.61	2.78	2.69	2.69	2.74	2.52	2.61	2.40	2.57	2.49
P_2O_5	0.17	0.11	0.15	0.13	0.17	0.17	0.16	0.15	0.13	0.15	0.12	0.15	0.12
SiO_2	69.18	75.18	66.55	71.52	68.36	69.34	70.04	70.07	71.85	70.73	73.04	71.67	73.20
TiO_2	0.41	0.18	0.38	0.26	0.42	0.43	0.38	0.38	0.26	0.35	0.20	0.31	0.22
LOI	0.69	1.17	0.58	1.05	0.69	0.76	0.74	0.85	0.67	0.64	0.69	0.46	0.45
Total	98.52	99.14	94.68	98.98	98.32	98.81	98.95	99.12	98.68	98.71	97.13	98.41	98.50

Sample	WP25A	WP25B	WP29	WP30	WP31	WP31B	WP12A	WP8	B27	A1	A3A5	A7	B9
Group	**1**						**2**						
Al_2O_3	14.38	14.27	14.96	14.26	13.53	14.02	12.90	12.37	12.28	12.11	12.20	12.44	12.26
CaO	1.57	1.52	1.84	1.46	1.12	1.48	0.90	0.78	0.63	0.77	0.76	0.78	0.69
FeO	2.79	2.71	3.08	2.52	2.19	2.51	1.64	1.47	1.55	1.47	1.46	1.49	1.42
K_2O	5.49	5.51	5.48	5.55	5.60	5.43	5.48	5.35	5.24	5.22	5.23	5.37	5.29
MgO	0.44	0.42	0.51	0.35	0.31	0.38	0.20	0.14	0.17	0.16	0.14	0.15	0.14
MnO	0.04	0.04	0.05	0.05	0.04	0.04	0.03	0.02	0.03	0.02	0.03	0.03	0.02
Na_2O	2.66	2.65	2.79	2.69	2.48	2.68	2.40	2.37	2.50	2.34	2.30	2.36	2.38
P_2O_5	0.16	0.16	0.18	0.16	0.14	0.16	0.12	0.11	0.11	0.11	0.11	0.12	0.12
SiO_2	69.89	70.09	68.36	70.53	72.18	70.25	73.84	74.84	75.07	74.93	75.50	75.53	75.63
TiO_2	0.39	0.39	0.45	0.35	0.30	0.35	0.21	0.17	0.17	0.17	0.17	0.17	0.17
LOI	0.63	0.56	0.73	0.63	0.57	0.57	0.70	1.04	0.90	0.59	0.60	0.44	0.61
Total	98.75	98.63	98.78	98.83	98.71	98.15	98.60	98.82	98.82	98.05	98.66	99.05	98.89

Sample	MB10	MB11	MB26	B13A	B26	B28
Group	**2**					
Al_2O_3	12.27	12.26	12.56	11.88	12.13	12.25
CaO	0.71	0.68	0.76	0.58	0.73	0.72
FeO	1.42	1.38	1.57	1.38	1.53	1.42
K_2O	5.31	5.26	5.25	5.09	5.16	5.31
MgO	0.14	0.14	0.15	0.15	0.15	0.14
MnO	0.03	0.02	0.02	0.02	0.02	0.02
Na_2O	2.32	2.30	2.43	2.25	2.32	2.33
P_2O_5	0.11	0.11	0.11	0.11	0.11	0.11
SiO_2	75.76	75.49	75.03	74.95	75.33	75.22
TiO_2	0.16	0.16	0.18	0.16	0.17	0.16
LOI	0.76	0.92	0.76	1.29	0.71	0.68
Total	99.15	98.88	99.00	98.02	98.53	98.52

11.4.2 Trace element chemistry

Sample	a3	a5	B13B	B15	B16	B17	B18A	B18B	B19	B20	B22	B23	B30
Group	**1**												
V	29.32	29.62	30.31	30.46	25.67	25.37	12.72	11.37	24.76	26.8	18.63	12.66	30.11
Cr	12.11	17.1	13.01	19.12	10.85	14.84	8.26	12.36	20.5	14.15	14.43	12.36	20.77
Co	104.51	116.96	71.28	83.05	83.58	98.57	163.38	121.73	91.87	93.86	111.32	134.05	103.74
Ni	7.7	6.65	7.1	7.25	7.46	7.49	5.74	4.97	7.66	6.69	21.54	7.84	9.23
Cu	18.05	16.75	10.39	18.52	18.16	15.21	14.75	7.67	22.08	13.75	15	6.9	16.23
Zn	55.17	75.17	67.62	54.17	63.6	69.08	45.74	44.1	45.19	64.91	51.06	50.75	64.89
Rb	203.14	264.45	200.69	202.66	212.73	216.22	243.25	228.46	198.97	203.96	220.6	225.43	207.53
Sr	100.42	118.25	109.44	116.85	97.28	104.55	58.29	54.26	131.63	104.81	84.64	62	104.73
Y	33.87	41.58	33.61	44.25	32	35.56	30.19	29.76	47.4	34.68	31.54	28.7	34.37
Zr	236.8	273.54	277.37	345.46	217.3	243.47	113.42	111.66	322.03	248.6	192.67	125.3	270.17
Nb	20.4	25.5	22.84	24.13	19.75	20.73	15.23	14.42	21.17	21.02	18.19	15.89	21.83
Mo	1.92	2.38	2.51	2.19	2.02	2.27	1.13	1.1	1.71	1.65	0.79	0.84	2.36
Cs	8.52	12.71	9.12	9.38	7.8	8.6	10.53	9.88	8.31	8.54	8.22	10.6	8.96
Ba	852.33	1143.05	934.9	926.18	825.56	952.16	478.07	461.85	1031.49	922.83	720.63	554.26	850.97
La	50.77	61.51	56.5	68.45	45.65	51.06	25.05	24.6	66.1	53.16	37.95	27.28	55.6
Ce	115.2	139.84	131.58	138.72	103.76	113.48	60.36	59.44	131.08	120.71	87.35	65.97	127.61

Sample	MB1	MB12	MB2	MB22	MB5	MB6	MB7A	MB7B	wig	wp11	wp16	wp12b	wp18
Group	**1**												
V	28.64	10.13	23.83	15.6	28.78	30.54	24.33	24.55	16.44	27.1	21.65	13.2	13.87
Cr	19.44	9.55	8.11	10.68	10.14	24.95	10.28	15.48	32.18	< 9	13.64	10.87	13.78
Co	74.01	123.98	71.19	134.64	86.41	80.36	101.86	108.81	100.97	114.75	93.52	138.02	138.02
Ni	7.66	3.43	5.87	6.56	6.4	6.41	6.2	6.12	5.26	8.86	7.2	9.44	5.76
Cu	7.84	6.07	9.53	8.09	12.36	13.12	12	8.19	13.5	20.19	11.78	15.88	13.68
Zn	70.75	46.03	70.68	52.52	74.48	76.39	66.52	66.77	40.81	62.27	58.06	46.55	49.48
Rb	202.02	235.55	202.58	221.89	201.91	205.17	212.47	210.91	209.04	260.41	265.03	267.74	279.94
Sr	107.7	42.33	100.14	88.15	109.75	110.76	96.55	98.09	72.03	96.4	91.2	60.62	68.3
Y	41.49	31.08	36.15	32.13	35.31	42.56	34.32	34.29	28.53	39.57	36.46	36.61	34.76
Zr	287.2	94.92	239.84	164.15	268.24	318.26	231.89	238.59	152.36	240.41	212.3	132.98	131.84
Nb	21.65	15.18	18.58	16.68	22.38	24.05	21.23	19.9	15.45	23.15	21.48	17.17	17.85
Mo	1.85	1.72	2.15	0.63	2.01	1.62	2.19	1.95	1.01	2.21	1.82	2.62	0.63
Cs	9.17	8.41	8.26	7.42	8.79	8.37	9.54	9.56	8.85	11.63	12.41	11.47	12.97
Ba	876.63	302.9	851.26	752.93	901.27	909.17	817.86	768.59	595.96	851	779.21	492.19	571.51
La	57.12	20.65	49.52	36.83	56.43	62.3	49	49.45	31.01	52.43	46.47	29.66	32.24
Ce	124.28	50.39	108.99	83.53	125.7	134.72	111.57	110.92	70.86	121.87	106.88	70.26	76.3

Sample	wp25a	wp25b	wp29	wp30	wp31	wp31B	WP12	WP8	B27	A1	A3/A5	A7	B9
Group	**1**						**2**						
V	27.2	25.89	31.45	21.59	23.93	18.02	13.04	9.44	9.42	10.52	10.32	11.21	8.18
Cr	< 9	24.53	14	< 9	12.22	< 9	< 9	8.11	5.5	9.75	< 8	8.88	9.94
Co	101.66	88.76	104.38	82.17	99.25	106.09	133.73	108	112.13	141.62	131.25	80.14	150.95
Ni	7.37	9.24	8.24	6.42	4.87	5.65	9.44	4.49	5.84	5.65	4.04	4.49	5.98
Cu	20.71	23.73	20.56	22.06	12.53	10.31	25.3	17.67	16.71	13.96	16.36	23.88	13.36
Zn	62	59.86	65.72	55.49	54.38	43.15	51.82	48.77	47.59	34.45	40.92	44.88	47.8
Rb	212.53	204.32	194.7	226.53	213.16	210.14	274.08	248.9	247.45	216.44	285.46	291.78	272.8
Sr	95.91	91.04	113.94	84.12	85.61	71.59	67	48.7	41.89	41.05	46.25	50.36	40.75
Y	35.33	32.99	35.89	32.89	32.94	30.64	38.24	32.65	30.57	28.04	34.9	35.4	32.6
Zr	238.78	230.42	282.53	199.89	215.25	168	136.74	106.18	91.79	87.34	104.58	105.69	90.04
Nb	21.21	19.5	21.7	19.11	18.92	16.39	17.55	14.27	14.97	13.29	16.56	16.73	15.84
Mo	2.29	1.86	1.9	1.89	1.82	1.41	1.03	2.41	2.11	2.09	2.42	2.68	0.84
Cs	8.96	8.15	7.22	8.85	9.17	8.86	11.98	11.74	8.1	7.9	12.15	11.45	12.01
Ba	773.58	711.79	933.71	684.37	674.24	579.85	552.8	380.06	302.36	302.85	339.06	408.18	301.27
La	49.74	46.49	57.44	42.25	42.84	34.02	31.9	22.68	19.65	18.75	22.71	24.04	19.81
Ce	109.96	105.81	124.84	95.77	96.38	78.16	74.59	53.88	48.52	45.94	55.85	59.34	49.02

Sample	MB10	MB11	MB26	B13A	B26	B28
Group	**2**					
V	8.14	8.75	9.4	8.6	9.78	9.94
Cr	14.19	9.48	11.14	11.6	9.15	9.1
Co	112.26	147.92	81.42	113.66	117.12	118.53
Ni	5.15	5.1	6.25	7.52	6.07	5.91
Cu	7.29	8.35	8.44	15.07	19.37	7.32
Zn	47.7	43.12	47.44	43.64	49.74	44.2
Rb	241.14	251.86	248.01	234.19	245.75	253.17
Sr	41.86	41.26	38.62	36.97	39.71	40.5
Y	32.19	30.04	33.03	30.44	33.05	31.1
Zr	91.31	85.24	91.7	84.61	95.78	86.61
Nb	14.29	14.74	15.98	14.5	15.53	15.59
Mo	0.73	2	2.35	2.33	2.21	1.6
Cs	10.21	9.88	10.88	7.55	9.36	11.07
Ba	320.07	297.66	267.17	286.56	283.88	291.47
La	20.14	18.81	19.92	18.53	20.01	18.74
Ce	48.22	46.6	48.71	46.77	48.67	47.46

Sample	A3	A5	B13B	B15	B16	B17	B18A	B18B	B19	B20	B22	B23	B30
Group	**1**												
Pr	12.62	15.22	14.05	15.85	11.48	12.61	6.48	6.59	15.51	13.2	9.6	7.37	13.85
Nd	45.38	56.43	51.58	60.52	41.21	46.47	23.31	23.42	58.15	47.46	34.59	26.35	49.78
Sm	8.8	11.27	9.38	11.45	8.23	9.61	5.3	5.31	11.74	9.62	7.54	5.8	9.61
Eu	1.61	1.89	1.62	1.78	1.44	1.59	0.9	0.89	1.93	1.56	1.28	0.96	1.53
Gd	8.02	10.61	7.67	9.51	6.6	7.63	4.82	4.85	9.96	7.66	6.32	5.06	7.43
Tb	1.17	1.48	1.14	1.5	1.03	1.14	0.86	0.89	1.42	1.09	1.07	0.87	1.17
Dy	6.45	8.46	6.72	8.35	6.16	6.89	5.36	5.4	8.54	6.6	5.93	5.49	6.57
Ho	1.24	1.66	1.27	1.77	1.17	1.31	1.09	1.09	1.82	1.27	1.16	1.07	1.25
Er	3.31	4.47	3.5	4.55	3.25	3.49	3.12	3.14	4.79	3.49	3.15	2.82	3.5
Tm	0.48	0.62	0.45	0.62	0.43	0.51	0.43	0.45	0.69	0.48	0.44	0.39	0.47
Yb	3.18	4.42	2.96	4.14	2.96	3.49	2.84	2.8	4.25	3.21	3.04	2.9	3.11
Lu	0.44	0.56	0.44	0.57	0.41	0.45	0.38	0.37	0.63	0.45	0.41	0.37	0.43
Hf	6.1	7.87	7.07	8.74	5.65	6.51	3.32	3.25	8.55	6.55	5.45	3.67	6.84
Ta	1.25	1.83	1.29	1.55	1.19	1.37	1.08	1.04	1.45	1.27	1.18	1.1	1.27
Pb	33.8	51.31	37.52	31.63	39.79	42.03	36.4	32.67	28.78	39.83	40.24	34.24	40.06
Th	18.87	24.88	20.91	25.44	18.06	20.56	12.07	12.03	25.52	20.35	16.67	13.26	20.76
U	4.28	6.79	4.96	5.15	4.17	5.64	4.5	4.13	4.67	4.3	3.39	3.42	4.95

Sample	MB1	MB12	MB22	MB2	MB5	MB6	MB7A	MB7B	WIG	WP11	WP12B	WP16	WP18
Group	**1**												
Pr	13.67	5.64	9.21	12.1	13.66	15.12	12.24	12.33	7.71	13.37	7.84	11.64	8.56
Nd	52.74	20.25	34.09	44.6	50.23	55.57	44.65	45.25	28.88	48.46	28.61	42.86	30.74
Sm	10.4	5.09	7.22	9.13	9.53	11.23	9.16	8.75	5.98	9.91	6.7	8.52	7.46
Eu	1.55	0.61	1.3	1.43	1.59	1.62	1.41	1.44	1.13	1.62	1.02	1.51	1.15
Gd	8.27	4.76	6.02	7.92	7.82	9.6	7.46	7.13	5.67	9.19	6.96	8.57	6.67
Tb	1.2	0.91	0.95	1.2	1.18	1.38	1.15	1.09	0.9	1.41	1.1	1.22	1.09
Dy	7.57	5.76	6.1	7.07	6.99	8.32	6.8	6.57	5.12	7.99	7	7.25	6.77
Ho	1.61	1.1	1.24	1.31	1.27	1.63	1.25	1.25	1.03	1.52	1.44	1.46	1.3
Er	4.13	3.28	3.42	3.61	3.49	4.54	3.34	3.34	2.86	4.36	3.99	4.06	4.03
Tm	0.59	0.47	0.46	0.5	0.48	0.59	0.49	0.45	0.43	0.62	0.57	0.6	0.55
Yb	3.75	3.19	3.05	3.16	3.41	3.89	3.34	3.12	2.68	4.07	3.73	3.86	3.59
Lu	0.51	0.44	0.41	0.46	0.47	0.53	0.48	0.44	0.39	0.61	0.54	0.5	0.48
Hf	7.58	3.13	4.6	6.5	7.12	8.21	6.38	6.27	4.04	7.01	4.26	6.15	4.1
Ta	1.37	1.21	1.23	1.22	1.3	1.58	1.33	1.24	1.04	1.62	1.39	1.54	1.38
Pb	37.04	33.42	42.96	39.98	39.88	36.65	40.59	40.73	33.4	47.54	40.99	47.9	46.3
Th	22.37	11.96	16.41	19.57	21.06	24.54	19.67	19.3	13.71	22.2	15.6	20.22	16.73
U	5.32	6.64	3.18	4.8	5.13	4.45	5.43	4.74	3.75	6.43	8.13	5.44	4.56

Sample	WP25A	WP25B	WP29	WP30	WP31A	WP31B	WP12	WP8	B27	A1	A3/A5	A7	B9
Group	**1**						**2**						
Pr	12.22	11.57	13.83	10.43	10.66	8.52	8.36	6.07	5.42	5.07	6.19	6.62	5.55
Nd	44.85	42.66	50.64	38.52	39.35	31.79	30.81	21.97	19.47	18.31	22.65	23.78	19.9
Sm	8.92	8.15	9.59	8.18	8.32	6.58	7.01	5.33	4.82	4.29	5.98	6.04	4.96
Eu	1.41	1.37	1.66	1.26	1.29	1.1	1.04	0.71	0.62	0.62	0.74	0.92	0.59
Gd	8.07	7.73	8.74	7.48	7.55	6.53	7.15	5.15	4.69	4.64	5.8	6.11	4.47
Tb	1.16	1.15	1.21	1.06	1.12	0.9	1.13	0.89	0.88	0.76	1.02	1.11	0.88
Dy	6.57	6.43	6.79	6.17	6.13	5.77	7.24	6	5.46	4.79	6.73	6.72	5.44
Ho	1.25	1.14	1.3	1.21	1.28	1.11	1.44	1.19	1.11	1.02	1.35	1.37	1.19
Er	3.48	3.32	3.32	3.29	3.4	3.09	4.18	3.5	3.3	2.93	3.82	4.22	3.29
Tm	0.49	0.45	0.52	0.45	0.49	0.44	0.6	0.49	0.45	0.41	0.54	0.61	0.46
Yb	3.28	3.09	3.26	3	3.22	2.96	3.99	3.18	3.07	2.74	3.87	3.96	3.08
Lu	0.46	0.42	0.49	0.41	0.43	0.41	0.53	0.41	0.42	0.38	0.5	0.53	0.44
Hf	6.21	6.04	7.26	5.23	5.79	4.37	4.27	3.31	2.68	2.53	3.48	3.62	2.72
Ta	1.29	1.22	1.34	1.2	1.25	1.1	1.47	1.24	1.21	0.99	1.39	1.41	1.21
Pb	38.1	35.92	36.59	36.14	35.79	34.24	44.19	37.15	35.29	29.37	39.29	42.08	32.78
Th	19.42	17.96	21.28	16.93	17.74	14.77	16.7	12.9	11.62	10.33	13.51	14.18	11.66
U	5.54	4.77	4.69	4.88	5.27	3.84	5.39	7.02	6.98	5.93	8.28	8.62	4.71

Sample	MB10	MB11	MB26	B13A	B26	B28
Group	**2**					
Pr	5.38	5.35	5.5	5.07	5.44	5.34
Nd	20.47	18.39	19.96	18.53	20.07	18.77
Sm	4.9	4.78	5.04	4.61	5.19	4.95
Eu	0.65	0.61	0.55	0.59	0.61	0.63
Gd	4.74	4.31	4.69	4.38	4.77	4.34
Tb	0.89	0.82	0.89	0.82	0.88	0.82
Dy	5.53	5.25	6.02	5.51	5.99	5.4
Ho	1.19	1.11	1.26	1.05	1.22	1.16
Er	3.43	3.3	3.49	3.1	3.42	3.17
Tm	0.45	0.45	0.53	0.45	0.48	0.45
Yb	3.17	2.98	3.33	2.98	3.3	3.17
Lu	0.42	0.4	0.47	0.38	0.42	0.4
Hf	2.76	2.68	2.85	2.65	2.99	2.66
Ta	1.16	1.13	1.28	1.1	1.25	1.11
Pb	35.41	32.57	33.24	30.57	34.74	32.58
Th	11.74	11.21	12.22	10.89	11.87	11.15
U	4.49	6.93	7.63	6.84	6.63	5.8

11.5 Appendix 5: Peritectic assemblage entrainment modelling

The melt used in modelling peritectic assemblage entrainment is a hypothetical melt, regarded to represent a hypothetical melt composition most compatible for the rhyolitic rocks of this study.

Reaction: 0.416 Hornblende + 1.2Biotite + 11.57 Quartz + 9.129Plagioclase (An 40) = 16.91 Melt + 7.5Plagioclase (An 42)+ 0.644 Ilmenite + 4.911Orthopyroxene+ 2.195Clinopyroxene

$$0.416\ Si_{6.547}\ Ti_{0.283}\ Al_{1.96}\ (Fe, Mg)_{4.45}\ Ca_{1.92}\ Na_{0.278}\ K_{0.221}\ O_{22}(OH)_2 + 1.2Si_{5.9}\ Ti_{0.47}\ Al_{2.68}\ (Fe, Mg)_{4.3}\ Na_{0.19.}\ K_{1.727}\ O_{20}\ (OH)_4 + 11.572\ SiO_2 + 9.158\ Si_{2.569}\ Al_{1.431}\ Na_{0.600}\ Ca_{0.400}\ O_8 = 16.91\ Si_{1.198}\ Ti_{0.002}\ Al_{0.256}\ Fe_{0.018}\ Mg_{0.003}\ Ca_{0.013}\ Na_{0.075}\ K_{0.13}O_{0.3037}(OH)_{0.33} + 7.5\ Si_{2.3}Al_{1.7}Ca_{0.42}Na_{0.58} + 0.643\ TiFeO_3 + 4.898\ Si_2(Fe, Mg)_2O_6 + 2.195\ Si_2(Fe, Mg)CaO_6$$

Magma compositions which reflect the entrainment of a peritectic assemblage produced by the reaction to the melt										
	SiO_2	TiO_2	Al_2O_3	Fe_2O_3	MgO	CaO	Na_2O	K_2O	H	Mol.% Peritectic Assemblage Entrained
Melt	72.95	0.16	13.22	1.35	0.14	0.71	2.28	6.18	3.00	0
Magma 1	71.14	0.31	13.94	1.93	0.47	1.31	2.46	5.69	2.76	5
Magma 2	69.61	0.41	14.55	2.43	0.75	1.81	2.61	5.27	2.56	10

11.6 Appendix 6: Sample Locality Coordinates

Sample	Texture	Latitude	Longitude
WP 11	Group 1	32° 58' 52.6182"	17° 52' 52.2588"
WP 12B	Group 1	32° 58' 35.7162"	17° 52' 52.1322"
A3	Group 1	33° 0' 18.1362"	17° 56' 22.092"
A5	Group 1	33° 0' 18.1362"	17° 56' 22.092"
WP 16	Group 1	32° 58' 10.9986"	17° 53' 8.0016"
WP 18	Group 1	32° 57' 28.98"	17° 52' 58.0002"
WP 25A	Group 1	32° 56' 26.0016"	17° 53' 11.0004"
WP 25B	Group 1	32° 56' 26.0016"	17° 53' 11.0004"
WIG	Group 1	32° 59' 52.0002"	17° 52' 23.9982"
WP 29	Group 1	32° 59' 52.0002"	17° 52' 23.9982"
WP 30	Group 1	32° 59' 52.0002"	17° 52' 23.9982"
WP 31A	Group 1	32° 59' 25.0008"	17° 52' 54.9984"
WP 31B	Group 1	32° 59' 25.0008"	17° 52' 54.9984"
MB1	Group 1	33° 2' 5.7618"	17° 55' 41.8866"
MB2	Group 1	33° 2' 3.0228"	17° 55' 37.3188"
MB5	Group 1	33° 2' 16.2918"	17° 55' 41.7642"
MB 6	Group 1	33° 2' 4.671"	17° 55' 47.3226"
MB 7	Group 1	33° 2' 6.9252"	17° 55' 32.6562"
MB7B	Group 1	33° 2' 8.3724"	17° 55' 18.2064"
MB 12	Group 1	33° 2' 1.1646"	17° 56' 5.8092"
B 13 B	Group 1	33° 1' 14.8542"	17° 55' 4.3464"
B 15	Group 1	33° 2' 28.23"	17° 55' 45.3684"
B 16	Group 1	33° 2' 50.388"	17° 54' 58.7298"
B 17	Group 1	33° 3' 4.392"	17° 54' 38.3436"
B 18	Group 1	33° 2' 50.4312"	17° 54' 29.16"
B18B	Group 1	33° 2' 47.0148"	17° 54' 10.8684"
B 19	Group 1	33° 2' 21.8214"	17° 53' 48.7356"
B 20	Group 1	33° 1' 45.5556"	17° 53' 30.8754"
B 22	Group 1	33° 1' 35.6196"	17° 56' 23.8158"
MB 22	Group 1	33° 1' 35.9358"	17° 56' 27.153"
B 23	Group 1	33° 1' 35.04"	17° 56' 29.7492"
B30	Group 1	33° 1' 17.9646"	17° 54' 52.6062"
B26	Group 2	33° 1' 42.0636"	17° 57' 20.307"
MB26	Group 2	33° 1' 42.9816"	17° 57' 19.767"
B 27	Group 2	33° 1' 43.0386"	17° 57' 21.4626"
B28	Group 2	33° 1' 44.22"	17° 57' 21.4482"
A1	Group 2	33° 1' 29.7474"	17° 57' 13.122"
A7	Group 2	33° 1' 29.7474"	17° 57' 13.122"
MB 10	Group 2	33° 1' 41.7864"	17° 57' 14.295"
MB 11	Group 2	33° 1' 41.4078"	17° 57' 13.4958"
B 13A	Group 2	33° 2' 0.3912"	17° 56' 2.2884"

WP8	Group 2	33° 1' 38.6322"	17° 57' 9.2268"
WP 12A	Group 2	32° 58' 35.7162"	17° 52' 52.1322"
A3A5	Group 2	33° 0' 23.1804"	17° 56' 21.4758"
B 9	Group 2	33° 1' 43.1472"	17° 57' 15.2208"